THERMO-POROELASTIC MODELING OF RESERVOIR STIMULATION AND MICROSEISMICITY USING FINITE ELEMENT METHOD WITH DAMAGE MECHANICS

A Dissertation

by

SANG HOON LEE

Submitted to the Office of Graduate Studies of
Texas A&M University
in partial fulfillment of the requirements for the degree of

DOCTOR OF PHILOSOPHY

December 2011

Major Subject: Petroleum Engineering

Thermo-Poroelastic Modeling of Reservoir Stimulation and Microseismicity Using

Finite Element Method with Damage Mechanics

Copyright 2011 Sang Hoon Lee

THERMO-POROELASTIC MODELING OF RESERVOIR STIMULATION AND MICROSEISMICITY USING FINITE ELEMENT METHOD WITH DAMAGE MECHANICS

A Dissertation

by

SANG HOON LEE

Submitted to the Office of Graduate Studies of
Texas A&M University
in partial fulfillment of the requirements for the degree of

DOCTOR OF PHILOSOPHY

Approved by:

Chair of Committee,	Ahmad Ghassemi
Committee Members,	Stephen A. Holditch
	Akhil Datta-Gupta
	Rashid K. Abu Al-Rub
Head of Department,	Stephen A. Holditch

December 2011

Major Subject: Petroleum Engineering

ABSTRACT

Thermo-Poroelastic Modeling of Reservoir Stimulation and Microseismicity Using Finite Element Method with Damage Mechanics. (December 2011)

Sang Hoon Lee, B.S., University of Seoul;

M.S., Seoul National University

Chair of Advisory Committee: Dr. Ahmad Ghassemi

Stress and permeability variations around a wellbore and in the reservoir are of much interest in petroleum and geothermal reservoir development. Water injection causes significant changes in pore pressure, temperature, and stress in hot reservoirs, changing rock permeability. In this work, two- and three-dimensional finite element methods were developed to simulate coupled reservoirs with damage mechanics and stress-dependent permeability. The model considers the influence of fluid flow, temperature, and solute transport in rock deformation and models nonlinear behavior with continuum damage mechanics and stress-dependent permeability.

Numerical modeling was applied to analyze wellbore stability in swelling shale with two- and three-dimensional damage/fracture propagation around a wellbore and injection-induced microseismic events. The finite element method (FEM) was used to solve the displacement, pore pressure, temperature, and solute concentration problems.

Solute mass transport between drilling fluid and shale formation was considered to study salinity effects. Results show that shear and tensile failure can occur around a

wellbore in certain drilling conditions where the mud pressure lies between the reservoir pore pressure and fracture gradient.

The fully coupled thermo-poro-mechanical FEM simulation was used to model damage/fracture propagation and microseismic events caused by fluid injection. These studies considered wellbore geometry in small-scale modeling and point-source injection, assuming singularity fluid flux for large-scale simulation. Damage mechanics was applied to capture the effects of crack initiation, microvoid growth, and fracture propagation. The induced microseismic events were modeled in heterogeneous geological media, assuming the Weibull distribution functions for modulus and permeability.

The results of this study indicate that fluid injection causes the effective stress to relax in the damage phase and to concentrate at the interface between the damage phase and the intact rock. Furthermore, induced-stress and far-field stress influence damage propagation. Cold water injection causes the tensile stress and affects the initial fracture and fracture propagation, but fracture initiation pressure and far-field stress are critical to create a damage/fracture plane, which is normal to the minimum far-field stress direction following well stimulation. Microseismic events propagate at both well scale and reservoir-scale simulation; the cloud shape of a microseismic event is affected by permeability anisotropy and far-field stress, and deviatoric horizontal far-field stress especially contributes to the localization of the microseismic cloud.

DEDICATION

To my God

To my wife for her unconditional love and support

ACKNOWLEDGEMENTS

I would like to express special thanks to my advisor, Dr. Ahmad Ghassemi, for his respectful diligence, motivation, patience, unlimited support and advice through the course of PhD work. Also my deep acknowledgement to the committee members, Drs. Holditch, Datta-Gupta and Abu Al-Rub, for the useful comments that helped my dissertation.

Special thanks to the Harold Vance Department of Petroleum Engineering faculty and staff for their help whenever I needed it. To my friends in the department, the many times we spent in discussion and the cooperation we shared is unforgettable.

I would like to thank the Geothermal Technologies Program from the Department of Energy for the fellowship and encouragement to develop the project.

Finally, I would like to thank my parents for their prayers to God for my success during my PhD work. Also I would like to thank my wife Sunghei Jean for her love, unconditional support and encouragement. My two sons Jayden and Kayden always boost morale during the course of my PhD.

TABLE OF CONTENTS

Page

Page

LIST OF FIGURES

Page

Page

Page

Page

Page

Page

Page

Page

Page

Page

Page

Page

Page

LIST OF TABLES

1. INTRODUCTION

Stress analysis or rock mass failure in response to water injection is of much interest in oil and gas exploration and geothermal reservoir design. The process involves coupled rock deformation, fluid flow, heat transfer and chemical interactions in the porous rock. Interest in understanding rock deformation and failure during fluid injection has increased in enhanced geothermal systems, unconsolidated petroleum reservoirs, and unconventional resources such as gas shales.

From the geomechanical point of view, the impact of the variations of pore pressure, temperature and chemical interaction are key factors in reservoir engineering. These are of especially interesting around a wellbore, where their impact is particularly significant during injection and production, which may lead to problems such as borehole collapse, distortion, and buckling during injection or drilling (Yu et al., 2001). These problems are mainly caused where the rock's effective stress exceeds its strength. In addition, the far-field stresses are among the most important factors in geomechanical engineering since the stress regime impacts rock failure, its geometry, and the resulting fluid path. The stress distributions around a wellbore are influenced both by the injection-induced stress and far-field stress in the reservoir so they must be accounted for in determining the impact of fluid flow, temperature and chemical interaction with far-field stresses (Fig. 1.1).

This dissertation follows the style of *Geothermics*.

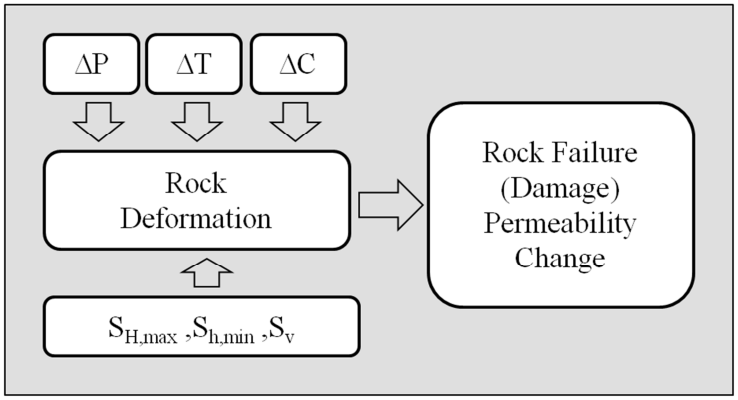

Fig. 1.1. The key factors in geomechanical engineering design.

Generally, the strain-stress behavior of rocks in experimental tests shows hardening and post-peak softening or directly reaches the softening regime, depending on the rock type and conditions such as pore pressure, stress conditions, and temperature (Jaeger et al., 2007). The continuum damage mechanics approach can capture the hardening and softening behavior of the rock (Yuan and Harrison, 2006), and permeability variation caused by the stress change and rock failure is critical in the analysis of wellbore stability and well stimulation. Induced microseismic events are among the promising approaches to estimate permeability changes and stress distributions since they measure the earthquake energy where geological formations have become imbalanced by fluid injection. The characteristics of microseismic events such as their locations, spatial patterns of distribution, and temporal relations between the occurrence of seismicity and reservoir activities are often studied for enhanced geothermal systems (EGS). Microseismic event detection and interpretation is used for estimating the stimulated volume and fracture growth, resulting reservoir permeability,

and geometry of the geological structures and the in-situ stress state (Pine, 1984). Numerical modeling of the coupled processes in rock can help improve understanding of MEQ and will improve reservoir development activities.

1.1 Motivation and objectives of the study

The theory of thermo-poroelasticity can explain the coupling of fluid flow and temperature effects in rock deformation. It provides a robust framework for studying the rock deformation and stress redistributions after rock failure. However, it could be improved by developing three-dimensional injection/extraction geomechancis models that not only consider induced rock failure and fracture propagation but also take into account rock damage and permeability variations. Continuum damage mechanics with fully coupled thermo-poroelasticity using finite element methods can be used for this purpose. The objectives of the research were:

- To develop a fully coupled thermo-chemo-poroelastic and three-dimensional finite element model that considers rock damage and stress-dependent permeability for simulating the influence of fluid flow and temperature with various injection schedules under anisotropic far-field stress conditions
- To investigate the influence of solute transport in wellbore stability with damage evolution in low permeability shale drilling
- To observe the injection-induced stress variations, permeability change and rock failure

- To simulate and study the three-dimensional propagation of damage/fracture and microseismic events under different stress regimes and to investigate the key factors for temporal and spatial distributions in induced microseismic events

This has been achieved by studying the theory of thermo-poroelasticity and chemo-thermo-poroelasticity and describing the nonlinear behavior of rock using damage mechanics and permeability change caused by fluid injection.

1.2 Fluid flow, temperature, and solute transport in porous rock

Coupled hydromechanical process analysis was initially motivated by soil consolidation problems. Terzaghi (1923) presented the one-dimensional consolidation theory that takes into account pore pressure and the soil deformation. Biot (1941) developed a model for linear poroelasticity that considered the stress change under fluid loading and pore pressure variations under applied stress. This theory has been extended to include the influence of temperature, fluid flow, and rock deformation and is called thermo-poroelasticity (McTigue, 1986; Kurashige, 1989; Wang and Papamichos, 1994). Heidug and Wong (1996) proposed the constitutive equations for swelling shale based on nonequilibrium thermodyanamics. Ghassemi and Diek (2003) considered combined effects of chemical potential and thermal osmosis on water flow in and out of the mud and shale formation. They indicated that in addition to thermal osmosis, chemical osmosis also can be several times higher than hydraulic pressure in certain conditions. Also, a linear chemo-thermo-poroelasticity was developed to remedy the cumbersome

solution of the original chemo-thermo-poroelasticity for practical applications. Details of these mathematical formulations will be illustrated in Section 2.

1.2.1 Biot poroelasticity

Biot (1941) developed the coupled fluid and solids consolidation problem in porous media. He assumed that the material is homogeneous and fully saturated, and fluid flow follows Darcy's law in porous media. The problem domain that illustrated the influence of loading in excess pore pressure variation is shown in Fig. 1.2. Consider a fully saturated poroelastic layer from $z = 0$ to $z = h$, and normal traction P applied at the top surface. Initially the layer deforms as elasticity, and an excess pore pressure induces the change of displacement as results of the Skempton effect. The fluid flow dries out gradually with time, and the layer continuously deforms vertically.

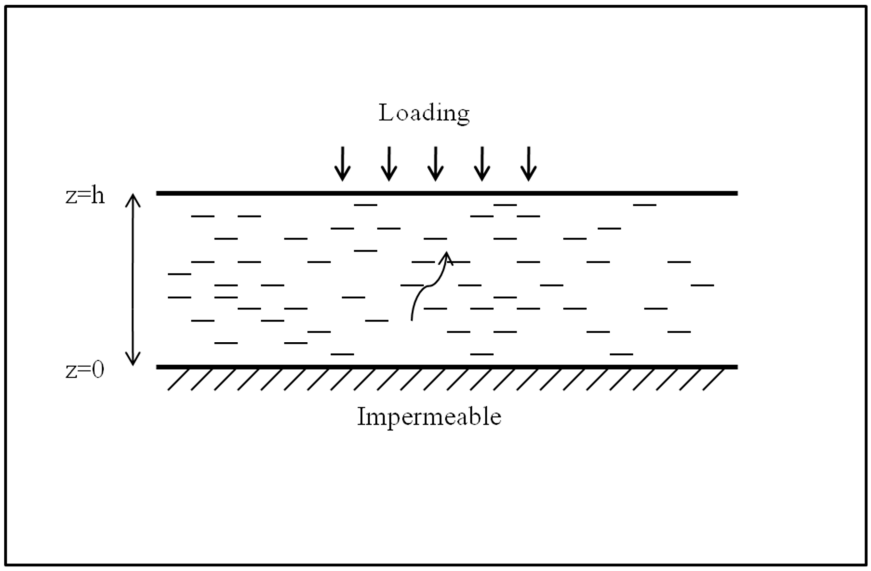

Fig. 1.2. Sketch of the Biot consolidation problem.

Assuming the fluid drains on the surface and the system is impermeable at the bottom, the governing equations for the transient phenomena of consolidation as follow,

$$\frac{1}{a}\frac{\partial^2 w}{\partial z^2} - \alpha\frac{\partial w}{\partial z} = 0 \quad \text{..... (1.1)}$$

$$k\frac{\partial^2 p}{\partial z^2} = \alpha\frac{\partial^2 w}{\partial z \partial t} + \frac{1}{Q}\frac{\partial p}{\partial t} \quad \text{..... (1.2)}$$

where $a = \frac{1-2\gamma}{2G(1-\nu)}$ is the compressibility, α is the Biot's constant, k is the coefficient of permeability of the soil including the viscosity, and Q is the volume of water which can be forced into the soil under pressure while the volume of the soil is kept constant.

Initial and boundary conditions for the consolidation problem can be described as no fluid flow at the bottom and zero pore pressure because of drainage on the surface.

$$\sigma = \frac{p_0}{\left(\frac{1}{\alpha a Q} + \alpha\right)} \quad for \quad t = 0 \quad \text{..... (1.3)}$$

$$\frac{\partial p}{\partial z}(z = 0, t) = 0 \quad \text{..... (1.4)}$$

$$p(z = h, t) = 0 \quad \text{..... (1.5)}$$

The interesting solution for the consolidation problem is the change of displacement after loading (Biot, 1941).

$$w_s = \frac{8}{\pi} a h p_0 \sum_0^\infty \frac{1}{(2n+1)^2} \times \left\{1 - \exp\left[-\left(\frac{(2n+1)\pi}{2h}\right)^2 ct\right]\right\} \quad \text{..... (1.6)}$$

The analytical solution in Fig. 1.3 shows the displacement change on the top surface under loading with respect to time, and the corresponding pore pressure changes illustrate how (Fig. 1.4) the saturated water diffuses through the porous soil and out of its top surface as time increases. Note that maximum pore pressure in the middle (consolidation effect) can disappear in a very short time when the permeability (as is the case here) is relatively high (100 md). The consolidation effects will be discussed in more detail in Section 3, in the context of pore pressure distribution around a wellbore in ultralow-permeability rock.

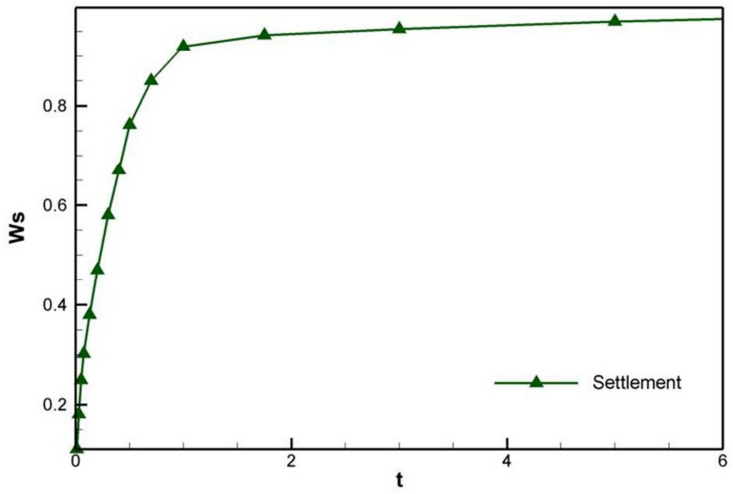

Fig. 1.3. Surface displacement with time.

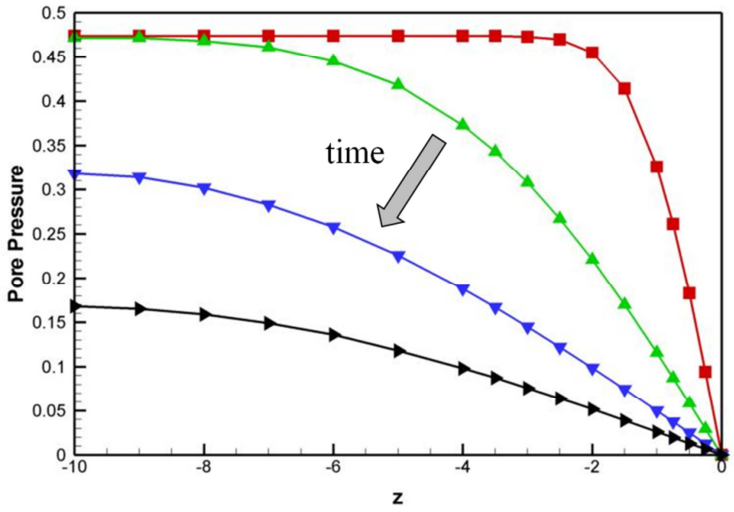

Fig. 1.4. Pore pressure change for various depths, as a function of time.

The theory of Biot consolidation represents fully coupled interaction of fluid flow and solids. It provides general schemes of the interaction between fluid flow and mechanical loading. Similar phenomena are observed around a wellbore.

1.2.2 The concept of thermal stress

The change of temperature induces stress and displacement in a rock skeleton. The theory of thermoelasticity is analogous to the theory of poroelasticity, but instead of pore pressure, it includes the role of temperature change. Palciauskas and Domenico (1982) and McTigue (1986) studied the effects of temperature change on pore pressure and stress in rock. Considering linear elasticity, temperature decrease or rise causes a change of strain in the rock given by:

$$\varepsilon = -\beta \left(T - T_0\right) \quad \text{.....} \quad (1.7)$$

where β is the volumetric thermal expansion coefficient (at constant *t* and *p*) that indicates the change of strain by the difference of temperature in a rock. An increase in temperature will cause bulk volume increase, whereas a decrease of temperature will cause bulk volume decrease. Since the injection water in geothermal conditions is cold and reservoir temperature is hot, injection leads to tensile stress of rock in the injection well. For typical values such as K=10 GPa and β=10^{-5}/K°, a temperature change of 10 K° induces a thermal stress around 30 MPa.

The conductivity and thermal expansion coefficients do not vary widely because most rock-forming minerals have similar thermal expansion coefficients. The thermal conductivity of rock is in the range of 1 to 10 W/m·K (Jaeger, Cook, and Zimmerman, 2007). An interesting phenomenon regarding the thermal effects in the rock is that the range of the thermal expansion coefficient does not vary significantly with rock type (Grimvall, 1986), in contrast to other rock properties such as porosity and permeability that may vary by many orders of magnitude. McTigue (1986) determined that the thermal expansion coefficient of a fluid-saturated rock is equal to that of the rock skeleton in drained conditions, whereas in undrained conditions, it is:

$$\beta_u = \alpha_s + \phi B\left(\beta_f - \beta_s\right) \quad (1.8)$$

where ϕ and B are the porosity and the Skempton coefficient. The subscripts *s* and *f* indicate the rock skeleton and fluid phase, respectively.

According to linear thermo-elasticity, the strain is the sum of stress-induced strain and thermally induced strain:

$$\varepsilon = \frac{1}{2G}\boldsymbol{\tau} - \frac{\nu}{2G(1+\nu)} trace(\tau)\mathbf{I} - \beta(T - T_0)\mathbf{I} \quad \text{..... (1.9)}$$

where $\boldsymbol{\tau}$ is the relationship of stress and strain in linear elasticity, that is

$$\boldsymbol{\tau} = \lambda\, trace(\tau)\mathbf{I} + 2G\varepsilon \quad \text{..... (1.10)}$$

The governing equation for thermoelasticity is obtained by combining Eq. 1.9 with the stress equilibrium equation, $\tau_{ij,j} = 0$ and the strain-displacement equations.

$$G\nabla^2\mathbf{u} + (\lambda + G)\nabla(\nabla \cdot \mathbf{u}) + 3\beta K \nabla T = 0 \quad \text{..... (1.11)}$$

Fourier's law, $q_T = -k^T \nabla T$ and the energy balance equation for conductive heat transfer equation can be written as

$$\frac{\partial T}{\partial t} = \frac{k^T}{\rho c_p}\nabla^2 T \quad \text{..... (1.12)}$$

The solutions of temperature distribution and displacement can be solved from Eq. 1.11 and Eq. 1.12. Thermo-elasticity has been extended to thermo-poroelasticity, which takes into account the influence of fluid flow and heat transfer. The theory of thermo-poroleasticity will be described in Section 2.

1.2.3 The influence of chemical potential

The effect of chemical potential on water and solute transport is of interest in ultralow-permeability rock such as shale reservoirs. The general concept of chemical interaction in drilling fluid/shale has been studied by experiments (Chenevert, 1970; Hale et al., 1992; Mody and Hale, 1993). They showed that the in and out movement of water and solution between the drilling mud and the shale reservoir alters the pore

pressure distribution, which in turns impacts the effective stresses. The fundamentals of fluid movement in shale can be explained by the difference of chemical potential between the water and shale as shown in Fig. 1.5.

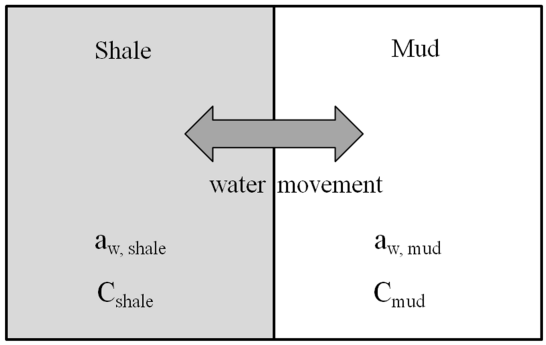

Fig. 1.5. Conceptual scheme of osmosis flow by chemical potential.

A model for chemo-poroelasticity that considers the osmosis, swelling, and solute transport between the drilling mud and pore fluid in the rock based on the Gibbs-Duhem equation in thermodynamics was presented by Heidug and Wong (1996). In this section, we only briefly introduce the general constitutive equations and transport equations for chemo-poroelasticity. Details will be presented in Section 3.

Total stress and pore volume fraction has been introduced by Heidug and Wong (1996); that is (tension positive),

$$\dot{\sigma}_{ij} = L_{ijkl}\dot{\varepsilon}_{kl} - \alpha_{ij}\dot{p} + \sum_{\beta}\omega^{\beta}\dot{\mu}^{\beta}\delta_{ij} \quad \text{.....} \quad (1.13)$$

$$\dot{v} = \alpha\dot{\varepsilon}_{ij} + Q\dot{p} + \sum_{\beta}B^{\beta}\dot{\mu}^{\beta} \quad \text{.....} \quad (1.14)$$

where v is the pore volume fraction, and μ^{β} is the chemical potential of β^{th} chemical component. The elastic stiffness coefficients are the tensor in the case of isotropy, as

$$L_{ijkl} = G\left(\delta_{ik}\delta_{jl} + \delta_{il}\delta_{jk}\right) + \left(K - \frac{2G}{3}\right)\delta_{ij}\delta_{kl}, \quad \text{..... (1.15)}$$

where *K* and *G* denote the bulk and shear modulus, respectively.

The presence of hydraulic pressure and chemical potential cause the change of pore pressure and solute concentration with time. Fluid flux in shale can be written as

$$J_f = -\frac{L^{11}}{\overline{\rho}_f}\nabla p - L^{12}\nabla\left(\mu^S - \mu^D\right), \quad \text{..... (1.16)}$$

where *S* and *D* denote the solid and fluid, and the phenomenological coefficients are defined by:

$$L^{12} = -L^{11}\Re = -\frac{\overline{\rho}_f{}^2 k\Re}{\mu}, \quad \text{..... (1.17)}$$

where *k* and μ are the permeability and viscosity, respectively. $\Re$ is the solute reflection coefficient which may range from 0 to 1.

1.3 Deformation and failure of rock

A number of cases in geothermal and petroleum reservoir operation involve rock deformation and failure caused by fluid flow change. Several different failure criteria are used for its applications (Jaeger, Cook, and Zimmerman, 2007). In this section, we briefly review the strain-stress behavior of rock under stress change, the Coulomb failure criterion, and the effect of pore pressure on rock failure.

1.3.1 Strain-stress curve

The most common tool for studying mechanical behavior of rocks is the uniaxial and triaxial test. It provides the rock properties such as modulus, rock strength, and hysteretic behavior during loading and unloading. In addition, it can estimate the brittle or ductile behavior of rock in a certain conditions of reservoir far-field stress and temperature. The general strain-stress curve for rock under compressive stress is illustrated in Fig. 1.6. In region A-B, the strain-stress behavior is almost elastic and hysteresis may be observed. The stress continues to rise in region B-C but nonlinear behavior, which is called the ductile state, begins at point B, which is the yield stress of the rock. The third region, C-D beginning with the maximum stress at point C leads to large permanent strain change caused by compressive stress, where deterioration of the rock causes a brittle state.

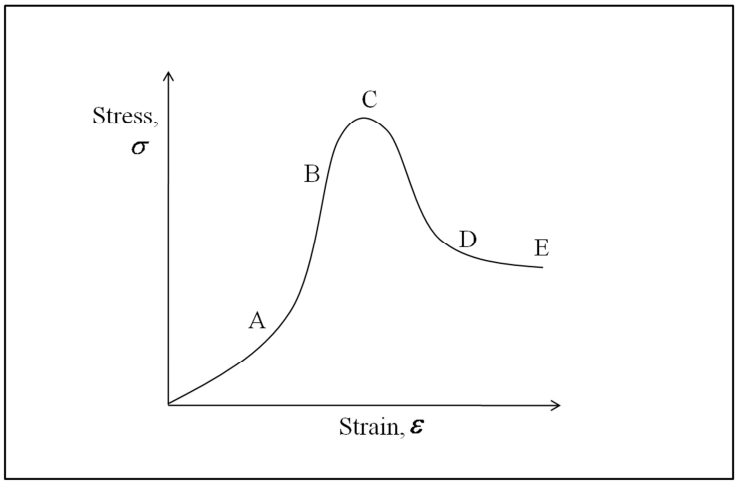

Fig. 1.6. General strain-stress curve for rock under compression.

1.3.2 Coulomb failure criterion

The mostly widely used model for the prediction of rock failure is the Mohr-Coulomb failure criterion. Coulomb (1773) developed the model through experimental investigation, assuming the shear stress along to the plane causes failure. This consideration can be mathematically expressed as

$$|\tau| = S_1 + \mu_s \sigma \quad \text{..... (1.17)}$$

where $|\tau|$ is shear stress, S_1 is finite shear stress, and μ_s and σ are the coefficients of internal friction and normal stress. Eq. 1.17 can be rearranged to the maximum and minimum principal stress as

$$\frac{1}{2}(\sigma_1 - \sigma_3) = S_0 \cos\phi_c + \frac{1}{2}(\sigma_1 - \sigma_3)\sin\phi_c, \quad \text{..... (1.18)}$$

where ϕ_c is the angle of internal friction and σ_1 and σ_3 are the minimum and maximum principal stress.

Understanding tensile failure requires the tension cut-off, $T_{0,}$ which can be measured from a tensile experiment since without a tension cut-off, the Coulomb failure criterion often overestimates the stress state for the failure criterion.

1.3.3 Effects of pore pressure in rock failure

Fluid injection causes rock failure because of the hydraulic pressure and chemical interactions between the rock and the fluid. The mechanical impact with pore

pressure has been developed by Terzaghi (1936). He proposed that the failure of soil can be controlled by the effective principal stress σ'; that is,

$$\sigma = \sigma' - p \quad \text{..... (1.18)}$$

where p is the pore pressure.

Fig. 17 and Fig. 1.8 illustrate the stress state in shear and caused tensile failure by pore fluid pressure. This fluid-induced failure is frequently observed around a borehole during the injection or production operation in geothermal and petroleum reservoirs since they experience significant change of pore pressure around a wellbore.

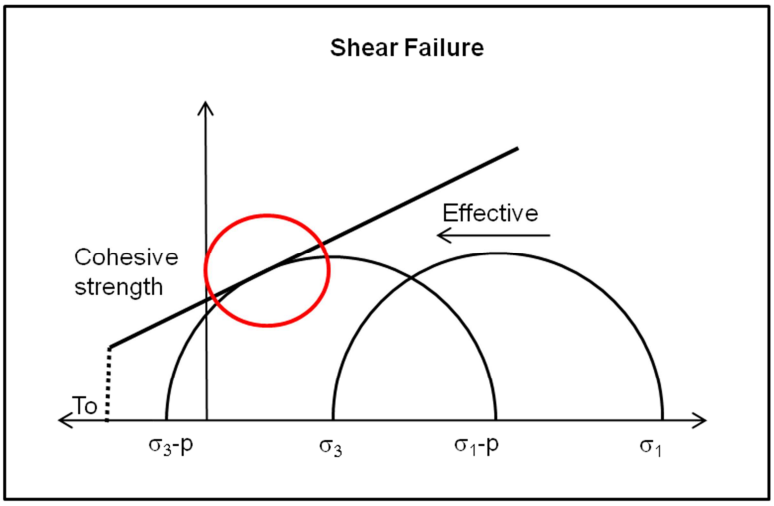

Fig. 1.7. Stress state that satisfies the shear failure curve.

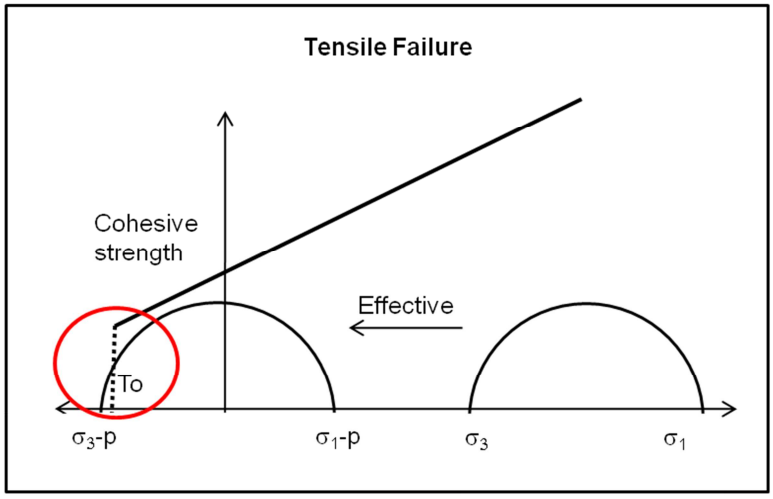

Fig. 1.8. Stress state that satisfies the tensile failure curve.

1.4 Fundamental of continuum damage mechanics

The nonlinear behavior of the rock is of much interest in well stimulation and hydraulic fracturing design in petroleum and enhanced geothermal reservoirs. Stress behavior in triaxial tests shows the hardening and softening process as the vertical compressive stress increases. This nonlinear behavior can also be observed frequently in oil and gas exploration in, for example, sanding problems in unconsolidated reservoirs, reservoir compaction during injection and production, and wellbore stability. More importantly, the process of hydraulic fracturing directly contributes to the nonlinearity of the rock by imposing fluid loading. Traditional poroelasticity cannot capture the hardening and softening behavior after the rock fails, so that it is necessary to consider the nonlinear behavior of rock under the effects of fluid flow, temperature change, and solute transport. In this section, we briefly review the continuum damage mechanics

which illustrate microcracks, microcavities, nucleation, and coalescence. The continuum damage theory phenomenologically accounts for the initial evolution of defects such as nucleation of a certain amount of cracks and void growth during the deformation.

Various damage models have been proposed brittle and ductile materials. These include creep damage, cycle fatigue, and brittle damage (Kachanov, 1986; Lemaitre and Chaboche, 1990; Voyiadjis and Kattan, 1999). Kachanov (1958) first proposed a continuum damage model by introducing effective stress in a fictitious, undamaged configuration. Later researchers extended his theory for ductile material (Lemaitre, 1984, 1985; Murakami, 1988) and brittle material (Krajcinovic and Foneska, 1981; Krajcinovic, 1983, 1996). Ductile materials show a strong plastic deformation, which is the main contributor to the damage evolution and reverse process, so many models for ductile material consider the concepts of coupling between plasticity and damage mechanics (Gurson, 1977; Tvergaard, 1982; Rousselier, 1987; Mahnken, 2002).

The theory of damage in porous rock has been implemented by several researchers (Hamiel et al., 2004; Selvadurai, 2004; Tang et al., 2002). Bart et al. (2000) developed an anisotropic damage model in poroelastic brittle rock and Selvadurai (2004) presented the application of an isotropic damage model in a poroelastic contact problem. Tang et al. (2002) illustrated brittle rock failure under compressive and tensile stress with triaxial tests. They described the sudden drop to the residual stress regime by assuming that strain-stress behavior follows the elasticity theory before the rock failure and the damage theory after the rock failure without considering the hardening process;

instead, rock heterogeneity leads to distributed rock failure (different peak stress in each element), which defines the hardening process in the stress and strain behavior.

Chow and Wang (1987) and Zhao and Roegiers (1993) studied the influence of rock damage on the change in Poisson's ratio. Measurement of the change of compressibility in uniaxial tests of Berea sandstone and Cordoba cream limestone (Zhao and Roegiers, 1993) showed that Poisson's ratio is reduced as the damage variable increases during the rock fracturing progress.

To understand the damage variable, we briefly introduce the physical meaning of damage variable d and its relations of stress change. We assume that the cross-sectional area of the cylindrical bar in the loading condition is A and the area of both cracks and voids (damage in the bar) is A^D. The removal of defects can be considered as a fictitious, undamaged configuration as shown in Fig. 1.9 to use continuum damage mechanics to remove both cracks and voids from the cylindrical bar.

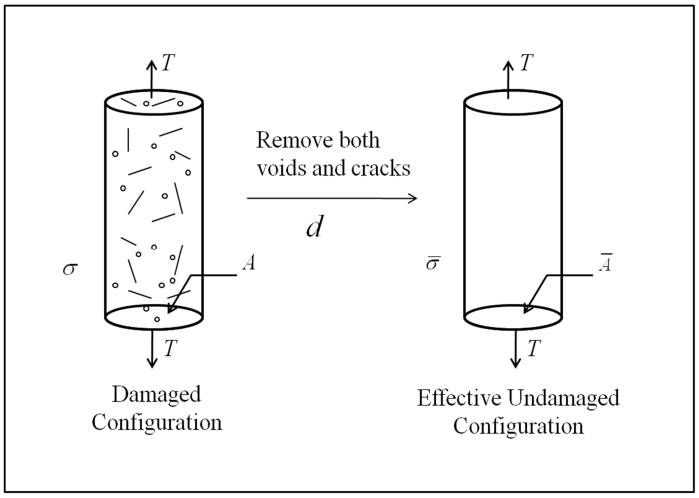

Fig. 1.9. Under uniaxial tension, both voids and cracks are removed in the effective undamaged configuration (Voyiadjis and Kattan, 1999).

The effective configurations of the cross-sectional area and the stress are denoted by $\overline{A}$ and $\overline{\sigma}$, respectively. The effective undamaged configuration of stress can be written as

$$\overline{\sigma} = \frac{\sigma}{1-d}, \quad \text{..... (1.18)}$$

where the damage variable can be described from the continuum damage theory as

$$d = \frac{A-\overline{A}}{A} = \frac{A^D}{A}, \quad \text{..... (1.19)}$$

where $\overline{A}$ is the effective configuration of the cross-sectional area, and A^D is the damaged area. We can formulate the effective configuration of the stress-strain relationship d as

$$\overline{\sigma}_{ij} = \overline{E}_{ijkl}\overline{\varepsilon}^{e}_{kl} \quad \text{..... (1.20)}$$

where $\overline{E}_{ijkl}$ is the elastic moduli tensor for effective configuration of undamaged area and $\overline{\varepsilon}^{e}_{ij}$ is the similar effective strain.

The two theories in the transformation from the nominal to the effective configuration are the strain equivalence hypothesis and the strain energy equivalence hypothesis. Assuming that the strain in normal configuration is the same as in the effective configuration in strain equivalence hypothesis as

$$\varepsilon_{ij} = \overline{\varepsilon}_{ij}, \quad \text{..... (1.21)}$$

we can derive the expression for the relationship of the effective stress and strain configuration with the damage variable as follows:

$$\frac{\sigma}{1-d} = \overline{E}\varepsilon \quad \text{..... (1.22)}$$

$$\frac{E\varepsilon}{1-d} = \overline{E}\varepsilon \quad \text{..... (1.23)}$$

From the hypothesis of strain equivalence ($\varepsilon_{ij} = \bar{\varepsilon}_{ij}$), the relationship of damaged modulus with initial modulus can be written as:

$$E = (1-d)\overline{E} \quad \text{..... (1.24)}$$

The other theory for the transformation relation between the damaged and fictitious undamaged state was proposed by Sidoroff (1981). The theory assumed that the elastic energy in terms of effective configuration and nominal stress are equal; therefore, the elastic strain energies for damage and undamaged configuration are the same:

$$\frac{1}{2}\sigma_{ij}\varepsilon_{ij} = \frac{1}{2}\bar{\sigma}_{ij}\bar{\varepsilon}_{ij} \quad \text{..... (1.25)}$$

The relation of effective and nominal strain can be derived with Eq. 1.24 by substituting Eq. 1.18 such that

$$\bar{\varepsilon}_{ij} = (1-d)\varepsilon_{ij} \quad \text{..... (1.26)}$$

Therefore, by rearranging of Eq. 1.26 and Eq. 1.18, we can obtain the relationship between the initial and damaged modulus,

$$E = (1-d)^2\overline{E} \quad \text{..... (1.27)}$$

1.5 Stress-dependent permeability

One of the interesting physical properties in a rock is permeability. It varies by many orders of magnitude among the various rock types, and it influences the fluid transmissibility in porous rock, which in turns impacts the effective rock stress. Permeability appears to have a relationship with porosity, but that is still highly uncertain because of their complexity in rocks (Ingebritsen and Manning, 2010).

The permeability variations induced by altered stress and rock failure have been studied by many researchers (Shipping et al., 1994; Kiyama et al., 1996; Coste et al., 2001; Zoback and Byerlee, 1975). Zoback and Byerlee (1975) illustrated the relation between permeability change and the evolution of microcracks and voids. Their experimental tests on granite show permeability increases of up to a factor of four during rock deformation. Other studies present different magnitudes for the increase in permeability depending on rock type and conditions (De Paola et al., 2009; Wang and Park, 2002). Stress-dependent permeability has been developed by Elsworth (1989) and Bai and Elsworth (1994, 1999) for fractured media and Bai and Elsworth (1994) for intact rock. They considered equivalent fracture networks and showed the sensitivity of permeability to effective stress with coupled poroelasticity.

The empirical models for the correlations relating the permeability increase to the porosity change have been proposed by several authors (Labrid, 1975; Lund and Fogler, 1976; Lambert, 1981). The Labrid permeability model based on porosity change can be supposed as:

$$\frac{k_0}{k} = M\left(\frac{\phi_0}{\phi}\right)^n , \quad \text{..... (1.28)}$$

where k_0 and ϕ_0 are the initial permeability and porosity, respectively.

Labrid's permeability model based on porosity was extended by Thomas et al. (2003), who proposed that porosity has correlations with strain:

$$-\ln\left[\frac{(1-\phi)}{(1-\phi_0)}\right] = \varepsilon_v , \quad \text{..... (1.29)}$$

where ε_v is the volumetric strain.

The other interesting permeability model considering the shear dilation was developed from Bai and Elsworth (1994):

$$\frac{k}{k_0} = \left\{1 \mp \frac{1}{2}\left[\frac{9(1-\nu^2)^2}{2}\left(\frac{\pi\Delta\sigma}{E}\right)^2\right]^{1/3}\right\}^2 , \quad \text{..... (1.30)}$$

where the alternate negative and positive sign denote compression and dilatational loading.

Tang et al. (2002) developed a stress-dependent permeability model based on effective stress that accounts for the permeability increase under shear and tensile failure. There model emerged from experimental observation in triaxial tests with fluid in and out through the core sample.

For undamaged rock:

$$k = k_0 \exp-\left[\beta_d\left(\sigma_{ii}/3 - \alpha p\right)\right] \quad \text{..... (1.31)}$$

For damaged rock:

$$k = \xi_d \, k_0 \exp\left[-\beta_d \left(\sigma_{ii}/3 - \alpha p\right)\right] \quad (1.32)$$

where ξ_d is the increasing factor after the rock failure and β_d represents the sensitivity of permeability in exponential decay by compression.

Permeability anisotropy is a key factor in the reservoir fluid path that can be caused by in-situ stress anisotropy. Experimental studies have shown that the permeability behaves isotropically under isotropic loading, whereas anisotropy becomes larger with anisotropic loading in core analysis (Bruno et al., 1991; Rhett et al., 1992; Ruistuen et al., 1996). From the experimental results of permeability behavior under stress variations, we can infer that reservoir permeability is dependent on the deviatoric far-field stress. Khan and Teufel (2000) illustrated the change of permeability anisotropy with respect to pore pressure variations and far-field stresses. They concluded that the maximum permeability direction is parallel to the maximum principal stress, and the permeability anisotropy increases as the deviatoric stress increases.

1.6 Injection-induced microseismicity

In geological formations, earthquakes are occasionally caused by redistribution of the in-situ earth stresses in the rock mass. The interest in monitoring microseismic events during injection and production has increased over the past several years since it can be used as a tool to predict the natural fracture distribution and reservoir rock properties such as permeability and rock strength. Once injection and production begin in geothermal or oil and gas exploration, the pore pressures increase in the injection well

and decrease in the production well. This change of pore pressure triggers earthquake activity by both shear and tensile failure as shown in Fig. 1.10.

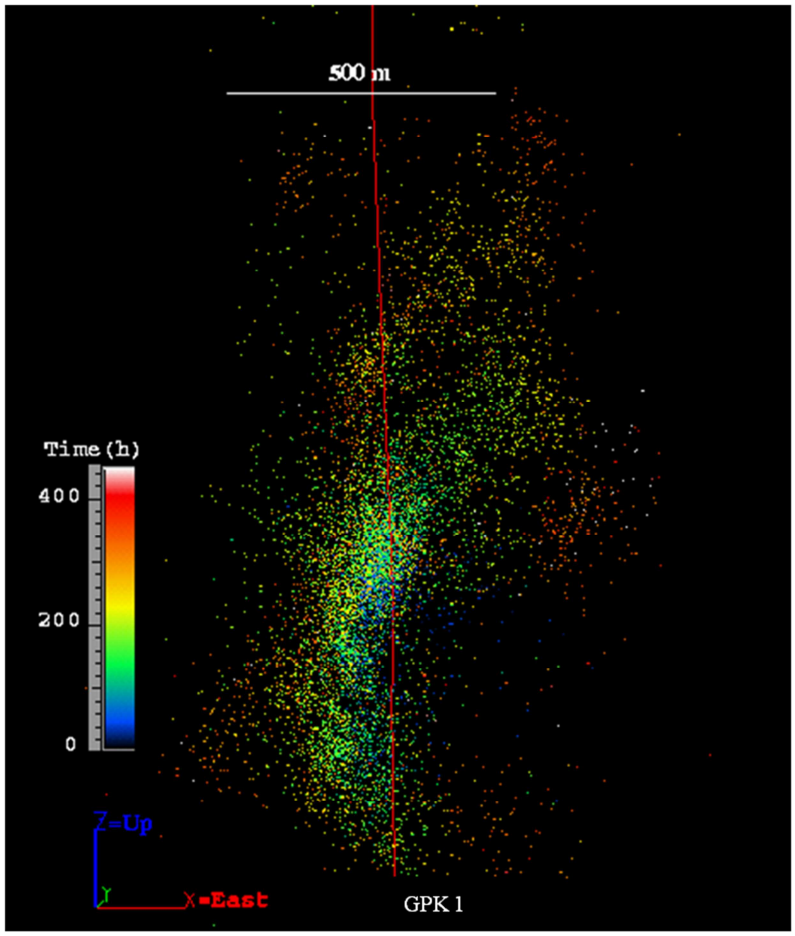

Fig. 1.10. Microseismic events induced during the injection experiments of the Soultz-Sous-Forets reservoir.

Efforts to estimate reservoir properties during fluid injection and extraction have progressed by several researchers (Talwani and Acree, 1985; Shapiro et al., 1997; 1999; 2002; Adushkin et al., 2000; Fehler et al., 2001). Microseismic event detection and

interpretation are used for estimating the stimulated volume; resulting fracture growth, reservoir permeability, and geometry of the geological structures; and the in-situ stress state (Pine, 1984). The process commonly is referred to as seismicity-based reservoir characterization. Progress has been made in quantitative and qualitative analysis of reservoir stimulation using microseismic events (Shapiro et al., 1997, 1999, 2002; Rothert and Shapiro, 2003). They demonstrated numerical simulations based on a fluid diffusion model with a permeability tensor, assuming microseismic events are triggered if the pore pressure exceeds certain threshold values. However, rock failure and permeability change were not considered. Also, in-situ stress and thermal effects on fluid-rock interaction have not been considered. Generally, the induced seismicity occurs more frequently by fluid injection if the cracks, natural fractures, and faults exist and are subjected to excess shear. Bruel (2002) and Baisch et al. (2003) considered shear failure by fluid injection in naturally fractured reservoirs, and Safari and Ghassemi (2011) showed thermo-poroelastic analysis of microseismicity, which considered the fluid flow and fracture deformation by injection/extraction in geothermal reservoirs. Hydraulic fracturing also induces microseismicity. Fracturing is accompanied by tensile failure, which contrasts with shear induced failure (although shear failure can also be present in the vicinity of the hydraulic fracturing). It creates high energy for monitoring tensile failure so that it can be a tool for predicting the intended fractured volume.

1.7 Heterogeneous model

Rocks are heterogeneous, with natural weaknesses such as pre-existing cracks, voids, and grain boundaries. The variations of pore pressure and temperature during fluid injection can induce fractures at these defects, resulting in rock failure and fracture propagation. Muller et al. (2009) conducted stochastic borehole stability analysis using probability distribution functions for rock and reservoir properties such as bulk and shear modulus, far-field stress, initial pore pressure, and tension cutoff. They assumed the stochastic parameters follow lognormal and normal distributions which are widely used in heterogeneous reservoir simulations. The other probability function in geomechanics simulation is the Weibull distribution function (Weibull, 1951; Fang and Harrison, 2002; Tang et al., 2002; Gharahbagh and Fakhimi, 2010; Min et al., 2011), defined as

$$\varphi = \frac{n}{s_0}\left(\frac{s}{s_0}\right)^{n-1} \exp\left[-\left(\frac{s}{s_0}\right)^{n}\right] \quad \text{..... (4.10)}$$

where s in the variables s_0 represents the corresponding mean value. The shape parameter n determines the deviation from the mean value. The range of n is from 1 to infinity. If n increases, statistical deviations become narrow and the rock is homogeneous. Most rock properties, such as modulus and porosity, are heterogeneous because of the rock's components and origin, and numerical modeling needs to depict this initial heterogeneity. The Weibull distribution function can be used to generate an initial property distribution for numerical modeling. Also, the deviations of rock properties from the mean values are important. These deviations can be assumed as

flaws in unit volume; therefore, homogeneous rock can be modeled with high value of *n*, and heterogeneity (flaws in unit volume) increase as *n* decreases.

1.7.1 Stochastic model

To approach realistic reservoir properties and conditions, many stochastic approaches have been developed to accommodate small and large-scale heterogeneities in reservoir simulations (Knutson, 1976; Smith and Morgan, 1986; Liu, 2006). The two main streams in stochastical approaches are the discrete and continuum models.

The discrete model considers discrete geological features such as naturally pre-existing fracture and faults in spatial distributions. Ezzedine (2010) presented stochastic discrete fracture network numerical model using Monte Carlo realizations and Cacas et al. (1990) proposed stochastic particle trajectories of flow patterns in fractured rock incorporating intersections with the network pipes model. Liu (2006) developed multiple-point simulations based on the Bayesian updating correction, and demonstrated the influence of geostatistical model parameters, number of replicates, and grid-scale.

The other stochastic approach is the continuum model. This model describes the mean level, deviations from the mean values, and how strongly typical properties are related with other neighboring points. Some key concepts are random distribution functions such as Gaussian, Weibull, and log-normal distribution functions, and the model has been applied to the rock mechanics and reservoir simulations (Muller et al., 2009; Tang et al., 2002; Voss, 1985; Hewett, 1986).

The discrete models are better suited for modeling large-scale heterogeneous reservoirs to describe the discontinuities of rock mass. The continuous models are well-suited for geomechanical modeling of rock properties, assuming typical probability distributions with stationary change. The approach for describing the heterogeneity in this work is the continuum model which considers the deviation from the mean values based on Weibull distribution function.

1.7.2 Mesh size sensitivity for heterogeneous models

It is critical to consider the influence of mesh scale to model spatial distribution of geological media. Especially to describe the discontinuity of reservoir rocks, the mesh generation and size selection become more important problems. Liu (2006) tested geostatistical modeling with different scales and found good agreement between a finer-scale mesh and a training model that assumed a synthetic spatial distribution for channels in sinuous sand and shale. Similarly, for crack propagation modeling, mesh size is crucial to differentiate stress distribution during loading. Liang (2005) presented a strain-stress curve with different mesh sizes representing the heterogeneity of rock distributions. Fig. 1.11 shows the influence of mesh size for the numerical modeling of fracture propagation in heterogeneous media. The stress field in the coarse mesh can smear out the stress concentration near the crack tip, so it causes difficulty for geomechanical simulations. The finer mesh is suitable for describing the realistic spatial distribution; however, it requires extensive computational memory and CPU costs.

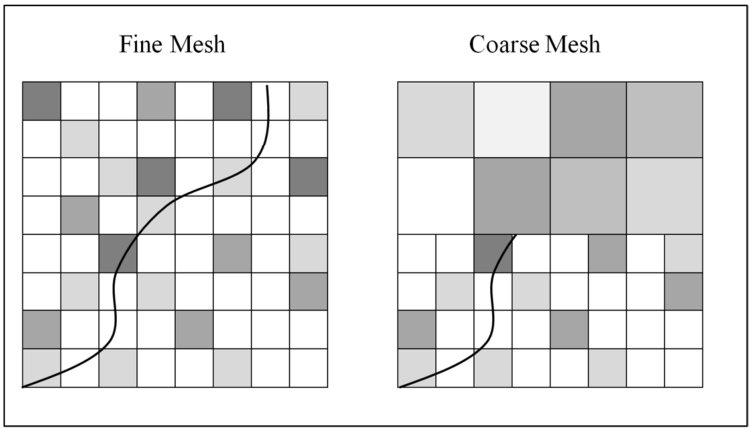

Fig. 1.11. The influence of mesh size on crack propagation in heterogeneous media (Liang, 2005).

A selection of optimum mesh size for geomechanical simulation is dependent on the local distribution of the reservoir properties and fluid injection conditions. Especially for the wellbore stability problem, the mud pressure is maintained in between the initial pore pressure and the fracture gradient to avoid well collapse and severe distortion. The mesh for numerical modeling for wellbore stability must be finer near the wellbore to capture the variations of stress, pore pressure, and temperature; however, the changes of pore pressure and temperature are small in the range far from the wellbore (~5m), so the large element size is suitable. The design of mesh size should be based on how significant the spatial variations of variables are. Also, loading conditions such as fluid injection and the difference of temperature between the injection fluid and reservoir are key factors in constructing the mesh size; too large mesh sizes and too high heat transfer rates can cause numerical oscillation for temperature distribution.

1.8 Summary of dissertation

This dissertation consists of eight sections. Section 1 introduces the objective of this research with review of previous development of the influence of fluid flow, temperature, and solute transport. In addition, continuum damage mechanics, stress-dependent permeability, and injection-induced microseismicity are reviewed.

Section 2 describes the theory of poroelasticity, thermo-poroelasticity, and chemo-poroelasticity. It consists of the constitutive relations, transport of fluid flow, temperature, and solute transport. The Navier-type governing equations are derived with constitutive and transport equations.

Section 3 contains the procedure for numerical implementation of coupled problems using finite element methods, and presents the verifications and examples for the influence of fluid flow, temperature, and solute transport.

Section 4 shows the application of damage mechanics and the stress-dependent permeability model using finite element methods. Numerical modeling for the triaxial test has been performed to obtain the parameters for nonlinear behavior of the rock and permeability models which are compared with experimental triaxial tests.

Section 5 presents wellbore stability in shale reservoir drilling with chemo-thermo-poro-mechanics using finite element methods. Damage mechanics and stress-dependent permeability model are introduced. The influence of solute transport and thermal stress on rock damage is discussed.

Section 6 describes the two-dimensional finite element analysis for well stimulation with thermo-poro-mechanics. Heterogeneous modulus and permeability

distributions are considered to simulate rock failure and microseismic event propagation. Two types of injection methods are presented in this section: injection geometry for well-scale simulation and the point-source method for reservoir-scale simulation.

Section 7 is the three-dimensional extension of finite element methods in well-scale simulation. It has been performed under normal, strike-slip, and thrust stress regimes so that the shape of damage propagation during fluid injection is affected by far-field stress. The heterogeneous modulus and permeability have been considered to simulate injection-induced microseismic event propagation.

Section 8 describes three-dimensional finite element modeling for reservoir-scale simulation with point source injection. The results for the influence of stress regime in microseismic events propagation are presented. Then critical factors for injection-induced microseismicity clouds pattern is presented.

Finally, in Section 9, the dissertation will be concluded and future work will be outlined.

2. THE THEORY OF POROELASTICITY AND ITS EXTENSIONS

The influence of fluid flow in a porous rock was initially recognized in the soil consolidation problem. The one-dimensional consolidation problem, which takes into account the pore pressure in soil, was developed by Terzaghi (1923), who demonstrated that the total stress concept consists of effective stress and pore pressure. Biot (1941) developed a coupled fluid/solid interaction model that assumed that the soil is homogeneous and water is incompressible, and used Darcy's law for fluid flow. The linear poroelasticity was extended to combined thermal and hydraulic stress (McTigue, 1986; Kurashige, 1989). Also the relation of chemical potential and rock deformation has been developed on the basis of the thermodynamic law and the Gibbs-Duhem equation (Mody and Hale, 1993; Heidug and Wong, 1996; Ghassemi and Diek, 2003; Ghassemi et al., 2009; Zhou and Ghassemi, 2009). The sign convention in this section follows positive tension.

2.1 Poroelasticity

The linear poroelasticity introduces the coupled interaction between the rock deformation and pore pressure variations. The change of pore pressure causes rock deformation and also rock could be deformed by fluid flow.

2.1.1 Constitutive equations

The relation between the solid (ε_{ij}) and fluid (ζ), the stress and pore pressure can be described as:

$$\varepsilon_{ij} = \frac{\sigma_{ij}}{2G} - \left(\frac{1}{6G} - \frac{1}{9K}\right)\delta_{ij}\sigma_{kk} + \frac{1}{3H'}\delta_{ij}p \quad (i = 1,2,3 \quad j = 1,2,3) \quad \text{.....} \quad (2.1)$$

$$\zeta = \frac{\sigma_{kk}}{3H''} + \frac{p}{R'} \quad \text{.....} \quad (2.2)$$

where the K and G are the bulk and shear modulus of the drained elastic solid. The constants H', H'' and R' denote the coupling between the solid and fluid stress and strain.

The change of strain by pore pressure is equal to the fluid contents change caused by the increase of volumetric stress:

$$\frac{\partial \varepsilon_{ij}}{\partial p} = \frac{\partial \zeta}{\partial \sigma_{ij}} \quad \text{.....} \quad (2.3)$$

The poroelastic coupling parameters can be defined as (Rice and Cleary, 1976; Detournay and Cheng, 1993)

$$R' = \frac{2G(1+\nu)(\nu_u - \nu)}{\alpha^2(1-2\nu)^2(1+\nu_v)} \quad \text{.....} \quad (2.4)$$

$$H' = H'' = \frac{2G(1+\nu)}{2\alpha(1-2\nu)} \quad \text{.....} \quad (2.5)$$

Substituting Eq. 2.4 and Eq. 2.5 into Eqs. 2.1 and 2.2:

$$\varepsilon_{ij} = \frac{\sigma_{ij}}{2G} - \frac{\nu}{2G(1+\nu)}\delta_{ij}\sigma_{kk} + \frac{\alpha(1-2\nu)}{2G(1+\nu)}\delta_{ij}p \quad \text{.....} \quad (2.6)$$

$$\zeta = \frac{\alpha(1-2\nu)}{2G(1+\nu)}\sigma_{kk} + \frac{\alpha^2(1-2\nu)^2(1+\nu_u)}{2G(1+\nu)(\nu_u-\nu)}\,p \quad \text{..... (2.7)}$$

After rearranging Eq. 2.6 and Eq. 2.7 to include the stress σ_{ij} and pore pressure p, we obtain:

$$\sigma_{ij} = 2Ge_{ij} + \frac{2G\nu}{1-2\nu}\delta_{ij}e - \alpha\delta_{ij}p \quad \text{..... (2.8)}$$

$$p = -\frac{2GB(1+\nu_u)}{3(1-2\nu_u)}e + \frac{2GB^2(1-2\nu)(1+\nu_u)^2}{9(\nu_u-\nu)(1-2\nu_u)}\zeta \quad \text{..... (2.9)}$$

where *B* is the Skempton pore pressure coefficient is defined by:

$$B = \frac{3(\nu_u-\nu)}{2(1-2\nu_u)(1+\nu_u)}.$$

2.1.2 Field equations

To solve the solutions for the stress and pore pressure, the balance equation for stress and fluid flow with Darcy's law are also necessary.

The equilibrium equations:

$$\sigma_{ij,j} = 0 \quad \text{..... (2.10)}$$

The fluid mass balance equation can be written as:

$$\dot{\zeta} + q_{i,i} = 0 \quad \text{..... (2.11)}$$

where q_i is the specific discharge vector which has a relation with Darcy's law:

$$q_i = -\frac{k}{\mu}p_{,i} \quad \text{..... (2.12)}$$

The governing equation for solids is obtained from Eqs. 2.8 and 2.10 as

$$G\nabla^2 u_i + \frac{G}{1-2\nu_u} u_{k,ki} - \alpha p_{,i} = 0 \quad \text{..... (2.13)}$$

After substituting Eq. 2.7 into Eq. 2.11 with Darcy's law (Eq. 2.11), the governing equation for fluid can be derived:

$$\dot{\zeta} - c_f \nabla^2 \zeta = 0 \quad \text{..... (2.14)}$$

where $c_f = \frac{2kB^2 G(1-\nu)(1+\nu_u)^2}{9\mu(1-\nu_u)(\nu_u-\nu)}$ is the fluid diffusion coefficient. Substituting Eq. 2.7 into Eq. 2.9:

$$\dot{p} - kM\nabla^2 p = -M\alpha\dot{e} \quad \text{..... (2.15)}$$

where $M = \frac{2G(\nu_u-\nu)}{\alpha(1-2\nu_u)(1-2\nu)}$ is the Biot modulus (similar to a storage coefficient) defined as the change of fluid contents per unit volume as a result of pore pressure variation under constant volumetric strain.

2.2 Thermo-poroelasticity

Nonisothermal conditions often arise when geothermal reservoir or steam assisted gravity drainage (SAGD) is used to enhance oil recovery. The difference of heat expansion coefficients between the rock and fluid cause rock deformation and pore pressure. The governing equations for thermo-poroelasticity were developed by McTigue (1986), assuming fully-saturated homogeneous rock.

2.2.1 Constitutive equations

The constitutive equations considering the relations of the strain, pore pressure, and temperature change were developed from the thermoelasticity and poroelsticity (McTigue, 1986):

$$\sigma_{ij} = 2Ge_{ij} + \frac{2Gv}{1-2v}\delta_{ij}e_{kk} - \alpha\delta_{ij}p - K\beta_s\delta_{ij}\Delta T \quad \text{..... (2.16)}$$

$$\zeta = \frac{\alpha(1-2v)}{2G(1+v)}\sigma_{kk} + \frac{\alpha^2(1-2v)^2(1+v_u)}{2G(1+v)(v_u-v)}p - \phi(\beta_f - \beta_S)\Delta T \quad \text{..... (2.17)}$$

where K is the bulk modulus, β_f and β_s are the volumetric thermal expansion coefficient for fluid and solid, respectively.

2.2.2 Field equations

Similarly from the poroelasticity derivations, the thermo-poroelastic governing equation can be derived from the constitutive equations and transport equations. We can obtain the governing equation for the solid from Eq. 2.16 and Eq. 2.10:

$$G\nabla^2 u_i + \frac{G}{1-2v_u}u_{k,ki} - \alpha p_{,i} + K\beta_S\,\delta_{ij}\,\Delta T = 0 \quad \text{..... (2.18)}$$

The governing equation for the fluid can be derived by putting Eq. 2.17 into Eq. 2.11 with Darcy's law:

$$\dot{p} - kM\nabla^2 p = -M\alpha\dot{e} + (\alpha\beta_f + \beta_S)\Delta\dot{T} \quad \text{..... (2.19)}$$

The heat transfer equation is obtained by combining the Fourier's law and energy balance equation:

$$Q_i = -k^T T_{,i} \quad \text{..... (2.20)}$$

$$\rho_m c_p \dot{T} + Q_{i,i} = 0 \quad \text{..... (2.21)}$$

where Q_i is the heat flux and k^T is the thermal conductivity. ρ_m and c_p are the total mass density and specific heat capacity.

Substituting Eq. 2.20 into Eq. 2.21 can obtain the heat transfer equation.

$$\dot{T} = c_T \nabla^2 T \quad \text{..... (2.22)}$$

where $c_T = \dfrac{k^T}{\rho_m c_p}$ is the thermal diffusivity.

2.3 Chemo-poroelasticity

Chemical interaction in shale plays a key role in pore pressure distribution and effective rock stress. Ghassemi and Dike (2003) showed that the solute transport is several times higher than hydraulic pressure at certain conditions. In osmotic flow, the difference of water activity caused by chemical potential influences the solute transport. Sherwood and Baily (1994) proposed the constitutive equations for the chemically induced fluid flow, and Heidug and Wong (1996) developed Biot-like constitutive equations based on irreversible thermodynamics. Ghassemi and Diek (2003) developed a

linear version for chemo-elasticity to improve the nonlinearity problem between the stress and solute concentration.

2.3.1 Constitutive equations

The constitutive relation for stress can be described with strain, fluid content, and solute concentration (Tao, 2000; Ghassemi and Diek, 2003):

$$\sigma_{ij} = 2Ge_{ij} + \frac{2Gv}{1-2v}\delta_{ij}e_{kk} - \alpha'\delta_{ij}\,p + \frac{\omega_0 x\delta_{ij}\dot{C}^S}{\overline{C}^S} \quad \text{..... (2.23)}$$

$$\zeta = \alpha e_{kk} + \left(\frac{1}{M} + \frac{M^S\omega_0(\alpha-1)}{K\overline{C}^D RT_0\overline{\rho}_f}\right)p + \frac{\chi\omega_0(\alpha-1)}{K}\frac{C^S}{\overline{C}^S} \quad \text{..... (2.24)}$$

where α' and χ are defined by:

$$\alpha' = \left(\alpha - \frac{M^S w_0}{\overline{C}^D RT_0\overline{\rho}_f}\right) \text{ and } \quad \chi = 1 - \frac{\overline{C}^S}{\overline{C}^D}$$

$\overline{C}^S$ are $\overline{C}^D$ the mean values of solute and diluent mass concentration, respectively, T_0 the average absolute temperature, $\overline{\rho}_f$ the average fluid density, R the universal gas constant, and M^S the molar mass fraction of the solute.

2.3.2 Transport equations

Assuming that the system is isothermal and binary electrolyte solution. The fluid and solute flux can be described with the gradient of pore pressure and solute concentration:

$$J^f = -\frac{k\overline{\rho}_f}{\mu}\left(p_{,i} - \frac{\Re\overline{\rho}_f RT_0}{M^S \overline{C}^S \overline{C}^D} \right) \quad \text{..... (2.25)}$$

$$J^S = -\overline{\rho}_f D^S \nabla C^S_{,i} \quad \text{..... (2.26)}$$

where $\Re$ denote the reflection coefficient, J^f and J^S are the flux for fluid flow and solute, respectively, and D^S the solute diffusivity.

The balance equation for fluid flow and solute transport can be written as

$$\overline{\rho}_f \dot{\zeta} + \nabla \cdot J^f \quad \text{..... (2.27)}$$

$$\phi\overline{\rho}_f \dot{C}^S + \nabla \cdot J^S \quad \text{..... (2.28)}$$

2.3.3 Field equations

The constitutive equation for chemo-elasticity (Eq. 2.23) with equilibrium equation derives the governing equation:

$$G\nabla^2 u_i + \frac{G}{1-2v_u} u_{k,ki} - \alpha p_{,i} + \omega_0 x a C^S_{,i} = 0 \quad \text{..... (2.29)}$$

The solute diffusion equation can be obtained by combining the solute transport equation (Eq. 2.26) with mass balance equation (Eq. 2.28) as:

$$\dot{C}^S = \frac{D^S}{\phi}\nabla^2 C^S \quad \text{..... (2.30)}$$

The coupled fluid diffusion equation can be obtained by combining the fluid content constitutive equation (Eq. 2.24) with conservation equations:

$$c'\nabla^2 p - \dot{p} = -c''\dot{C}^S \quad \text{..... (2.31)}$$

where

$$c' = \frac{c^f}{1-c_0}$$

$$c'' = \frac{RT\overline{\rho}_f}{M^S}\left[\frac{\overline{C}^D c_0 x}{\overline{C}^S(1-c_0)} - \frac{\Re c^f \phi}{(1-c_0)\overline{C}^S\overline{C}^D D^S}\right]$$

$$c_0 = \frac{\mu c^f}{k}\left[\frac{1}{K} - \frac{2\eta(1-2v)}{G(1+v)}\right]\frac{\omega_0 M^S}{\overline{C}^D RT\overline{\rho}_{f\,0}}$$

$$c^f = \frac{2kG(1-v)(v_u - v)}{\alpha^2(1-v_u)(1-v)^2}$$

3. FINITE ELEMENT METHOD FOR COUPLED PROBLEM AND ITS VERIFICATIONS

Section 2 described mathematical models for coupled fluid flow, temperature, and solute transport in rock deformation. This section describes the finite element method for coupled problems and its verification. The finite element method is one of the discretizing techniques for solving partial-differential equations. The method has been developed by many researchers (Zienkiewicz and Taylor, 1991; Strang and Fix, 1973; Cook et al., 2001). Finite element discretization for coupled problems for coupled solid-fluid interaction is described by several authors (Smith and Griffiths, 2004; Zienkiewicz and Taylor, 1991; Lewis and Schrefler, 1988).

3.1 Finite element formulations

3.1.1 Basics for discretization

In the finite element method, continuous variables such as displacement u, pore pressure p, temperature T, and solute concentration C^S can be approximated by $\tilde{u}$, $\tilde{p}$, $\tilde{T}$, and, $\tilde{C}^S$, in terms of their nodal values, interpolating the nodal to nodal values by shape functions. Considering a two-dimensional quadrilateral element or a three-dimensional hexahedron element (Fig. 3.1), the interpolation functions can be written as:

$$\tilde{u} = \sum_{i=1}^{q} N_i u_i \quad \text{.....} \quad (3.1)$$

$$\tilde{p} = \sum_{i=1}^{q} N_i p_i \quad \text{.....} \quad (3.2)$$

$$\tilde{T} = \sum_{i=1}^{q} N_i T_i \quad \text{.....} \quad (3.3)$$

$$\tilde{C}^S = \sum_{i=1}^{q} N_i C_i^S \quad \text{.....} \quad (3.4)$$

where $\tilde{u}$, $\tilde{p}$, $\tilde{T}$ and $\tilde{C}^S$ are approximated in terms of their nodal values u_i, p_i, T_i, and C_i^S in the system. N_i is the interpolation function and is generally referred to as a shape function where subscript "*i*" denotes the corresponding node.

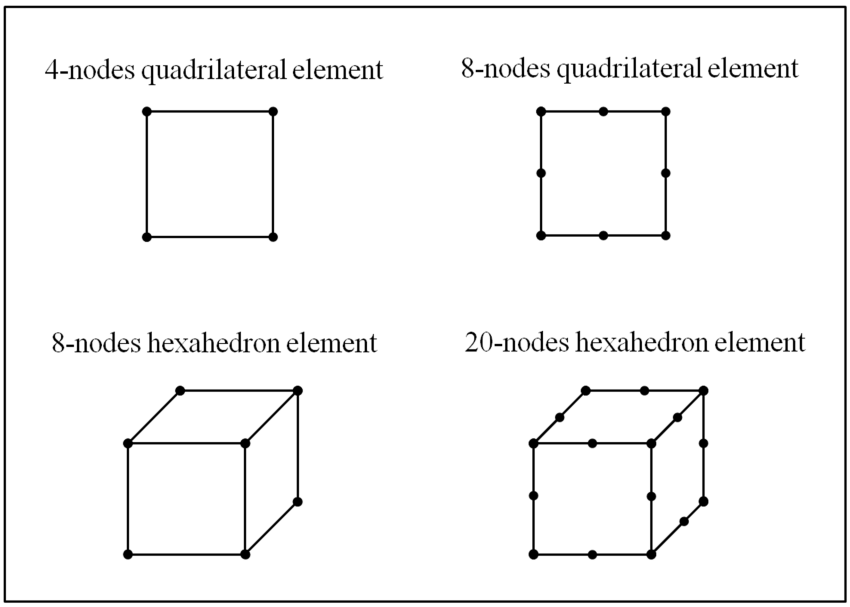

Fig. 3.1. Types of elements used for the finite element method.

The shape functions are often taken to be polynomials that depend on element type and the number of nodes in the element. Several types of shape functions for two-dimensional and three-dimensional elements are shown in Fig. 3.2 and Fig. 3.3.

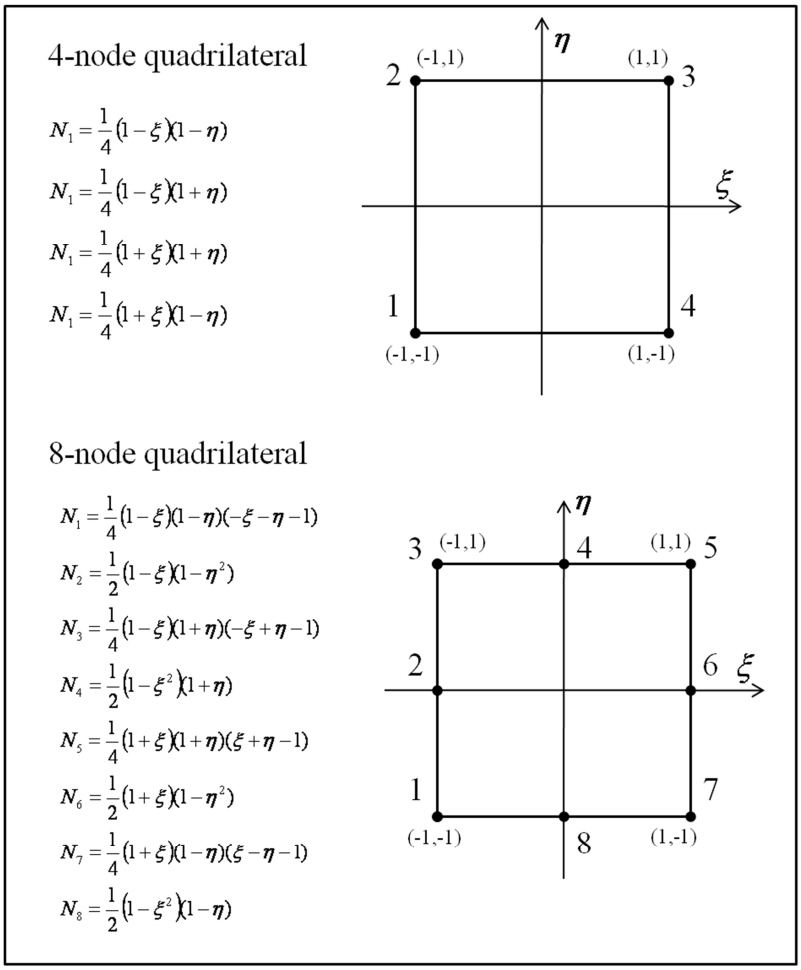

Fig. 3.2. Shape functions for two-dimensional 4-node and 8-node quadrilateral element.

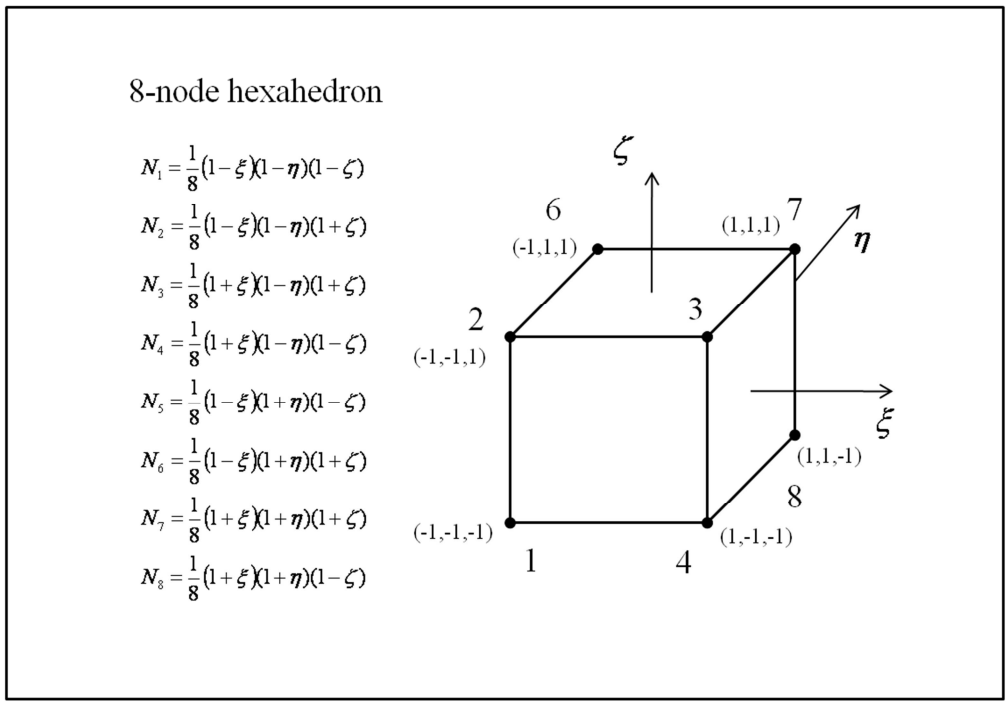

Fig. 3.3. Shape function for the case of three-dimensional 8-node hexahedron element.

The choice of shape function and element type varies depending on the purpose of the simulations. Especially for solving the mixed forms of finite element formulations, Zienkiewicz and Taylor (1991) presented a “patch test” to test the numerical stability of several types of element in two-dimensional coupled problems. They showed that finite element solutions are stable when the variable configurations are 8 nodes for displacement and 4 nodes for pore pressure in each element for a two-dimensional, quadrilateral element. For corresponding three-dimensional expansion, configurations for the variables are 20 nodes for displacement and 8 nodes for pore pressure in a hexahedron element. From a practical point of view, the numerical stability becomes critical around a wellbore because of significant gradients of pore pressure, temperature,

and rock deformation by fluid injection. Lewis and Schrefler (1988) also suggested a degree of freedom in each element two times higher for displacement nodes than pore pressure and temperature to obtain more accurate finite element results. The limitations of element types for finite element approximations are related with ill-posed shape functions that cause the singularity problem which is divided by zero in numerical modeling, and the criterions of the stability is analyzed from Babuska (1971, 1973) and Brezzi (1974).

Since the shape functions are defined in a local coordinate system (ξ,η), it is necessary to describe the relation between the global (x, y) and local coordinate (ξ,η) system. For example, the coordinate transformation for the four-node quadrilateral element can be written as:

$$\begin{aligned} x &= N_1x_1 + N_2x_2 + N_3x_3 + N_4x_4 = [\mathbf{N}]\{\mathbf{x}\} \\ y &= N_1y_1 + N_2y_2 + N_3y_3 + N_4y_4 = [\mathbf{N}]\{\mathbf{y}\} \end{aligned} \quad \text{..... (3.5)}$$

where $[\mathbf{N}]$ denotes the shape function vector as described in (Fig. 3.2) and $\{\mathbf{x}\}$ and $\{\mathbf{y}\}$ are the nodal coordinates in the global coordinate system.

The other necessary coordinate transformation is the derivatives from the local to global coordinate, which can be described by the chain rule of the partial differentiation:

$$\begin{Bmatrix} \dfrac{\partial}{\partial\xi} \\ \dfrac{\partial}{\partial\eta} \end{Bmatrix} = \begin{bmatrix} \dfrac{\partial x}{\partial\xi} & \dfrac{\partial y}{\partial\xi} \\ \dfrac{\partial x}{\partial\eta} & \dfrac{\partial y}{\partial\eta} \end{bmatrix} \begin{Bmatrix} \dfrac{\partial}{\partial x} \\ \dfrac{\partial}{\partial y} \end{Bmatrix} = [\mathbf{J}] \begin{Bmatrix} \dfrac{\partial}{\partial x} \\ \dfrac{\partial}{\partial y} \end{Bmatrix} \quad \text{..... (3.6)}$$

or

$$\begin{Bmatrix} \frac{\partial}{\partial x} \\ \frac{\partial}{\partial y} \end{Bmatrix} = [\mathbf{J}]^{-1} \begin{Bmatrix} \frac{\partial}{\partial \xi} \\ \frac{\partial}{\partial \eta} \end{Bmatrix} \quad \text{.....} \quad (3.7)$$

where $[\mathbf{J}]$ is the Jacobian matrix.

To solve a partial differential equation (Eqs. 3.10 to 3.13), it is necessary to understand the procedure for numerical integration (Eqs. 3.18 to 3.31) of the weighting residual by each shape function by integrating over the equations (Galerkin's method). The transformation between the local Jacobian coordinate and the global coordinate in integration should be evaluated as follow:

$$\iint dxdy = \int_{-1}^{1}\int_{-1}^{1} \det|\mathbf{J}| d\xi d\eta \quad \text{.....} \quad (3.8)$$

The Gauss-Legendre quadrature for finite element numerical integration in two dimensions can be described as:

$$\begin{aligned} &\int_{-1}^{1}\int_{-1}^{1} f(\xi,\eta)\det|\mathbf{J}| d\xi d\eta \approx \sum_{i=1}^{n}\sum_{j=1}^{n} w_i w_j f(\xi_i,\eta_i) \\ &\approx \sum_{i=1}^{nip} W_i f(\xi,\eta)_i \end{aligned} \quad \text{.....} \quad (3.9)$$

where *nip* is the total number of integration points (Gaussian point), w_i and w_j are the weighting coefficients, and (ξ_i,η_i) are sampling points in element.

3.1.2 Spatial discretization

For the case of chemo-thermo-poroelasticity, the combining the constitutive equations and the balance equations with transport equations yield the governing equations:

$$\left(K+\frac{G}{3}\right)\nabla(\nabla\cdot\mathbf{u})+G\nabla^2\mathbf{u}+m\left(\alpha'\nabla p-\chi\nabla C^S+\gamma_1\nabla T\right)=0 \quad \text{..... (3.10)}$$

$$\alpha(\nabla\cdot\dot{\mathbf{u}})+\beta'\dot{p}+\chi'\dot{C}^S+\gamma_2\dot{T}-\frac{k}{\mu}\nabla^2 p+\frac{k}{\mu}L_D\nabla^2 C^2=0 \quad \text{..... (3.11)}$$

$$\phi\dot{C}^S-D^S\nabla^2 C^S-C^S D^T\nabla^2 T=0 \quad \text{..... (3.12)}$$

$$\dot{T}-c^T\nabla^2 T=0 \quad \text{..... (3.13)}$$

where K and G are bulk and shear modulus, respectively, α Biot's constant, μ viscosity. α' , χ , χ' , γ_1 , γ_2 , and β' are given by:

$$\alpha'=\alpha-\frac{M^S\omega_0}{\overline{\rho}_f RTC^D}$$

$$\beta'=\frac{\alpha-\phi}{K_s}+\frac{\phi}{K_f}+\frac{\omega_0(\alpha-1)M^S}{\overline{\rho}_f KRC^D T}$$

$$\chi'=\frac{\alpha-1}{K}\chi$$

$$\gamma_1=K\alpha_s$$

$$\gamma_2=\alpha\beta_s+(\beta_f-\beta_s)\phi$$

where M^S is molar mass of the solute, ω_0 the swelling coefficient, $\overline{\rho}_f$ the fluid mass density, R the universal gas constant, ϕ the porosity, C^S and C^D the solute and dilute concentrations, respectively, and β_f and β_s the thermal expansion coefficients of fluid and solid, respectively.

To discretize the field equations (Eqs. 3.10 to 3.13), we introduce an 8-node quadrilateral element and a 20-node hexahedron element for computing the displacement, pore pressure, solute mass concentration, and temperature. Substituting the shape functions for the factors (Eqs. 3.1 to 3.4) into the field equations (Eqs. 3.10 to 3.13), and then using Galerkin's method (Finlayson, 1972, see Appendix A), the finite element formulations for displacement, pore pressure, solute mass concentration, and temperature are obtained as:

$$\mathbf{K_m}\,\tilde{\mathbf{u}} + \mathbf{A}\,\tilde{\mathbf{p}} - \mathbf{W}\tilde{\mathbf{C}} + \mathbf{V}\,\tilde{\mathbf{T}} = \mathbf{0} \quad \text{..... (3.14)}$$

$$\mathbf{A^T}\,\dot{\tilde{\mathbf{u}}} + \mathbf{S}\,\dot{\tilde{\mathbf{p}}} + \hat{\mathbf{M}}\dot{\tilde{\mathbf{C}}} + \mathbf{N}\,\dot{\tilde{\mathbf{T}}} + \mathbf{H_H}\tilde{\mathbf{p}} + \mathbf{D_H}\tilde{\mathbf{C}}^{\mathbf{S}} = \mathbf{0} \quad \text{..... (3.15)}$$

$$\mathbf{M}\dot{\tilde{\mathbf{C}}}^{\mathbf{S}} + \mathbf{D_D}\tilde{\mathbf{C}}^{\mathbf{S}} + \mathbf{Q_D}\,\tilde{\mathbf{T}} = \mathbf{f}^{\mathbf{u}} \quad \text{..... (3.16)}$$

$$\mathbf{R}\,\dot{\tilde{\mathbf{T}}} + \mathbf{U}\,\tilde{\mathbf{T}} = 0 \quad \text{..... (3.17)}$$

where

$$\mathbf{K_m} = \int_{\Omega} \mathbf{B^T D_u B}\, d\Omega \quad \text{..... (3.18)}$$

$$\mathbf{A} = \int_{\Omega} \mathbf{B^T \alpha\, m\, N_p}\, d\Omega \quad \text{..... (3.19)}$$

$$\mathbf{W} = \int_{\Omega} \mathbf{B}^{\mathbf{T}} \chi \, \mathbf{m} \, \mathbf{N}_{\mathbf{C}^s} \, d\Omega \quad \text{..... (3.20)}$$

$$\mathbf{V} = \int_{\Omega} \mathbf{B}^{\mathbf{T}} \gamma_1 \, \mathbf{m} \, \mathbf{N}_{\mathbf{T}} \, d\Omega \quad \text{..... (3.21)}$$

$$\mathbf{S} = \int_{\Omega} \mathbf{N}_{\mathbf{p}}^{\mathbf{T}} \beta \mathbf{N}_{\mathbf{p}} \, d\Omega \quad \text{..... (3.22)}$$

$$\hat{\mathbf{M}} = \int_{\Omega} \mathbf{N}_{\mathbf{p}}^{\mathbf{T}} \chi' \mathbf{N}_{\mathbf{C}^s} \, d\Omega \quad \text{..... (3.23)}$$

$$\mathbf{N} = \int_{\Omega} \mathbf{N}_{\mathbf{T}}^{\mathbf{T}} \gamma_2 \, \mathbf{N}_{\mathbf{T}} \, d\Omega \quad \text{..... (3.24)}$$

$$\mathbf{M} = \int_{\Omega} \mathbf{N}_{\mathbf{C}^s}^{\mathbf{T}} \phi \mathbf{N}_{\mathbf{C}^s} \, d\Omega \quad \text{..... (3.25)}$$

$$\mathbf{R} = \int_{\Omega} \mathbf{N}_{\mathbf{T}}^{\mathbf{T}} \mathbf{N}_{\mathbf{T}} \, d\Omega \quad \text{..... (3.26)}$$

$$\mathbf{U} = \int_{\Omega} \left\{ (\nabla \mathbf{N}_{\mathbf{T}})^T \left(c^T \right) (\nabla \mathbf{N}_{\mathbf{T}}) + (\mathbf{N}_{\mathbf{T}})^T \, \mathbf{v}_{\mathbf{f}} \, (\nabla \mathbf{N}_{\mathbf{T}}) \right\} d\Omega \quad \text{..... (3.27)}$$

$$\mathbf{H}_{\mathbf{H}} = \int_{\Omega} \left(\nabla \mathbf{N}_{\mathbf{p}} \right)^T (\mathbf{k} / \eta) \left(\nabla \mathbf{N}_{\mathbf{p}} \right) d\Omega \quad \text{..... (3.28)}$$

$$\mathbf{D}_{\mathbf{H}} = \int_{\Omega} \left(\nabla \mathbf{N}_{\mathbf{p}} \right)^T L_D \left(\nabla \mathbf{N}_{\mathbf{p}} \right) d\Omega \quad \text{..... (3.29)}$$

$$\mathbf{D}_{\mathbf{D}} = \int_{\Omega} \left(\nabla \mathbf{N}_{\mathbf{C}^s} \right)^T D^S \left(\nabla \mathbf{N}_{\mathbf{C}^s} \right) d\Omega \quad \text{..... (3.30)}$$

$$\mathbf{Q}_{\mathbf{D}} = \int_{\Omega} \left(\nabla \mathbf{N}_{\mathbf{T}} \right)^T C^S D^S \left(\nabla \mathbf{N}_{\mathbf{T}} \right) d\Omega \quad \text{..... (3.31)}$$

where the $[\mathbf{D}_{\mathbf{u}}]$ is the stiffness property for stress-strain relations, and strain displacement can be described with $[\mathbf{B}]$. (See Appendix A for full explanation of the

integrals in Eqs. 3.18 to 3.31.) For example, in the axisymmetric stress-strain problem, strain and displacement have a relation (Timoshenko and Goodier, 1982) as shown by Eq. 3.32:

$$\begin{Bmatrix} \varepsilon_r \\ \varepsilon_z \\ \gamma_{rz} \\ \varepsilon_\theta \end{Bmatrix} = \begin{bmatrix} \frac{\partial}{\partial r} & 0 \\ 0 & \frac{\partial}{\partial z} \\ \frac{\partial}{\partial z} & \frac{\partial}{\partial r} \\ \frac{1}{r} & 0 \end{bmatrix} \begin{Bmatrix} u \\ v \end{Bmatrix} \quad \text{..... (3.32)}$$

Matrix $[\mathbf{B}]$ is the expression of the spatial derivative:

$$[\mathbf{B}] = \begin{bmatrix} \frac{\partial N_1}{\partial r} & 0 & \frac{\partial N_2}{\partial r} & 0 & \frac{\partial N_3}{\partial r} & 0 & \frac{\partial N_4}{\partial r} & 0 \\ 0 & \frac{\partial N_1}{\partial z} & 0 & \frac{\partial N_2}{\partial z} & 0 & \frac{\partial N_3}{\partial z} & 0 & \frac{\partial N_4}{\partial z} \\ \frac{\partial N_1}{\partial z} & \frac{\partial N_1}{\partial r} & \frac{\partial N_2}{\partial z} & \frac{\partial N_2}{\partial r} & \frac{\partial N_3}{\partial z} & \frac{\partial N_3}{\partial r} & \frac{\partial N_4}{\partial z} & \frac{\partial N_4}{\partial r} \\ \frac{N_1}{r} & 0 & \frac{N_2}{r} & 0 & \frac{N_3}{r} & 0 & \frac{N_4}{r} & 0 \end{bmatrix} \quad \text{..... (3.33)}$$

3.1.3 Discretization in time

Among the methods to discretize the time steps for partial differential equations (Zienkiwicz and Taylor, 1989) are linear interpolations and fixed time step Δt (Smith and Griffiths, 2004). The finite element formulations derived in Section 3.1.2 include the time-dependent variables for displacement, pore pressure, solute mass concentration, and temperature. The governing equations use the second order for the spatial domain and the first order for the time domain. These domains are categorized to a parabolic partial

differential equation. A typical expression of a first-order time-dependent problem in a finite element formulation can be described by:

$$[\mathbf{K}]\{\boldsymbol{\varphi}\}+[\mathbf{m}]\left\{\frac{d\boldsymbol{\varphi}}{dt}\right\}=\{\mathbf{q}\} \quad \text{..... (3.34)}$$

Consider two consecutive time steps as follow:

$$[\mathbf{K}]\{\boldsymbol{\varphi}\}_0+[\mathbf{m}]\left\{\frac{d\boldsymbol{\varphi}}{dt}\right\}_0=\{\mathbf{q}\}_0 \quad \text{..... (3.35)}$$

$$[\mathbf{K}]\{\boldsymbol{\varphi}\}_1+[\mathbf{m}]\left\{\frac{d\boldsymbol{\varphi}}{dt}\right\}_1=\{\mathbf{q}\}_1 \quad \text{..... (3.36)}$$

where 0 and 1 indicate the previous and current time step, respectively. Then, variation of the variable φ over the two time steps can be expressed in terms of a linear interpolation between its values at the two time steps:

$$\frac{\{\boldsymbol{\varphi}\}_1-\{\boldsymbol{\varphi}\}_0}{\Delta t}\approx(1-\theta)\left\{\frac{d\boldsymbol{\varphi}}{dt}\right\}_0+\theta\left\{\frac{d\boldsymbol{\varphi}}{dt}\right\}_1 \quad \text{..... (3.37)}$$

Substituting Eq. 3.37 into Eq. 3.35 and Eq. 3.36, we obtain:

$$\{\boldsymbol{\varphi}\}_1=\{\boldsymbol{\varphi}\}_0+\Delta t\left((1-\theta)\left\{\frac{d\boldsymbol{\varphi}}{dt}\right\}_0+\theta\left\{\frac{d\boldsymbol{\varphi}}{dt}\right\}_1\right) \quad \text{..... (3.38)}$$

Using Eq. 3.35 and Eq. 3.36 and substituting them into Eq. 3.35 and Eq. 3.36, we arrive at the time discretization of finite element method:

$$\begin{aligned}([\mathbf{M}]+\theta\Delta t[\mathbf{K}])\{\boldsymbol{\varphi}\}_1 = {} & ([\mathbf{M}]-(1-\theta)\Delta t[\mathbf{K}])\{\boldsymbol{\varphi}\}_0 \\ & +\theta\Delta t\{\boldsymbol{\varphi}\}_1+(1-\theta)\Delta t\{\boldsymbol{\varphi}\}_0\end{aligned} \quad \text{..... (3.39)}$$

If θ =1/2, it is called the “Crank-Nicolson” method,

$$\left\{[\mathbf{M}]+\frac{\Delta t}{2}[\mathbf{K}]\right\}\{\boldsymbol{\varphi}\}_1=\left\{[\mathbf{M}]-\left(\frac{\Delta t}{2}\right)[\mathbf{K}]\right\}\{\boldsymbol{\varphi}\}_0 \quad \text{..... (3.40)}$$

and if θ=1, is it the "fully implicit" method, which ignores any history since the past is unknown:

$$\{[\mathbf{M}]+\Delta t[\mathbf{K}]\}\{\boldsymbol{\varphi}\}_1=[\mathbf{M}]\{\boldsymbol{\varphi}\}_0$$

The discretization for the finite element method also has incremental version that results from rearranging the governing equations (Eq. 3.14 to Eq. 3.17) for solid, fluid, solute concentration, and temperature with linear interpolation for time:

$$\begin{bmatrix} \mathbf{K_m} & \mathbf{A} & -\mathbf{W} & \mathbf{V} \\ \mathbf{A^T} & -(\mathbf{S}+\theta\Delta t\mathbf{H_H}) & -(\hat{\mathbf{M}}+\theta\Delta t\mathbf{D_H}) & -\hat{\mathbf{N}} \\ 0 & 0 & -(\mathbf{M}+\theta\Delta t\mathbf{D_D}) & -\theta\Delta t\mathbf{Q_D}) \\ 0 & 0 & 0 & -(\mathbf{R}+\theta\Delta t\mathbf{U}) \end{bmatrix} \begin{Bmatrix} \Delta\tilde{\mathbf{u}} \\ \Delta\tilde{\mathbf{p}} \\ \Delta\tilde{\mathbf{C}}^{\mathbf{S}} \\ \Delta\tilde{\mathbf{T}} \end{Bmatrix}$$
$$= \begin{Bmatrix} \Delta\mathbf{f} \\ \Delta t\mathbf{H_H}\tilde{\mathbf{p}}_{\mathbf{n-1}}+\Delta t\mathbf{D_H}\tilde{\mathbf{C}}^{\mathbf{S}}_{\mathbf{n-1}} \\ \Delta t\mathbf{D_D}\tilde{\mathbf{C}}^{\mathbf{S}}_{\mathbf{n-1}}+\Delta t\mathbf{Q_D}\tilde{\mathbf{T}}_{\mathbf{n-1}} \\ \Delta t\mathbf{U}\tilde{\mathbf{T}}_{\mathbf{n-1}} \end{Bmatrix} \quad \text{..... (3.41)}$$

The difference between these two methods is that absolute discretization obtains total values for displacement, pore pressure, solute mass concentration, and temperature, whereas incremental discretization computes the relative values. For example, if we have a constant pore pressure boundary condition at the wellbore, the corresponding traction and the values for pore pressure at the wellbore should be applied in each time step for the absolute version; but for the incremental version, we apply the traction and pore pressure values only for the first time step since there is no relative change with a constant boundary condition.

3.1.4 Boundary conditions

It is important to define the boundary conditions in geomechanics simulations; for example, hydraulic injection pressure p, injection rate Q, injection temperature T, mud solute concentration C^S are often used in geothermal and petroleum reservoir study. For the finite element formulation (Eq. 3.41), explicit variables such as displacement pore pressure, solute concentration, and temperature can define the boundary by the penalty method. This method operates by multiplying the corresponding prescribed boundary values on the left-hand side of the matrix and its corresponding coefficient on the right-hand side vector by a large value (Fig. 3.4). This in effect fixes the known value (boundary condition) on the nodes; that is, it prescribes the value we desired for the unknown variables.

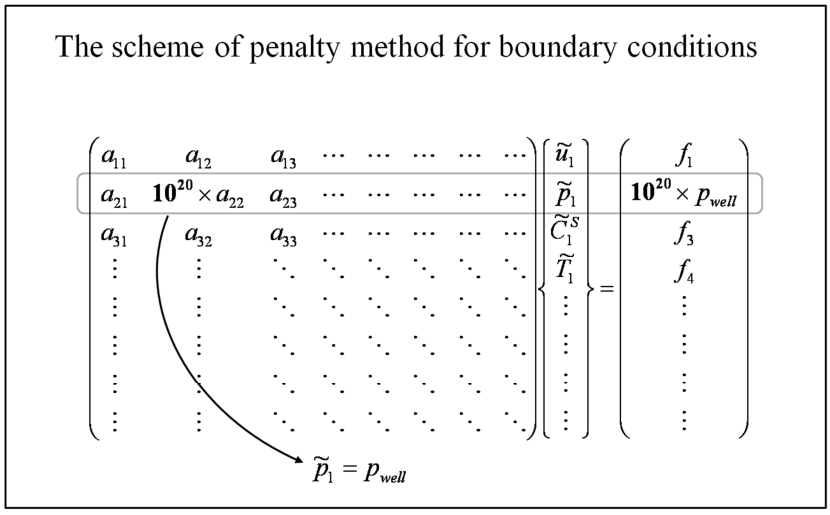

Fig. 3.4. Illustration of the penalty method in the finite element formulation for the boundary conditions of displacement, pore pressure, solute concentration, and temperature.

The other most-used boundary condition in geomechanics simulations is the injection rate boundary condition. Consider the finite element formulation for the fluid mass-balance equation (Eq. 3.11). The right-hand side matrix should be defined by injection rate *Q* at the boundary elements as,

$$\alpha(\nabla\cdot\dot{\mathbf{u}})+\beta\dot{p}+\chi'\dot{C}^S+\gamma_2\dot{T}-\frac{k}{\mu}\nabla^2 p+\frac{k}{\mu}L_D\nabla^2C^2=f_q \quad \text{..... (3.42)}$$

where

$$f_q=\sum_{i=1}^{nip}(N_iQ)d\Omega$$

where *nip* is the number of Gaussian points and N_i denotes the shape function.

A typical example of implementation of injection rate boundary conditions for the finite element method is illustrated in Fig. 3.5. The difference between the injection boundary condition and the pressure boundary condition is that the pore pressure distribution is computed through the finite element for the given *Q*.

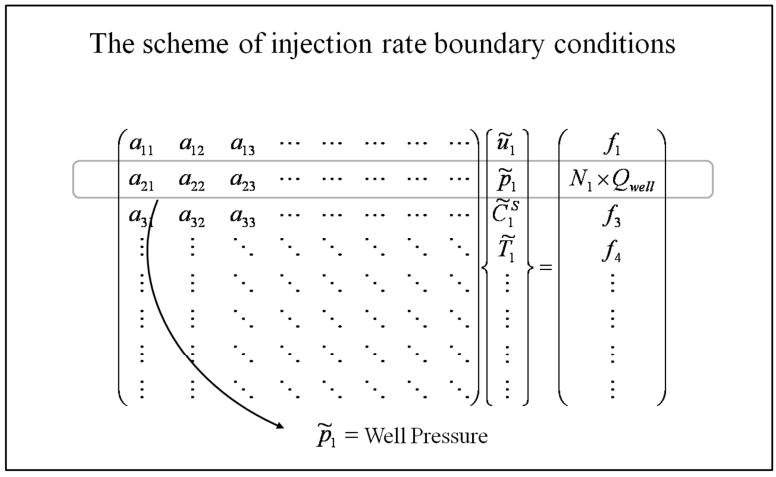

Fig. 3.5. Illustration of injection rate boundary conditions in the finite element method.

Another important boundary condition in coupled fluid flow and solid problems is mechanical loading. For describing the prescribed traction that results, for example, from pressurizing the wellbore, tractions must relate the acting wellbore with the far-field stress of the system. For example, if the pore pressure on the wall of the wellbore is 20 MPa and the far-field stress is 10 MPa, the applied traction is 20 MPa – 10 MPa = 10 MPa at the wellbore, which takes into account the relative force between the well pressure and natural in-situ stress. The mechanical loading term at the boundary for the solid in finite element formulations as is described by:

$$\mathbf{K_m}\,\tilde{\mathbf{u}} + \mathbf{A}\,\tilde{\mathbf{p}} - \mathbf{W}\tilde{\mathbf{C}} + \mathbf{V}\,\tilde{\mathbf{T}} = \mathbf{f} \quad \text{..... (3.43)}$$

where:

$$f = \sum_{i=1}^{nip} \left(N_i\, f\right) d\Omega$$

The right-hand side of Eq. 3.43 is the mechanical load (traction on the boundary). Fig. 3.6 shows the matrix configuration for the mechanical loading at the boundary. For the poroelastic simulation without rock failure, it is not necessary to iterate to solve the variables. However, an iteration scheme should be introduced if we consider the rock failure and stress-dependent permeability since the results of stress and permeability conditions with certain loading are satisfied during the iterations. An illustration of the iteration procedure for the case of rock failure and permeability variations is presented in Section 4.

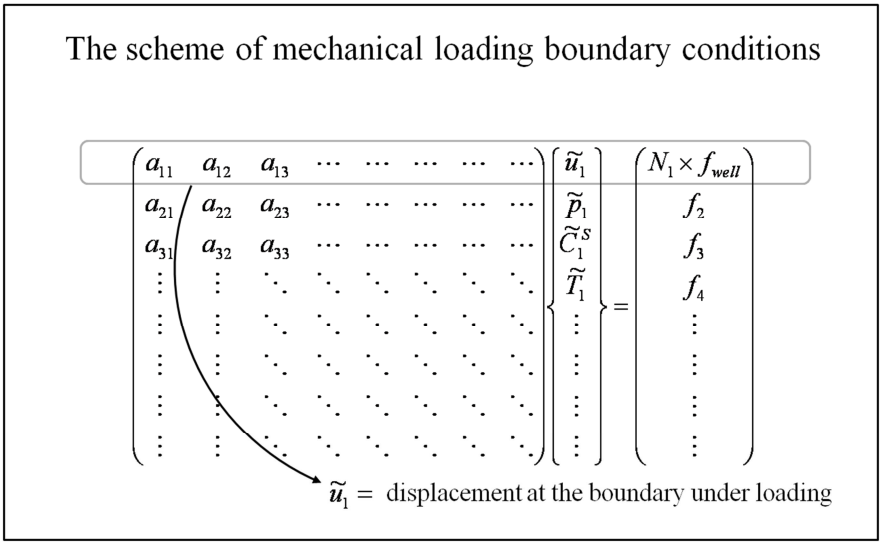

Fig. 3.6. Illustration of mechanical loading boundary condition in the finite element method.

3.2 Verifications of the finite element method

In this section, finite element results for coupled problems are compared with analytical solutions. The reservoir conditions such as far-field stress, injection pressure, temperature, and initial pore pressure are critical in geomechanical simulations; therefore it is necessary to validate the numerical modeling under various boundary conditions. We verified two-dimensional and three-dimensional finite element modeling using the analytical solutions for a wellbore in an poroelastic, thermo-poroelastic, and thermo-chemo-poroelastic formation. For the poroelastic case, Mode 1, Mode 2, and Mode 3 were considered (Detournay and Cheng (1988). The verifications of thermal and chemical loading were made possible by using the solution by McTigue (1986) and Ghassemi et al. (2009), respectively.

For better understanding of the wellbore response, the wellbore loading can be decomposed into three parts (Carter and Booker, 1982; Detournay and Cheng, 1988). We used three modes for decomposition of the poroelastic problem around a wellbore: Mode I is an isotropic stress loading of the wellbore; Mode II is the pore pressure loading or injection into the wellbore; and Mode III is the loading of the wellbore by a far-field deviatoric stress (deviatoric far-field). The complete solution is the sum of the solutions to the three modes. The verifications were performed with mesh consisting of 350 elements and 1141 nodes which have 8 quadrilateral nodes for displacements and 4 nodes for pore pressure, temperature, and solute concentration (Fig. 3.7). The maximum and minimum far-field stress components were applied to the x- and y-directions, respectively, and reservoir properties are described in Table 3.1.

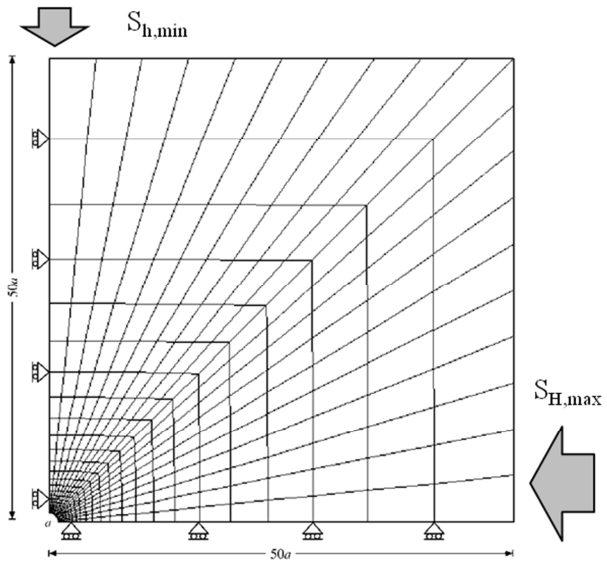

Fig. 3.7. Mesh used for the verifications, consisting of 350 elements and 1141 nodes.

Table 3.1
Rock properties of shale.

Young's modulus E (GPa)	1.85
Drained Possoin's ratio υ	0.219
Undrained Possoin's ratio υ_u	0.461
Skempton's coefficient, B	0.915
Permeability, k (md)	1×10^{-10}
Porosity, ϕ	0.299
Fluid mass density, ρ_f (kg/m^3)	1000
Fluid viscosity, μ (Pa·s)	0.3×10^{-3}

3.2.1 Isotropic far-field stress around a wellbore (Mode I)

Mode I represents the isotropic far-field stress distribution around a wellbore assuming no initial pore pressure; hence, Mode I results are the same as those for linear elasticity. We applied 10 MPa for isotropic far-field stress and compared finite element results with the analytical solution with a radius (Fig. 3.8; solid lines represent analytical solutions and numerical solutions are plotted as dotted symbols). The radial and tangential stresses are equally distributed around a wellbore by the isotropic far-field stress.

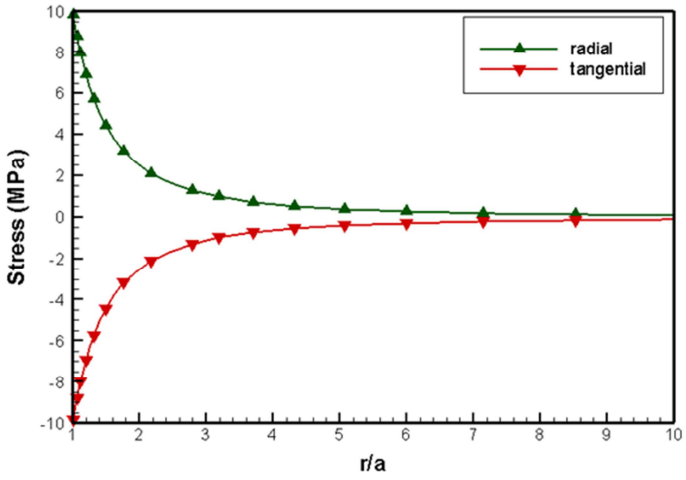

Fig. 3.8. Distributions of radial and tangential stress around a wellbore by isotropic far-field stress (Mode I). Finite element results are compared with the analytical solutions.

3.2.2 The influence of fluid flow around a wellbore (Mode II)

Initial reservoir pore pressure is maintained in equilibrium before we begin any exploration such as geothermal heat extraction, well stimulation, and oil and gas production. Once the change of pore pressure distribution occurs by fluid injection or production, fluid-induced stress variations should be considered. In this part, both production and injection-induced stress variations are presented.

In one example for stress variation induced by fluid production, we set boundary conditions so that the initial pore pressure was 10 MPa and wellbore pressure 0 MPa. Far-field stresses were assumed to be zero to study the induced stress variations. The comparison of finite element results and analytical solutions for pore pressure and total

radial and tangential stresses are presented in Fig. 3.9 to Fig. 3.11 Note that fluid extraction causes significant changes of tangential stresses with time around a wellbore.

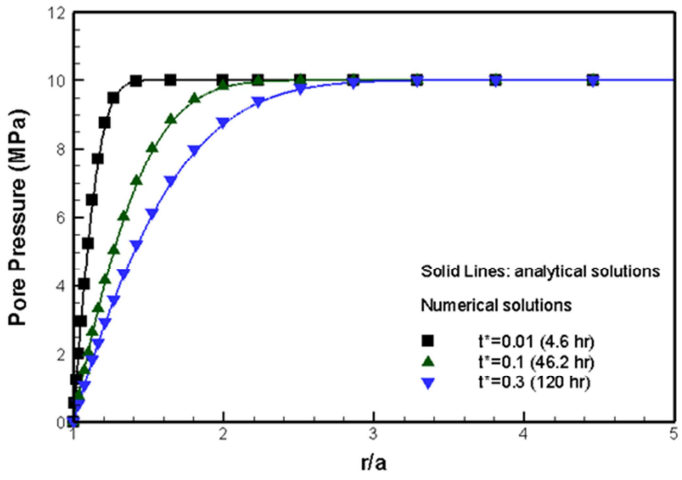

Fig. 3.9. Pore pressure distribution with respect to time when the pressure is zero at the wellbore (Mode II). Finite element results are compared with the analytical solutions.

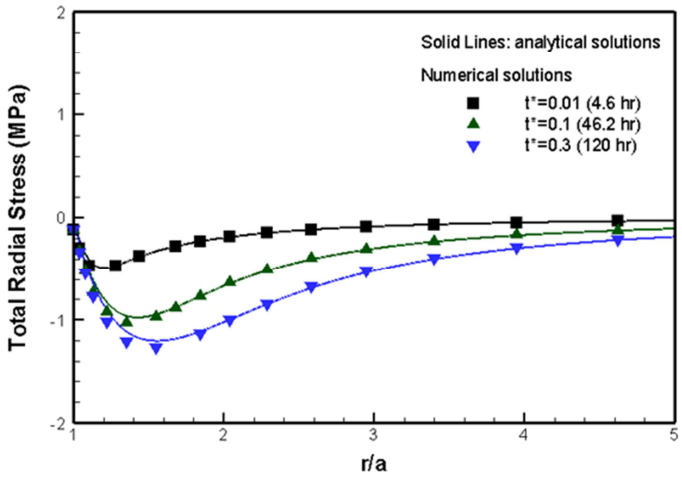

Fig. 3.10. The distribution of total radial stress with respect to time under production (Mode II). Finite element results are compared with analytical solutions.

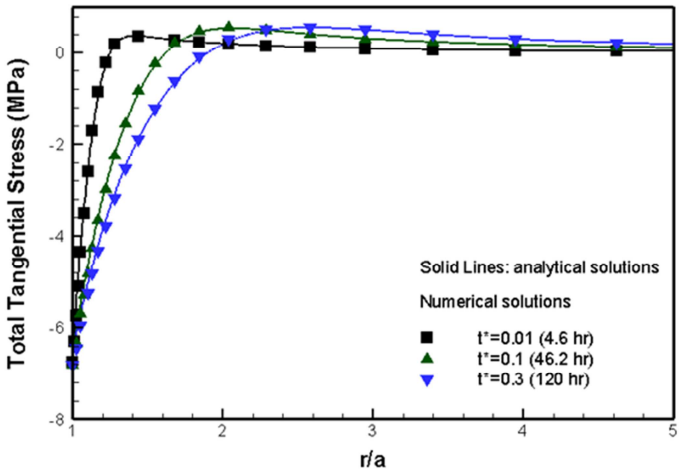

Fig. 3.11. Total tangential stress distribution with respect to time under production (Mode II). Finite element results are compared with the analytical solutions.

The other induced stress we are interested in is the injection case. The simplest condition for the injection sets pore pressure at the wall at 10 MPa, with no initial pore pressure and no far-field stresses. Results for numerical and analytical solutions are plotted in Fig. 3.12 to 3.14 for pore pressure and total radial and tangential stress distributions. In this case, the tangential stress distributions are significantly changed around a wellbore by fluid injection.

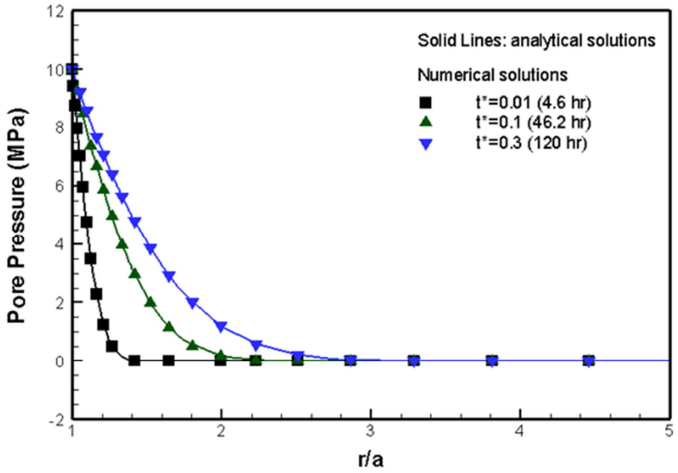

Fig. 3.12. Pore pressure distribution with respect to time when the pressure is 10 MPa at the wellbore (Mode II). Finite element results are compared with the analytical solutions.

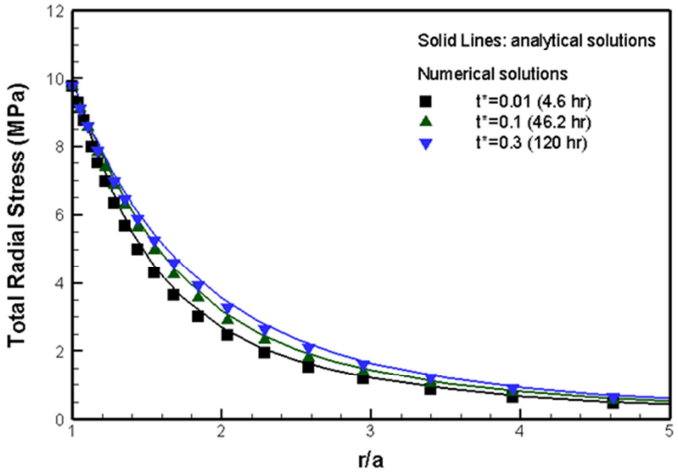

Fig. 3.13. The distribution of total radial stress with respect to time when the well is pressurized to 10 MPa (Mode II). Finite element results are compared with the analytical solutions.

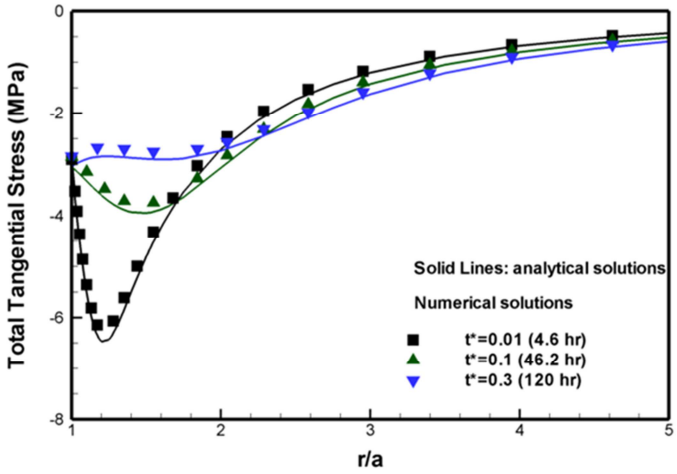

Fig. 3.14. Total tangential stress distribution with respect to time under pressurization (Mode II). Finite element results are compared with the analytical solutions.

3.2.3 The influence of deviatoric far-field stress (Mode III)

Deviatoric far-field stress plays an important role in stress distribution around a wellbore. It impacts tensile stress to the maximum far-field stress direction and compressive stress to the minimum far-field stress direction around a wellbore. This localized stresses often leads to shear and tensile failures around a wellbore. The boundary conditions on the well follow (Carter and Booker, 1982; Detrournay and Cheng, 1988):

$$\sigma_{rr} = -S_0 \cos 2\theta \quad \text{..... (3.44)}$$

$$\sigma_{r\theta} = S_0 \sin 2\theta \quad \text{..... (3.45)}$$

$$p = 0 \quad \text{..... (3.46)}$$

where S_0 denotes the deviatoric components in far-field stress and θ is the horizontal rotational angle along to the wellbore.

The influence of deviatoric stress is apparent where the deviatoric far-field stress is 10 MPa in the x-direction and -10 MPa in the y-direction. To clarify the influence of deviatoric stress effects, we assumed no initial pore pressure and no isotropic far-field stress. The distributions for pore pressure with time are presented in Fig. 3.15 and Fig. 3.16. The negative pore pressure distributions are localized to the maximum far-field stress direction and the positive pore pressure distributions to the minimum far-field stress direction, since the effects are coupled around a wellbore. From the physical point of view, tensile stress increases the pore volume, whereas compressive stress plays to decrease the pore volume. The finite element results for total radial and tangential stress distributions are compared with analytical solutions for both maximum and minimum far-field stress directions in Fig. 3.17 to Fig. 3.20. The influence of deviatoric stress on the fluid variations derived analytically by Detournay and Cheng (1988) are compared with finite element results in Fig. 3.21.

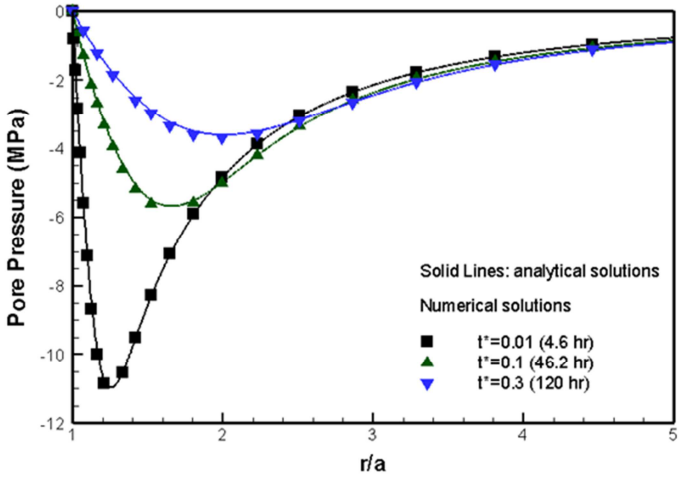

Fig. 3.15. Pore pressure distribution with respect to time along the maximum far-field stress direction when the deviatoric far-field (10 MPa) stress is applied (Mode III). Finite element results are compared with analytical solutions.

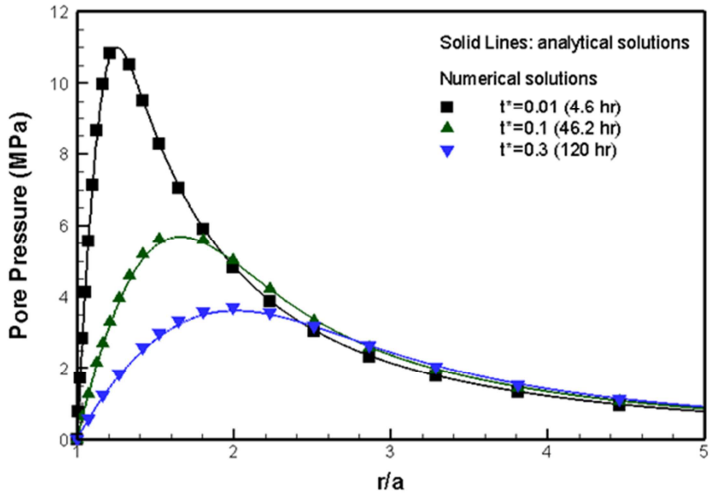

Fig. 3.16. Pore pressure distribution with respect to time along the minimum far-field stress direction when the deviatoric far-field (10 MPa) stress is applied (Mode II). Finite element results are compared with analytical solutions.

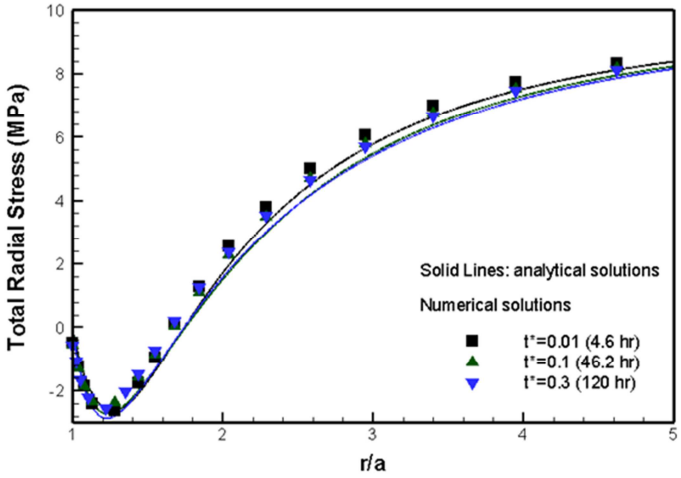

Fig. 3.17. The distribution of total radial stress along the maximum far-field stress direction when the deviatoric far-field (10 MPa) stress is applied (Mode III). Finite element results are compared with analytical solutions.

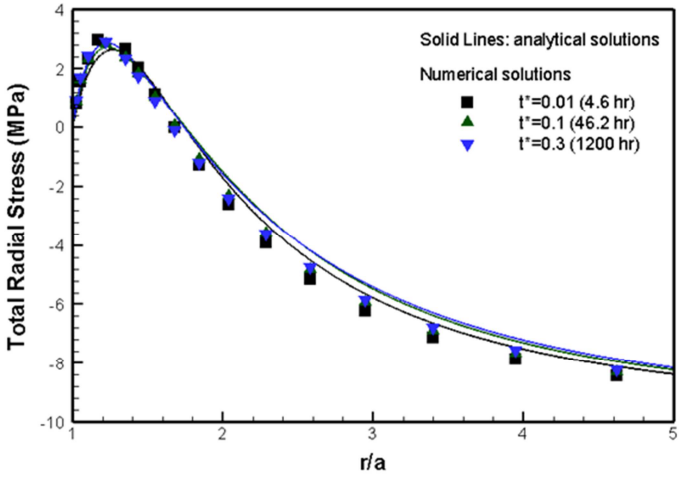

Fig. 3.18. The distribution of total radial stress along the minimum far-field stress direction when the deviatoric far-field (10 MPa) stress is applied (Mode III). Finite element results are compared with analytical solutions.

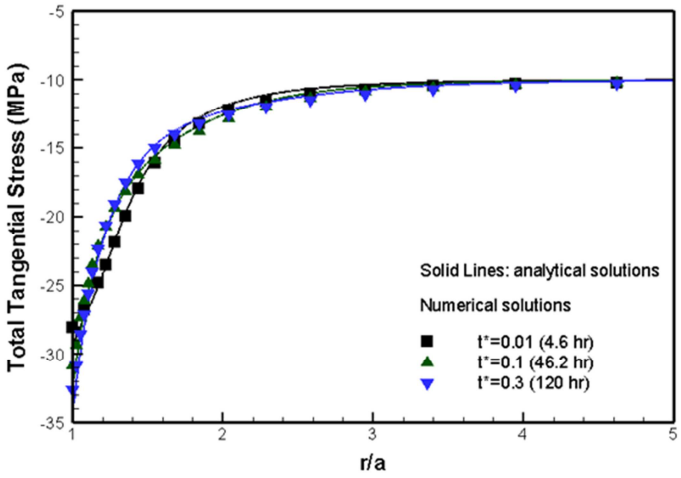

Fig. 3.19. The distribution of total tangential stress along the maximum far-field stress direction when the deviatoric far-field (10 MPa) stress is applied (Mode III). Finite element results are compared with analytical solutions.

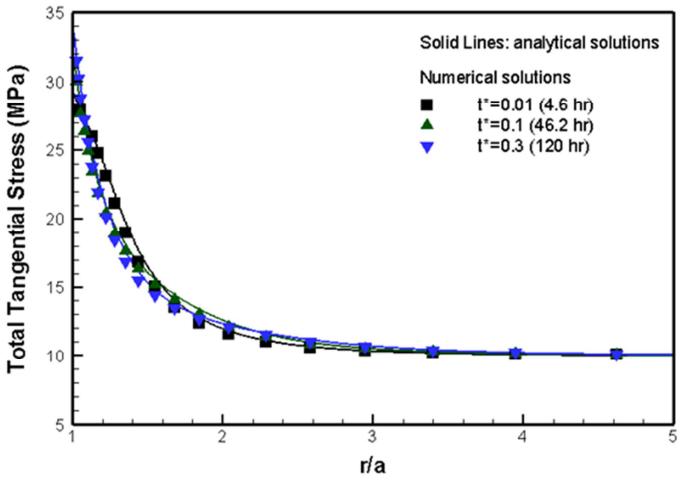

Fig. 3.20. The distribution of total tangential stress along the minimum far-field stress direction when the deviatoric far-field (10 MPa) stress is applied (Mode III). Finite element results are compared with analytical solutions.

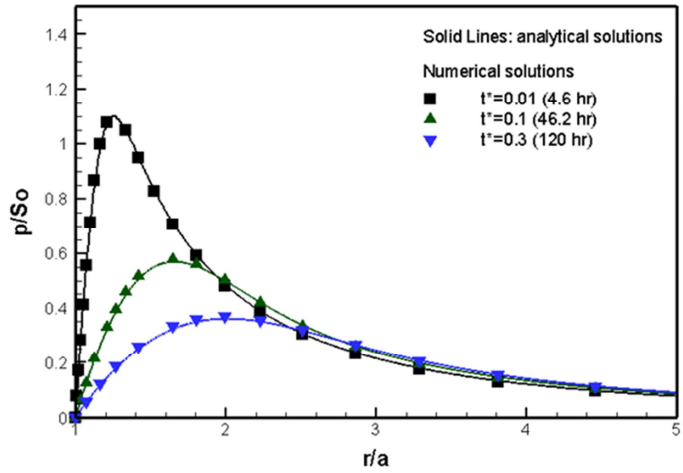

Fig. 3.21. Comparison of the finite element results with analytical solutions for the pore pressure variations with radius.

3.2.4 Combined influence (Mode I + Mode II + Mode III)

We considered the combined influence of isotropic far-field stress, deviatoric far-field stress, and fluid injection and production around a wellbore. Boundary conditions considering all factors are as follows:

$$\sigma_{rr} = P_0 - S_0 \cos 2\theta \quad \text{..... (3.47)}$$

$$\sigma_{r\theta} = S_0 \sin 2\theta \quad \text{..... (3.48)}$$

$$p = p_0 \quad \text{..... (3.49)}$$

where P_0 denotes the isotropic far-field stress and p_0 is injection well pressure.

The given boundary conditions for the verifications are isotropic far-field stress 20 MPa, deviatoric far-field stress 5 MPa, and injection well pressure 10 MPa. The comparisons for pore pressure distributions are plotted in Fig. 3.22 (to the maximum far-

field stress direction), and in Fig. 3.23 (to the minimum far-field stress direction). Total tangential stress distributions are also compared to the maximum and minimum far-field stress direction in Fig. 3.24 and Fig. 3.25.

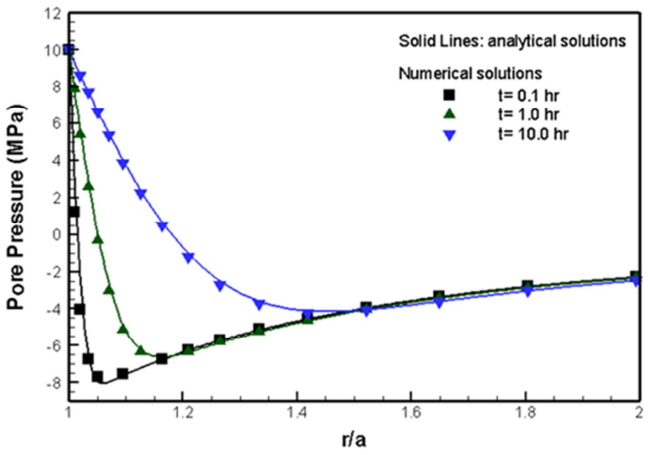

Fig. 3.22. Pore pressure distributions to the maximum far-field stress direction around a wellbore for an injection case under anisotropic far-field pressures. Finite element results are compared with analytical solutions.

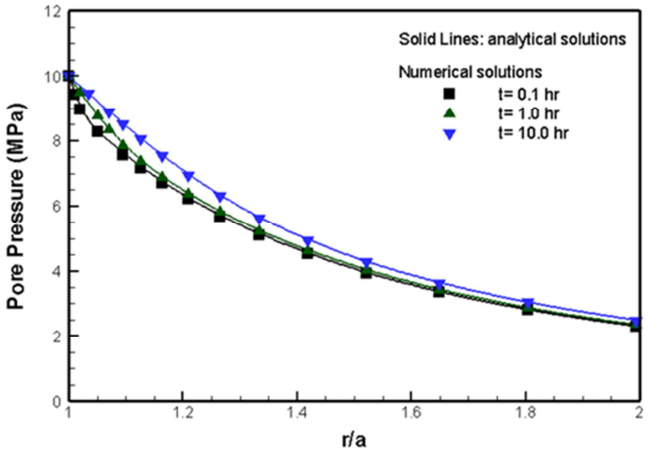

Fig. 3.23. Pore pressure distributions to the minimum far-field stress direction around a wellbore for injection case under anisotropic far-field. Finite element results are compared with the analytical solutions.

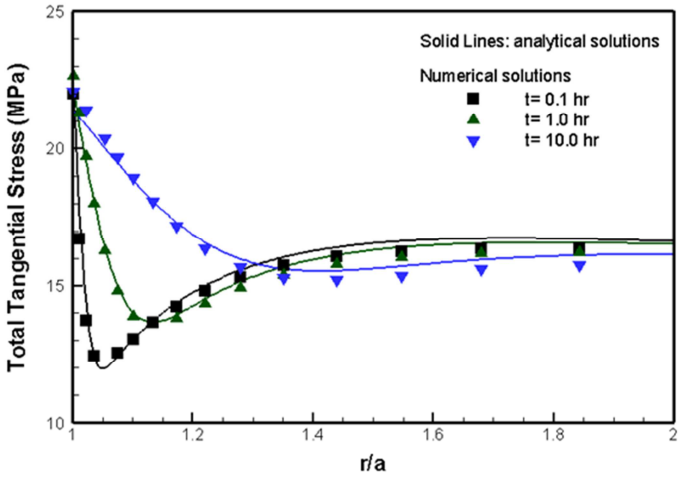

Fig. 3.24. Total tangential stress distributions to the maximum far-field stress direction around a wellbore for injection case under anisotropic far-field pressure. Finite element results are compared with the analytical solutions.

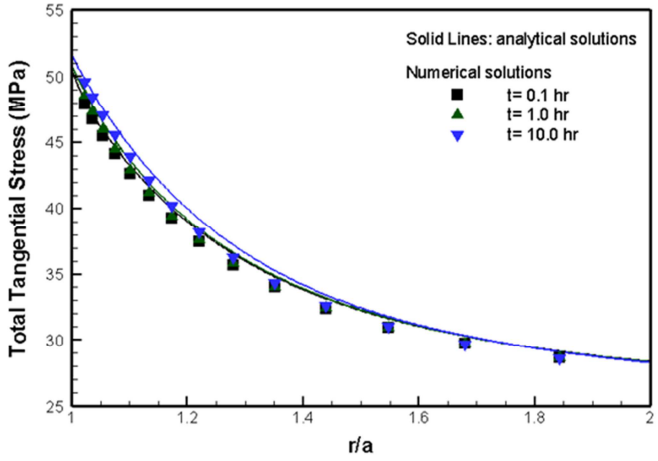

Fig. 3.25. Total tangential stress distributions to the minimum far-field stress direction around a wellbore for injection under the anisotropic far-field case. Finite element results are compared with analytical solutions.

3.2.5 Temperature and solute transport

The analytical solution for the impact of thermal loading has been developed by McTigue (1986), Kurashige (1989), Li et al. (1998), and Wang and Papamichos (1994). They found that the difference of thermal expansion coefficients between the rock and fluid flow cause the thermal stress to the rock in turn to impact the pore pressure distributions. Cold water injection to the hot reservoir causes rock shrinkage, and result in contributions to the tensile stress around the injection wellbore. The finite element results are compared with analytical solutions in Fig. 3.26 and Fig. 3.27. Initial reservoir temperature of 115°C and injection pressure of 65°C are applied in this comparison. Note that thermally-induced tensile stress leads the negative pore pressure distribution around a wellbore as described earlier in 3.2.3.

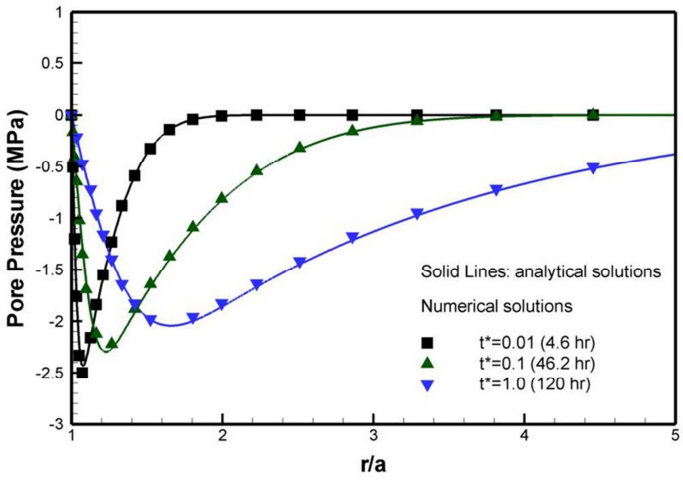

Fig. 3.26. Comparison of the pore pressure caused by temperature loading using variation with radial distance.

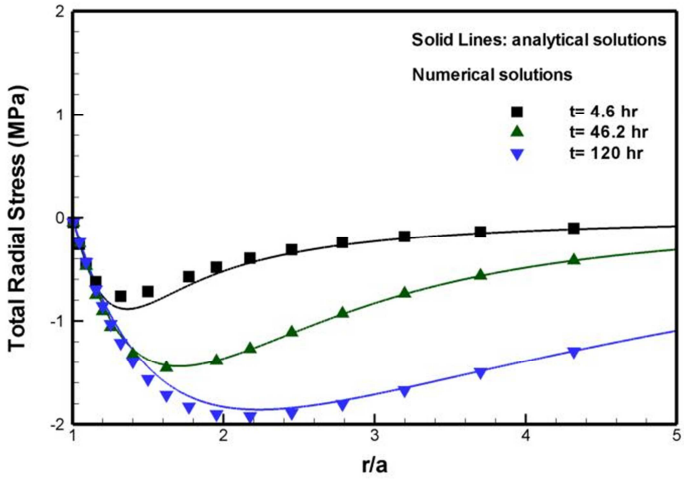

Fig. 3.27. Comparison of the total radial stress variations caused by temperature loading.

Sherwood and Baily (1994) proposed a constitutive model in the membrane system, assuming no solute transport consideration, and Heidug and Wong (1996) developed a fully coupled ion transport model. To accommodate the nonlinear relations between stress and solute concentration, Ghassemi and Diek (2003) proposed a linear chemo-thermo-poroelasticity model, and it has been shown both analytically and numerically that the resulting errors are negligible when the difference of solute concentration between the mud and the shale formation is not severe (Zhou and Ghassemi, 2009). Initial reservoir solute concentration is assumed to be 0.2 and mud concentration is 0.1 for the comparison. The pore pressure distributions and total tangential stress distributions during chemical loading are presented in Fig. 3.28 and Fig. 3.29. Results show that osmosis flow from the mud to the shale formation causes the increase of pore pressure around a wellbore (Fig. 3.28). The stress distributions are significantly affected by chemical loading (Fig. 3.29).

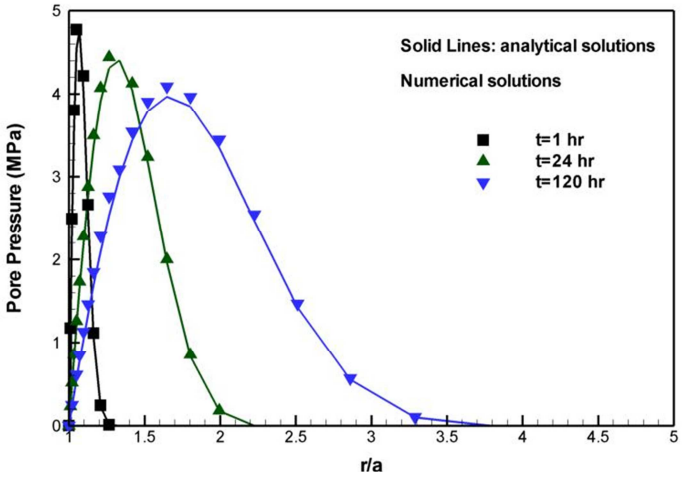

Fig. 3.28. Comparison of the pore pressure variations with radius caused by chemical loading, using numerical and analytical methods.

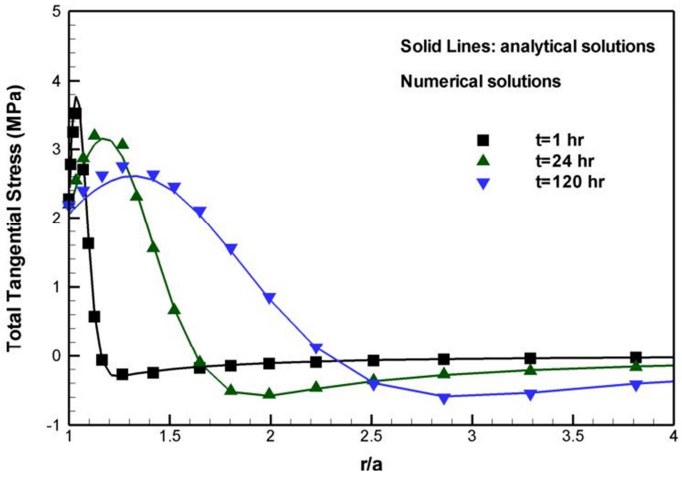

Fig. 3.29. Comparison of the total tangential stress variations with radius caused by chemical loading using numerical and analytical methods.

4. IMPLEMENTATION OF DAMAGE MECHANICS AND STRESS-DEPENDENT PERMEABILITY

The previous section presented the numerical procedure for partial differential equations—especially for solving the displacement, pore pressure, solute concentration, and temperature problems—and also compared the finite element results with analytical solutions for various engineering problems such as hydraulic pressure under anisotropic far-field stress, the influence of thermal stress, and chemical loading around a wellbore.

A coupled chemo-thermo-poroelasticity is critical to understand the interaction of pore pressure, temperature, and chemical potential in rock deformation. However, the theory has limitations in that it assumes an elastic rock skeleton and constant permeability. It is often used to consider the nonlinear behavior of rock in field operations such as sanding management, fracturing jobs, and drilling operations in unconsolidated reservoirs. Experimental core analysis for the strain-stress behavior of the rock in compressive loading shows the four stages of stress which are elastic, hardening, softening, and critical stress state (residual strength). Damage mechanics can describe the nonlinear behavior of rock under loading by considering the micro-crack, microvoid, and crackgrowth stresses (Kachanov, 1986; Lemaitre and Chaboche, 1990; Voyiadjis and Kattan, 1999). Kachanov (1986) proposed an effective configuration of undamaged material from the nominal state by introducing the damage variable, d .

Several researchers have shown that permeability is a stress-dependent property (Chin, 2000; Thomas et al., 2003; Bai and Elsworth, 1994; Tang et al., 2002). Tang et al.

(2002) tested permeability variations under triaxial loading and indicated that permeability decays exponentially before the rock failure in compressive stress and it increases suddenly by a factor of 2 to 3 after the rock failure. Similar results have been reported by other researchers (Shipping et al., 1994; Kiyama et al. 1996; Coste et al., 2001; Zoback and Byerlee, 1975), with the increase in permeability depending on rock type and conditions (De Paola et al., 2009; Wang and Park, 2002). Zoback and Byerlee (1975) illustrated the relation between the permeability change and microcrack and void evolution.

In this section, we present a numerical approach for implementing damage theory and stress-dependent permeability models into a fully coupled thermo-hydro-mechanics model. Triaxial simulations with finite element methods have been carried out to find the material parameters which define the peak stress and residual strength. In addition, a stress-dependent permeability model has been applied to both elastic and inelastic rock states, and then we present the influence of localized rock damage and permeability change caused by fluid injection around a wellbore.

4.1 Damage model

A damage and stress-dependent permeability model was proposed by Tang et al. (2002) from experiments for porous rock that measured the permeability and modulus change with respect to the change of strain (Yang et al., 2004). This model assumes that the strain-stress behavior before the rock failure follows the elasticity model without the hardening process and reaches the residual strength regime. From this damage model,

there is no damage in the elastic phase, but the rock begins to fail by crack initiation and void growth when the stress conditions reach the failure state; that is, it satisfies the failure criterion. This model has an advantage for describing the behavior of brittle rock, which has a short range of hardening and directly reaches the softening regime in triaxial tests. An elastic-damage mechanics model represents the rock degradation by expressing the damage in terms of a reduction in the elastic modulus as the damage proceeds:

$$E = (1-d)E_0 \ , \quad \text{.....} \quad (4.1)$$

where d is the damage variable which describes the amount of degradation (crack initiation, microvoid growth, and crack propagation) and E and E_0 are altered modulus and initial modulus, respectively. The degree of damage level can be represented with damage variable from 0 to 1 with a relationship of strain variations. For example, d = 0 if the rock is in elastic phase, and d = 1 if the rock is perfectly damaged. The damage model from the rock failure can be considered as either of two types, compressive and tensile stresses.

In compressive rock failure, the damage variable for describing softening and the critical state can be described as:

$$d = 1-\left\{\left(\frac{f_{cr}-f_c}{\varepsilon_{cr}-\varepsilon_c}\right)(\bar{\varepsilon}-\varepsilon_c)+f_c\right\}\Big/E_0\,\bar{\varepsilon} \quad (\varepsilon_c < \bar{\varepsilon} < \varepsilon_{cr})$$
$$d = 1-\frac{f_{cr}}{E_0\bar{\varepsilon}} \quad \text{.....} \quad (4.2)$$

where f_{cr} is the residual compressive strength and f_c is the maximum compressive stress. ε_{cr} and ε_c are the residual compressive strain and maximum compressive strain, respectively, and $\bar{\varepsilon}$ is the equivalent strain (Mazars, 1986):

$$\bar{\varepsilon} = \sqrt{\sum \langle \varepsilon \rangle_+^2} \quad \text{..... (4.3)}$$

where $\langle \varepsilon \rangle_+ = \varepsilon_i$ if $\varepsilon_i \le 0$ (tensile) and $\langle \varepsilon \rangle_+ = 0$ if $\varepsilon_i > 0$ (compressive).

This equivalent strain definition from Mazars (1986) represents a damage evolution that is dominated by tensile strain. These components of strain during damage evolution can be obtained as follows:

$$\sigma = \langle \sigma \rangle_t + \langle \sigma \rangle_c \quad \text{..... (4.4)}$$

where $\langle \sigma \rangle_t$ is built with the tensile components of the principal stress and $\langle \sigma \rangle_c$ is for compressive components of principal stress. In this way, we can obtain strain components for tensile and compressive stresses:

$$\varepsilon_t = \frac{1+\nu}{E_0(1-d)} \langle \sigma \rangle_t - \frac{\nu}{E_0(1-d)} tr\left(\langle \sigma \rangle_t \right) \quad \text{..... (4.5)}$$

$$\varepsilon_c = \frac{1+\nu}{E_0(1-d)} \langle \sigma \rangle_c - \frac{\nu}{E_0(1-d)} tr\left(\langle \sigma \rangle_c \right) \quad \text{..... (4.6)}$$

$$\sigma = \langle \sigma \rangle_t + \langle \sigma \rangle_c \quad \text{..... (4.7)}$$

If damage occurs in a tensile stress field, the damage variable is defined using the residual tensile strength of rock as:

$$d = 1 - \frac{f_{tr}}{E_0 \bar{\varepsilon}} \quad \text{..... (4.8)}$$

To trace the progress of damage under tensile stress, we introduced a tension cut-off, T_0, for tensile failure because the Mohr-Coulomb failure criterion was developed based on shear failure and it often overestimates the stress state for rock failure. The Mohr-Coulomb failure criterion for shear failure can be described as

$$F = \frac{\sigma_1 + \sigma_3}{2}\sin\phi_f - \frac{\sigma_1 - \sigma_3}{2} - c_F \cos\phi_f \quad \text{.....} \quad (4.9)$$

where σ_1 and σ_3 are the maximum and minimum principal stresses, respectively; ϕ_f and c_f represent the friction angle and cohesive strength, respectively.

4.2 Numerical implementation of the damage model

The theory of damage mechanics has been implemented into the finite element code described above. For illustration purposes, we consider the numerical simulation of the stress-strain response of a rock obtained from a laboratory triaxial experiment. In particular, we simulated the experimental data of Wang and Park (2002) and Tang et al. (2002), which shows a rapid decrease from the peak stress. The simulation domain for the axisymmetric triaxial test is shown in Fig. 4.1. The sample size is 1 cm×2 cm, which has axisymmetry so its actual ratio is 1:2. An axial load is applied in the z-directional in a step-wise manner by increasing the displacement of the top of the sample. Displacement step change in this simulation is 2×10^{-3}m per each step, and the total step number is 80. The procedure for implementation of damage mechanics and the stress-dependent permeability model is illustrated in Fig. 4.2. The state of stress is checked in each element by fluid and thermal loading. Once the stress condition is to be satisfied

with the failure criterion, the damage variable for the element is computed using previously described damage equations (Eq. 4.2 to 4.8). It is important to consider the change of the poroelastic parameters such as bulk modulus, Biot's constant, and porosity. The change of porosity, ϕ, is equal to the damage variable, d (Shao, 2002), and other modulus-related parameters are also updated with the relation of $E = (1-d)E_0$. To obtain accurate numerical results, the convergence of damage variables under a certain loading is critical before moving to the next time step. For example, damage variables in each element in the first and second iterations are compared, and if the result does not satisfy the criterion, damage variables are updated with the same loading conditions. The tolerance criterion in this simulation is 0.1 %.

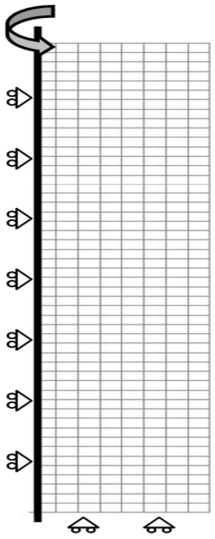

Fig. 4.1. Finite element mesh used for triaxial simulations.

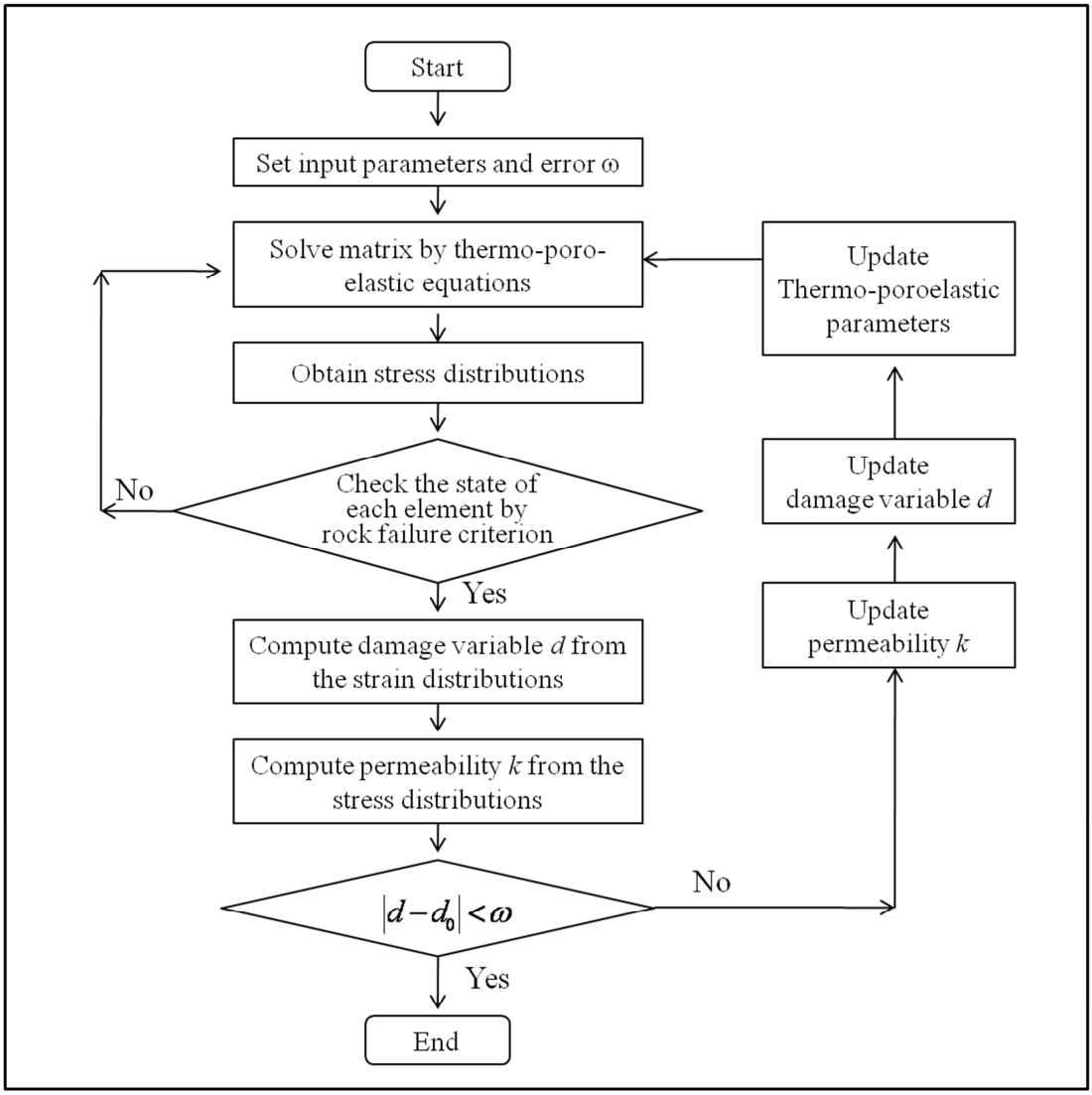

Fig. 4.2. Flow chart of the simulation procedures for the implementation of the damage and permeability model in thermo-poroelasticity with rock failure.

Simulated results in Fig. 4.3 show the peak stress variations by defining cohesive strength c_f and the residual strength change by defining f_{cr} in the damage model. Fig. 4.4 shows the simulated and actual curves for different pairs of c_f and f_{cr}. The best fits with experimental data are selected so that the residual strength, f_{cr}, in Eq. 4.4 and the

cohesive strength, c_f, in the Mohr-Coulmb failure criterion are determined. The implementation of the damage model for the tensile failure case is illustrated in Fig. 4.5.

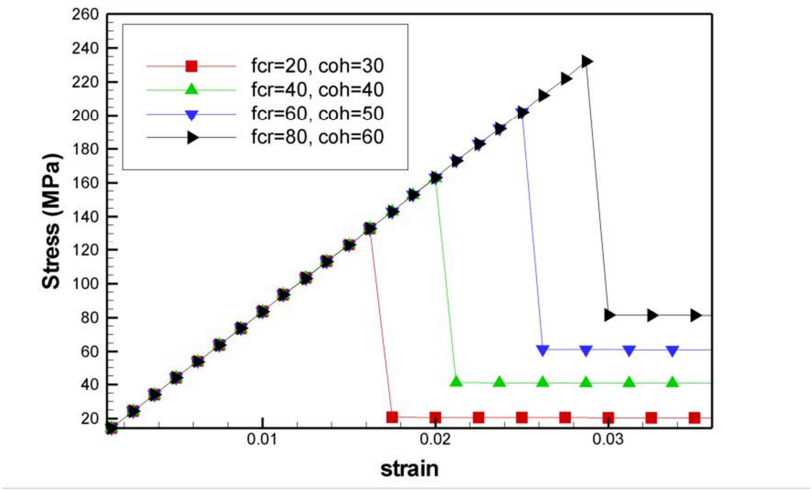

Fig. 4.3. Strain-stress curve variations with cohesive strength c_f and critical residual stress f_{cr}.

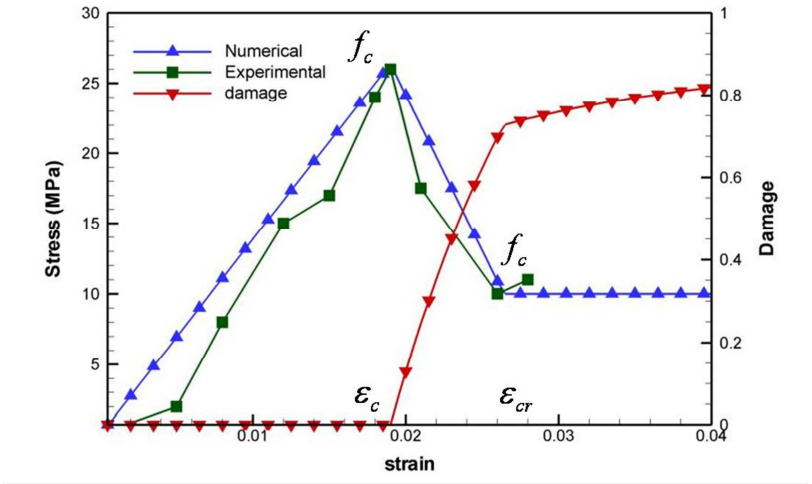

Fig. 4.4. Comparison of numerical implementation of the damage model and the experimental triaxial test. Triaxial test results are obtained from Tang et al. (2002).

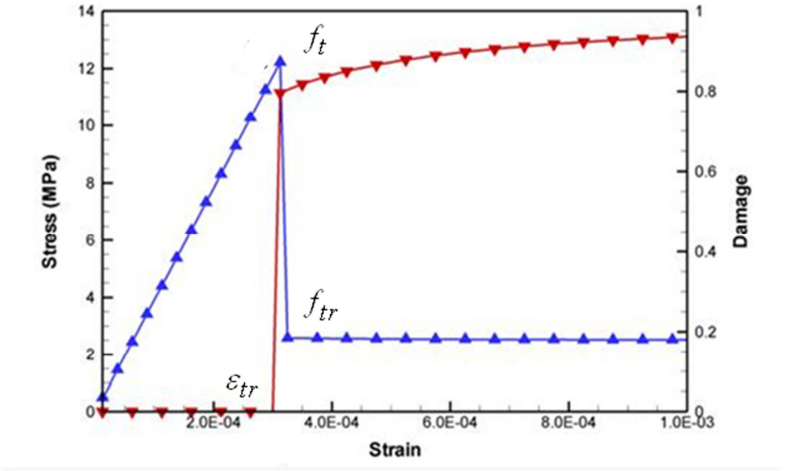

Fig. 4.5. Numerical implementation damage theory for the tensile failure case.

To simulate a more realistic triaxial test, we considered the heterogeneity of the modulus using the Weibull distribution function, which is widely used in a geomechanics simulation to depict the heterogeneity of rock. The heterogeneity of the modulus is introduced to the Gaussian points in each element. The Weibull distribution functions are defined as,

$$\varphi = \frac{n}{s_0}\left(\frac{s}{s_0}\right)^{n-1} \exp\left[-\left(\frac{s}{s_0}\right)^{n}\right] \quad \text{..... (4.10)}$$

where s is the variables s_0 represents the corresponding mean value.

The parameter n is the control factor in Weibull distribution function. A large n indicates the distributions are narrow and more homogeneous, whereas lower n represents the more heterogeneous rock. This index influences the rock failure in triaxial tests so that average peak stresses are reduced if the rock is more heterogeneous because of the increase of the lower modulus in the distributions. The heterogeneous results are

presented in Fig 4.6. Results show a reduction of peak stress and smooth variations in the heterogeneity case, which increase compared to homogeneous case. This is because of the earlier beginning of rock failure in low modulus elements.

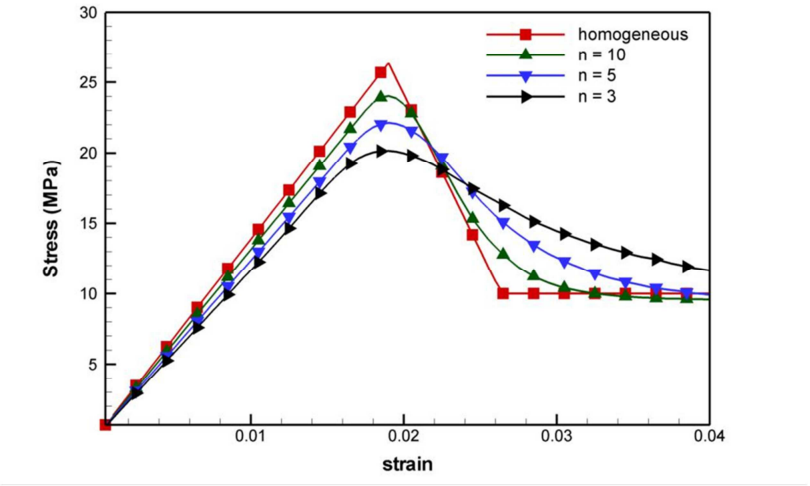

Fig. 4.6. Finite element results for triaxial stimulation with damage mechanics. The stress-strain curve varied with different levels of heterogeneity in Weibull distribution function.

4.3 Implementation of stress-dependent permeability model

The rock permeability change is also considered in the elastic phase and the damage phase (Tang et al., 2002; Yang et al., 2004):

$$k = k_0 e^{-\beta_d (\sigma_{ii}/3 - \alpha p)} \qquad (d = 0) \quad \text{..... (4.11)}$$

$$k = \zeta_d \, k_0 e^{-\beta_d (\sigma_{ii}/3 - \alpha p)} \qquad (d > 0) \quad \text{..... (4.12)}$$

where k_0 is the initial permeability and ζ_d` and β_d are material constants determined empirically. Here ζ_d (ζ_d >1) indicates permeability increase caused by damage. Parameter β_d in the exponent term is the control parameter for the stress sensitivity of permeability in the porous rock. This permeability model has been developed from experimental results of triaxial compressive tests. The model describes a decay of permeability while compressive stress increases in the elastic phase. After the rock fails, there is a step increase of permeability that decreases again with continuous compressive stress. The numerical results for permeability variations during the triaxial loading are illustrated in Fig. 4.7.

The changes of poroelastic parameters after rock failure are also important to study injection-induced nonlinear behavior of rock since the poroelastic constants are applicable for the elastic phase. Major poroelastic parameters to be considered after the rock failure are bulk modulus *K*, shear modulus *G*, Biot's constant α, and porosity ϕ. We considered the change of poroelastic parameters with damage evolution; for example, Biot's constant is 1 and the modulus of bulk solids and fluid are also reduced with the change of damage variables. Porosity related parameters are recomputed assuming porosity, ϕ is equal to the damage variable, *d* (Shao, 2002).

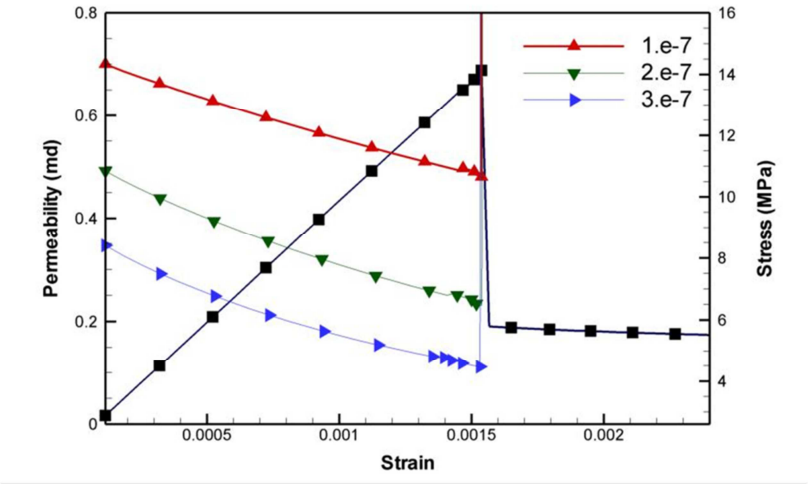

Fig. 4.7. Finite element results for permeability variation with triaxial simulation. Permeability varied with different material parameter, β_d.

4.4 Numerical analysis of the thermo-poro-mechanical process with damage evolution and permeability change

In this section, we present numerical examples for damage evolution and permeability alteration while considering poroelasticity and thermo-poroelasticity with convective heat transfer. First, we present poroelasticity and thermo-poroelasticity results without in-situ stresses to focus on the induced increments of damage and permeability around a wellbore.

4.4.1 The influence of damage evolution and permeability change in isothermal conditions

Consider the influence of fluid flow around a wellbore under isothermal reservoir conditions with pressure boundary conditions. We used 350 elements with 1141 nodes to

simulate the domain of 5×5 m with a wellbore of radius 0.1 m (Fig. 4.8). No in-situ stress and no initial pore pressure are applied in initial reservoir conditions, and a wellbore pressure of 12 MPa is used in the simulation.

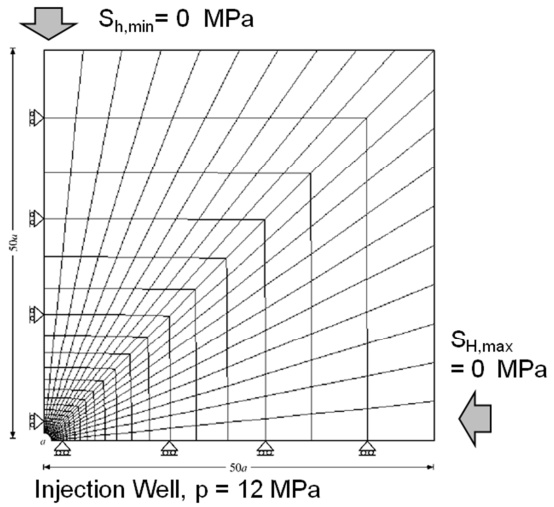

Fig. 4.8. Finite element mesh for coupled thermo-poroelasticity damage model consisting of 350 elements and 1141 nodes; zero in-situ stress pore pressure; wellbore pressure of 12 MPa.

Table 4.1
Rock properties of sandstone.

Young's modulus E (GPa)	7.92
Drained Possoin's ratio υ	0.14
Undrained Possoin's ratio υ_u	0.35
Skempton's coefficient, B	0.77
Permeability, k (md)	1
Porosity, ϕ	0.19
Fluid mass density, ρ_f (kg/m^3)	1000
Fluid viscosity, μ (Pa·s)	1×10^{-3}
Thermal expansion coefficient of solid, α_m (K^{-1})	1.8×10^{-5}
Thermal expansion coefficient of fluid, α_f (K^{-1})	3.0×10^{-4}
Thermal diffusivity, c^T (m^2/2)	1.6×10^{-6}

Damage evolution for this problem is presented in Fig. 4.9. The damage propagation in time is very slow for the pressure boundary condition. Rock failure around the wellbore is caused by tensile failure as the effective tensile stress dominates the failure around the wellbore. Fig 4.10 shows the distributions of permeability. A step increase is observed in the damage phase caused by microcrack and void growth in the rock. The resulting pore pressure distribution is discontinuous because of the high permeability in the damage phase (Fig. 4.11). The influence of damage and altered permeability is shown in comparison with the homogeneous poroelastic results in Fig. 4.11, where the solid lines represent the effect of damage and permeability change and dashed lines show the poroelastic results without damage and permeability increase (reference case). The distributions of total radial stress and tangential stress are plotted in Fig. 4.12 and Fig. 4.13; note that total radial stress distributions in the damage phase are relatively higher than in the reference case because the pore pressure is higher in the damage phase. From a stress analysis point of view, this small discontinuity of total radial stress between the damaged and elastic phase is caused by the lack of sufficient fluid movement at the interface between damaged and undamaged zones; that is, at the boundary between the high permeability and low permeability zones. Different fluid pressures in these zones cause a discontinuity of total stress between the damaged and elastic phases.

Fig. 4.14 and Fig. 4.15 illustrate the effective radial and tangential stress around the wellbore. The solid lines in Fig. 4.14 and Fig. 4.15 represent the poroelastic case with damage evolutions and permeability alterations whereas the dashed lines are for the

reference case. It is observed that the effective stresses in the damage phase are reduced in comparison to the reference case because of stress relaxation. However, stress concentration is observed between the damage and the elastic phase. This stress concentration effect between damage phase and intact rock drives damage propagation similar to the case of fracture propagation theory.

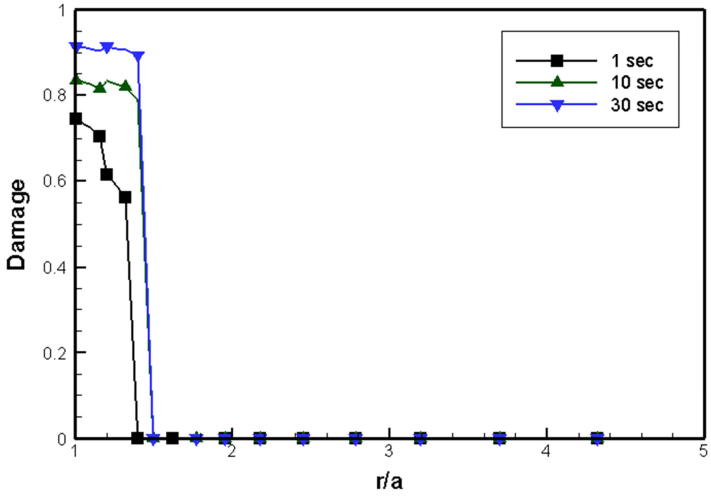

Fig. 4.9. Damage evolution around a wellbore.

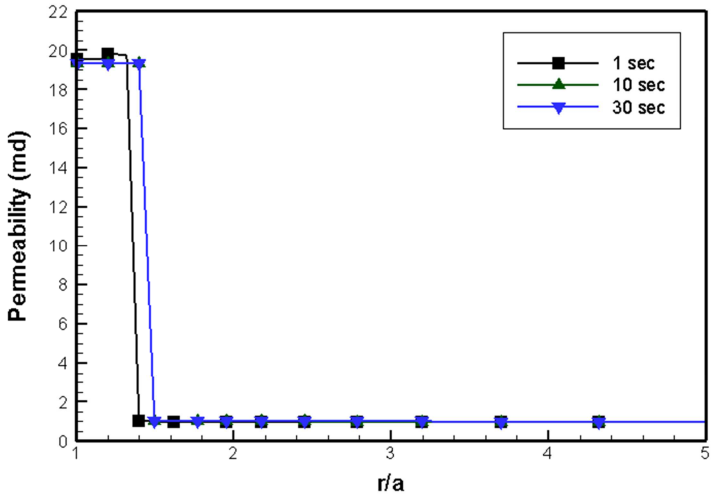

Fig. 4.10. Permeability distribution around the wellbore.

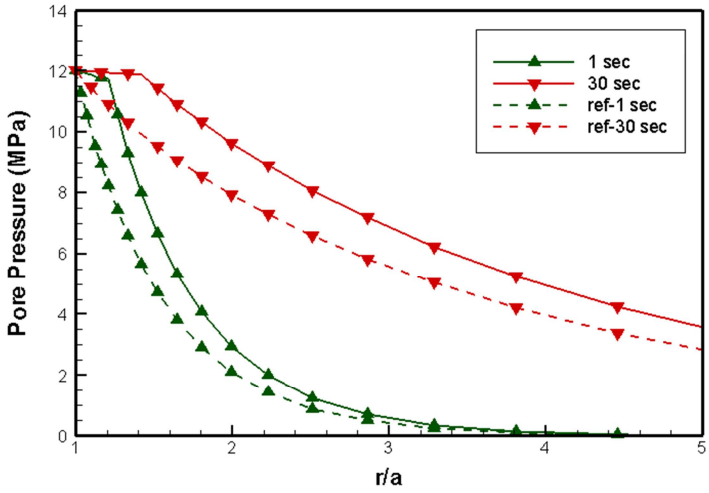

Fig. 4.11. Comparison of pore pressure distributions for simulations with and without damage. Solid lines: pore pressure distributions for damage evolutions and permeability change; dashed lines: the reference results from no damage and no step increase in permeability.

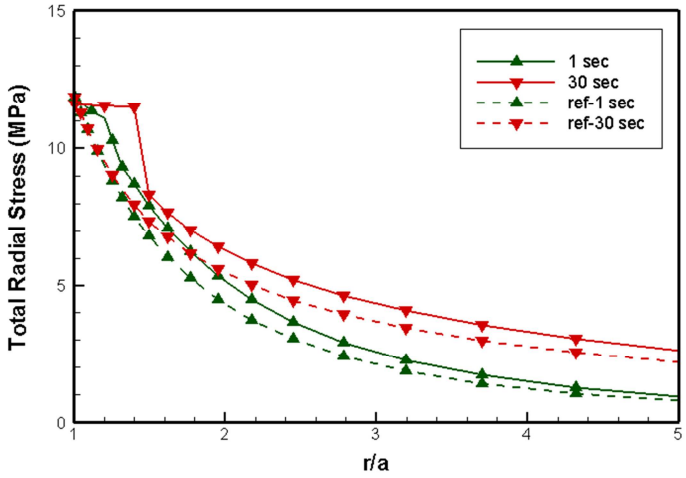

Fig. 4.12. Total radial stress distributions showing damage and altered permeability effects around a wellbore. Solid lines: stress distributions for damage case; dashed lines: the reference cases with no damage.

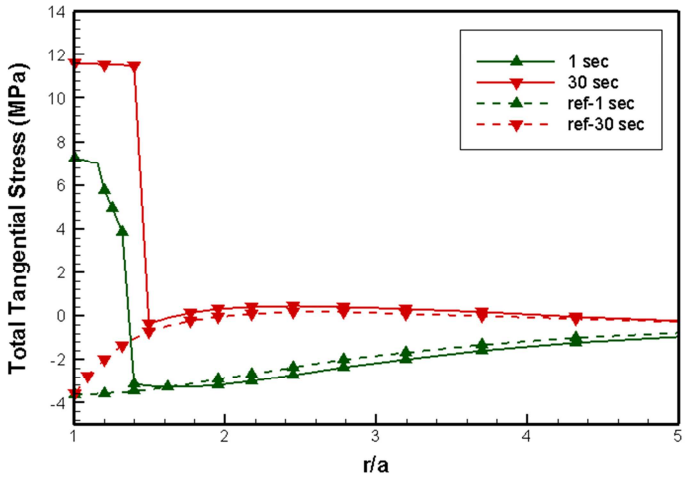

Fig. 4.13. Total tangential stress distributions showing damage and altered permeability effects around a wellbore. Solid lines: damage evolution and permeability change; dashed lines: reference case with no damage.

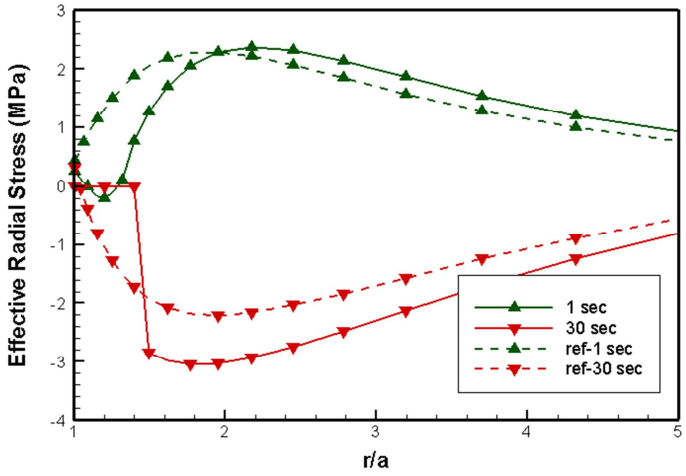

Fig. 4.14. Effective radial stress distributions around the wellbore. Solid lines: damage evolution included; dashed lines: no damage considered.

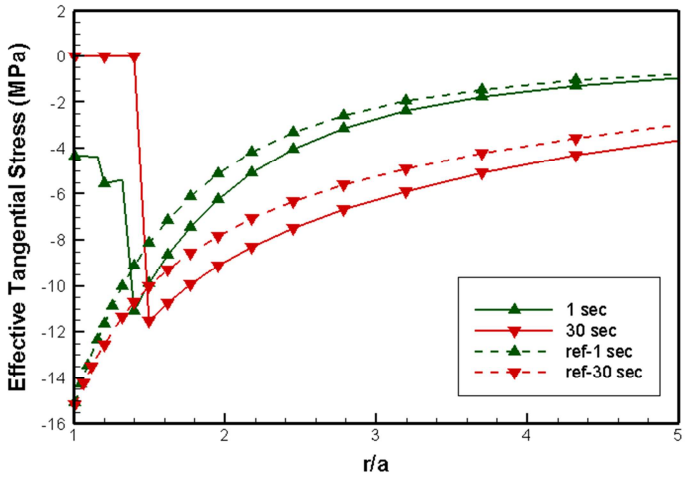

Fig. 4.15. Effective tangential stress distributions showing effects of damage and altered permeability around the wellbore. Solid lines: damage evolution; Dashed line: no damage.

4.4.2 The influence of damage evolution and permeability change in non-isothermal condition

Thermo-poroelastic simulations were performed while considering damage evolution and permeability alteration. Both conduction and convective heat transfer have been applied with fluid velocity computed using Darcy's law. We used the same 350 elements and 1141 nodes mesh in the thermo-poroelasticity case (Fig. 4.16). The penalty method is used for the pore pressure and temperature boundary conditions at the wellbore wall. Initial reservoir conditions of no in-situ stress and no pore pressure are first used to explain the pure effects of damage evolution in the fully coupled thermo-hydro-mechanical simulations.

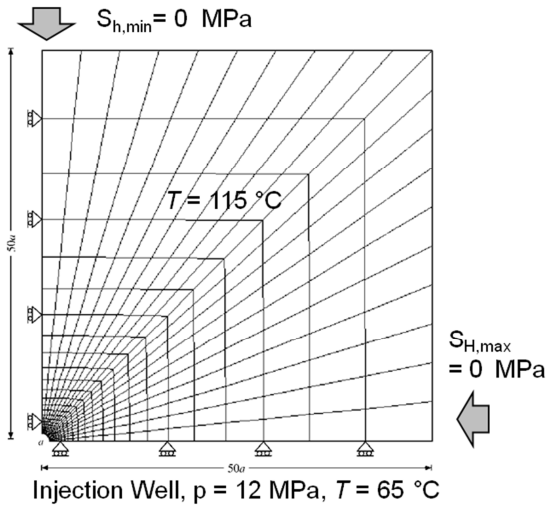

Fig. 4.16. Finite element mesh for the problem: 350 elements and 1141 nodes. Initial reservoir temperature is 115 °C, and wellbore pressure is 12 MPa.

The cooling associated with cold water injection in hot reservoir gives rise to tensile stresses associated with rock shrinkage. As a result, cooling influences the stress distributions differently from the isothermal conditions, as reflected in the distributions of damage variable as shown in Fig. 4.17; permeability distributions appear in Fig. 4.18. The effect of convective cooling around the wellbore is shown in Fig. 4.19. The solid lines represent the temperature profiles caused by both conduction and convection, whereas dashed lines are for the case of cooling by conduction only. We observe that the effect of convective cooling on temperature distribution can become significant, which in turn impacts the stress distributions around the wellbore caused by thermal stress. The pore pressure distributions are discontinuous at the interface due to the altered permeability in the damage phase as in Fig. 4.20. The total radial and tangential stress distributions are plotted in Fig. 4.21 and Fig 4.22, and effective stresses are plotted in Fig. 4.23 and Fig. 4.24. Again, we observe discontinuity in the total stress resulting from pore pressure discontinuity related to damage and relaxation of effective stress in the damage phase.

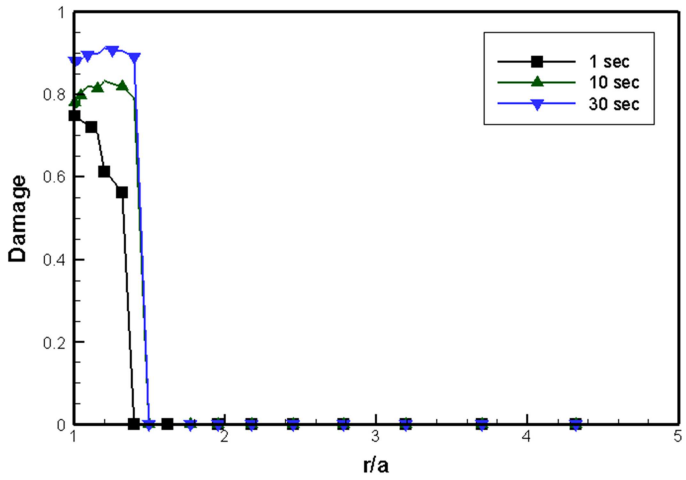

Fig. 4.17. Damage evolution around the wellbore.

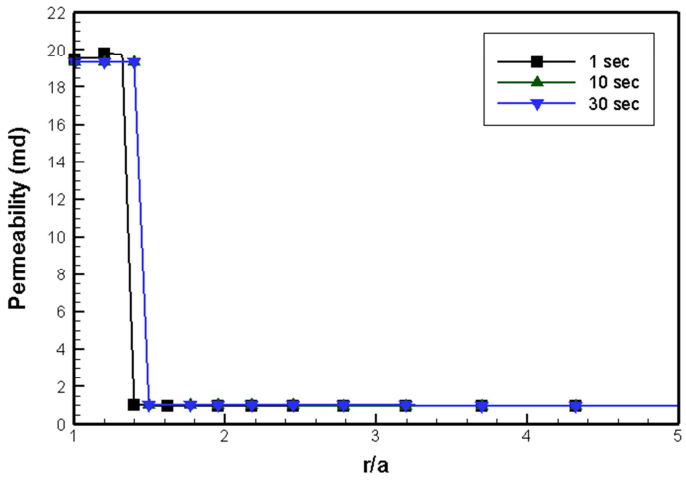

Fig. 4.18. Permeability distributions around the wellbore.

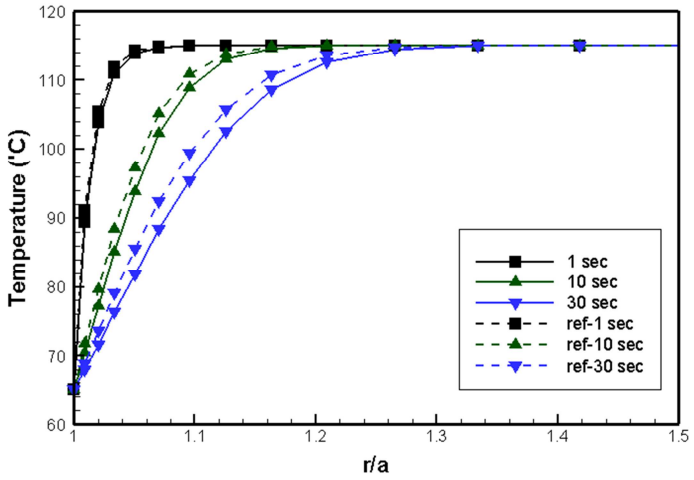

Fig. 4.19. Temperature distributions around the wellbore.

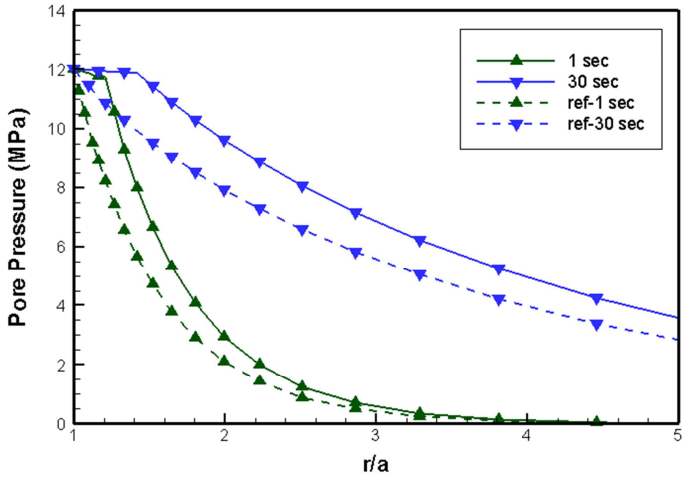

Fig. 4.20. Pore pressure distributions around the wellbore. Solid lines represent pore pressure distributions for damage; dashed lines give the results for the reference case with no damage.

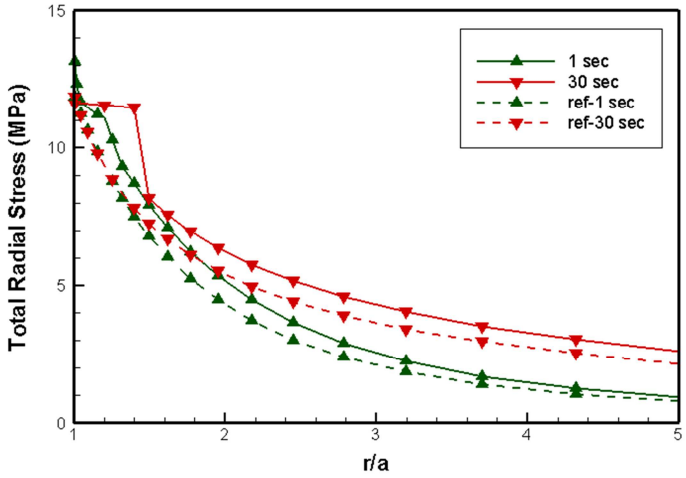

Fig. 4.21. Total radial stress distributions around the wellbore. Solid lines: with damage; dashed lines: no damage.

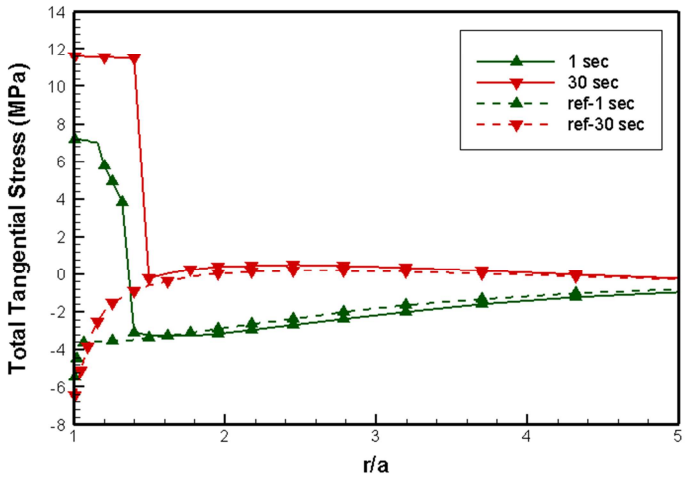

Fig. 4.22. Total tangential stress distributions comparing the damage and altered permeability effects around the wellbore. Solid lines: with damage evolutions and permeability change; dashed lines: reference case with no damage.

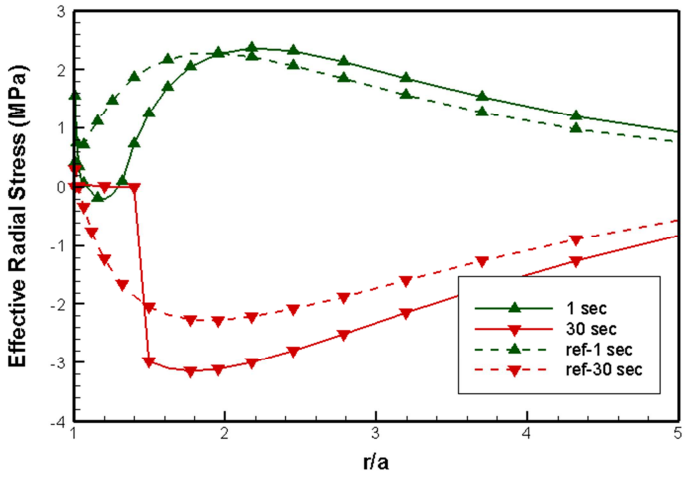

Fig. 4.23. Effective radial stress distributions around the wellbore showing the impact of damage and altered permeability. Solid lines: with damage evolution and permeability change; dashed lines: no damage and permeability increase.

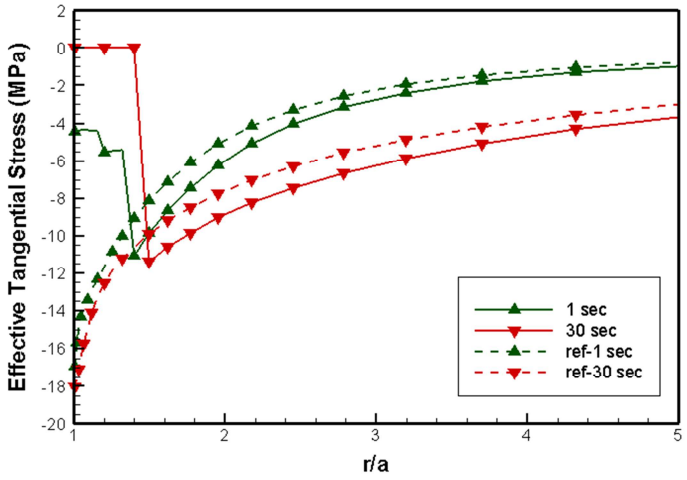

Fig. 4.24. Effective tangential stress distributions. Solid lines: damage evolutions and permeability change; dashed lines: no damage and no step increase of permeability.

4.5 Discussion

Damage and stress-dependent permeability models were applied to the theory of thermo-poroelasticity. Stress distributions with implementation of damage mechanics and the permeability model has been compared with a reference case (constant modulus and permeability). Stress relaxation occurred by modulus alteration and concentration of effective hoop stress at the interface between the damaged and undamaged rock. Also, pore pressure distribution shows the discontinuity at the interface due to the increase of permeability in the damaged area.

The damage model used in this section considered nonlinear behavior of strain-stress for the shear and tensile failure. This model can describe softening and residual strength regime with change the parameters f_{cr}, f_{tr}, and ε_{cr} better than other suggested damage models that include exponential terms in their equations (Mazars, 1986; Cheng and Dusseault, 1993; Selvadurai, 2004). These exponent-based damage models can depict the hardening and softening process smoothly; however, it is not convenient to control the desired softening regime and residual strength regime. For our applications, it is important to consider softening and residual strength since reservoir rocks (shale, sandstone, and granite) show brittle behavior with a short range of hardening regime.

5. CHEMO-THERMO-PORO-MECHANICAL FINITE ELEMENT ANALYSIS WITH DAMAGE EVOLUTION AROUND A WELLBORE IN SWELLING SHALE

Wellbore stability is important when drilling for oil and gas. Especially, well design must consider the influence of hydraulic pressure, temperature, and chemical osmosis in shale drilling in high pressure and high temperature. The interaction of solid and fluid in porous rock has been firstly developed by Biot's poroelastic theory (Biot, 1941; Cryer, 1963), and this theory has been extended with the influence of temperature, fluid flow, and rock deformation by thermo-poroelasticity (McTigue, 1986; Kurashige, 1989, Wang and Papamichos, 1994). These authors have shown the impact of thermal stress in wellbore stability: thermally induced pore pressure change can be significant in low permeability formations. The shale deterioration by chemical influence under isothermal condition around a wellbore has been studied extensively; the main driving mechanism of fluid flow is the chemical potential gradient in low permeability shale reservoirs. Heidug and Wong (1996) proposed constitutive equations for swelling shale based on nonequilibrium thermodynamics. Ghassemi and Diek (2003) considered combined effects of chemical potential and thermal osmosis on water flow in and out between the mud and shale formation. They indicated that thermal-osmosis flows are several times higher than hydraulic pressure in certain conditions. On the other hand, the chemo-poroelasticity model is not easy to implement because of its nonlinearity characteristics in physical parameters so that it can be simplified with linear chemo-

thermo-poroelastic models if the difference of concentration is not severe (Ghassemi and Diek, 2003). The assumptions of elasticity and constant permeability in shale drilling have limitations in predicting the real behavior of shale around a wellbore. In addition, the strength of shale is weak, so that it is important to predict the stress changes precisely around a wellbore influenced by hydraulic pressure, mass solute concentration, and temperature. Generally, the stress and strain behavior for shale in triaxial tests shows the hardening and softening with compressive or tensile stress (Yuan and Harrison, 2006). The damage mechanics model is one of the methods to describe this hardening and softening behavior of rock. Continuum damage mechanics was first introduced by Kachanov and since has been developed by many researchers (Kachanov, 1958; Mazars, 1986; Simankin and Ghassemi, 2005; Tang et al., 2002; Li et al., 2005; Selvadurai, 2004) who have studied the inelastic rock behavior due to crack initiation, void growth, and crack growth. This damage mechanics model has been applied to poroelasticity by Selvadurai, who applied consolidation problems with altered moduli and permeability change. Also Hamiel et al. (2005) proposed a damage model in poroelastic rock and applied the model to the triaxial simulation, considering the time dependent degradation and healing process for a damage variable which is dependent on modulus, porosity, and Poisson's ratio. Tang et al. (2002) proposed an isotropic damage model based on Kachanov's (1959) effective stress hypothesis. Also he presented the permeability model which describes stress-dependent behavior in the elastic phase and altered permeability after the rock failure based on triaxial tests by measuring the permeability change with stress variation (Tang et al., 2002). This permeability change by rock failure has been

studied by many researchers (Shipping et al., 1994; Kiyama et al.; 1996, Coste et al., 2001; Zoback and Byerlee, 1975). Their experimental results for tests on several rocks show permeability increase by a factor of two to four, and this increase of permeability by rock failure depends on the rock type and conditions (De Paola et al. 2009; Wang and Park, 2002).

This section presents the development of a finite element method to study the influence of chemo-thermo-poromechanical coupling on shale damage evolution and permeability alteration around a wellbore. The damage model describes the change of modulus with rock failure by water activity and thermal stress around a wellbore. A number of simulations are presented to verify the model and to illustrate the role of damage mechanics and stress-dependent permeability and resulting stress distribution by thermal stress and chemical osmosis. In addition, we present the different distributions of damage under different far-field stresses and compare the influence of temperature and chemical potential.

5.1. Finite element results for chemo-thermo-poroelasticity

In this section, we briefly present two-dimensional finite element results around a wellbore to study the influence of fluid flow, solute transport, and temperature. The simulation domain is 12×12 m^2 (Fig. 5.1) and is divided into 8000 eight-noded quadrilateral elements. The individual shape functions in the mixed approximation will not yield meaningful results (Zienkiewicz and Taylor, 1991). Overcoming this numerical inaccuracy requires double degrees of freedom for displacements in the presence of large

changes of stresses, pressure, concentration, and temperature around the wellbore. Details of shale properties in this simulation are illustrated in Table 5.1. Maximum and minimum far-field stress are 25 MPa and 15 MPa, respectively, and initial pore pressure and temperature are 10 MPa and 115°C. Mud pressure and temperature are set to 15 Pa and 65°C. Solute concentration in mud and shale formations are C_{mud}=0.1 C_{shale} = 0.2, respectively.

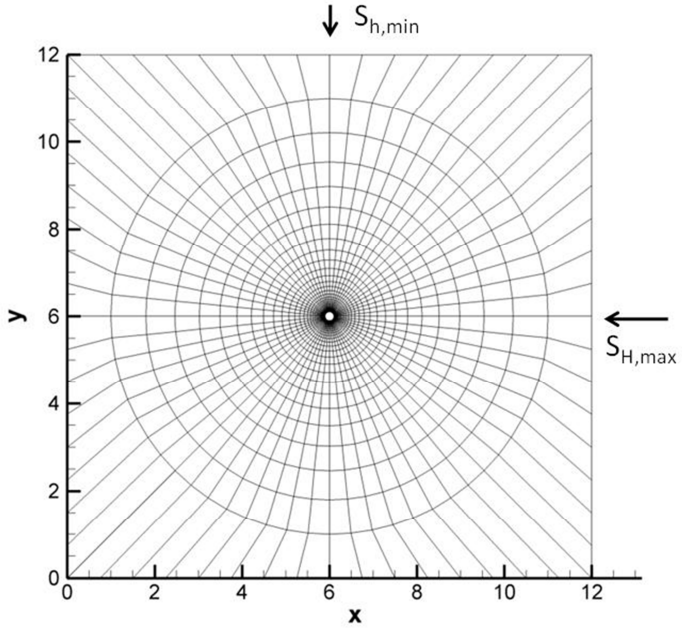

Fig. 5.1. Mesh used for finite element simulation.

Table 5.1
Input material properties for shale.

Young's modulus E (GPa)	1.853
Drained Possoin's ratio υ	0.219
Undrained Possoin's ratio υ_u	0.461
Biot's coefficient, α	0.966
Permeability, k (md)	1×10^{-6}
Porosity, ϕ	0.299
Fluid mass density, ρ_f (kg/m^3)	1111.11
Fluid viscosity, μ (Pa·s)	1×10^{-3}
Thermal expansion coefficient of solid, α_m (K^{-1})	1.8×10^{-5}
Thermal expansion coefficient of fluid, α_f (K^{-1})	3.0×10^{-4}
Thermal diffusivity, c^T (m^2/2)	1.6×10^{-6}
Reflection coefficient, $\Re$	0.2
Swelling coefficient, ω_0 (MPa)	1.5
Solute diffusivity, D^s (m^2/2)	2.0×10^{-9}

We compared the results which consider the influence of fluid flow, temperature, and solute transport based on poroelasticity, thermo-poroelasticity, and chemo-thermo-poroelasticity. Pore pressure distributions for isothermal and nonisothermal cases are plotted in Fig. 5.2 (a) and (b). The deviatoric far-field stress causes the lower pore pressure to the maximum far-field stress direction because of the tensile stress around a wellbore, and higher pore pressure to the minimum far-field stress direction because of the compressive stress. The influence of temperature is described in Fig. 5.2(b). Note that the difference of temperature between the mud and shale formation generates thermal stress as tensile around a wellbore because of rock shrinkage; therefore, the fluid disperses more easily than in the isothermal condition. Fig. 5.2(c) represents the influence of solute transport (C_m=0.1, C_{shale}=0.2) that the osmosis flow cause localized

pore pressure inside the shale formation. The result for the fully coupled case has been described in Fig. 5.2(d). The effective radial and hoop stress distributions with different coupling schemes are plotted in Fig. 5.3 and Fig. 5.4. It is observed that the fluid flow, temperature, and solute transport are critical to rock stress; the variations in hoop stresses are especially significant. This localization of stress distribution often reaches the rock failure criterion, so it is necessary to consider the stress variations after the rock failure. The rock damage with altered modulus and permeability will be discussed in the next section.

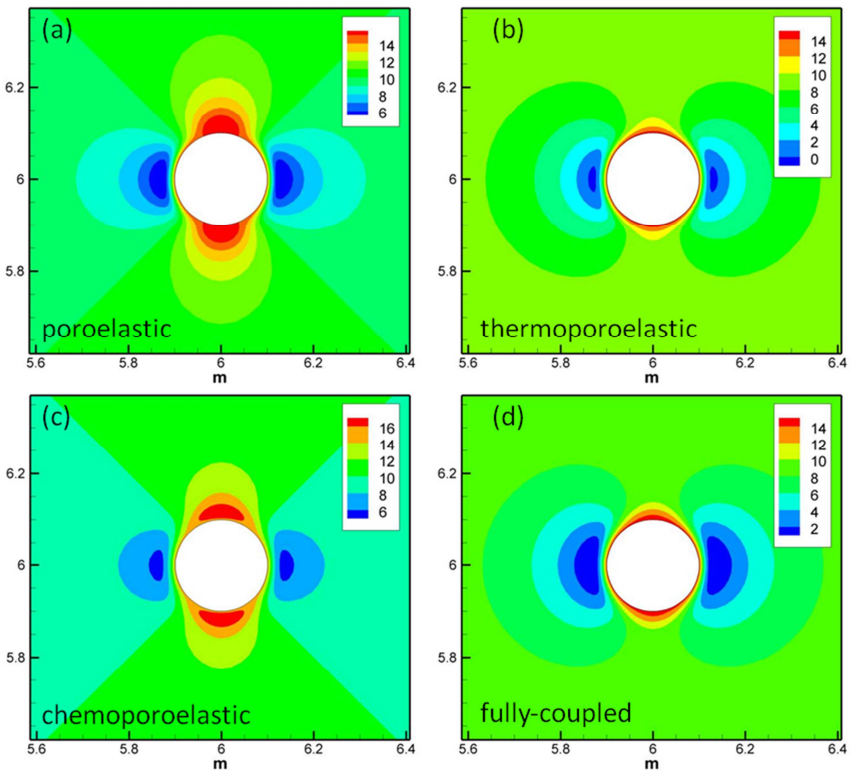

Fig. 5.2. Two-dimensional plots for pore pressure distribution. The solid-fluid interaction between the drilling mud and shale formation under anisotropic far-field stress is plotted in (a), the influence of thermal stress is in (b), chemical interaction with fluid is in (c), and fully coupled results are in (d).

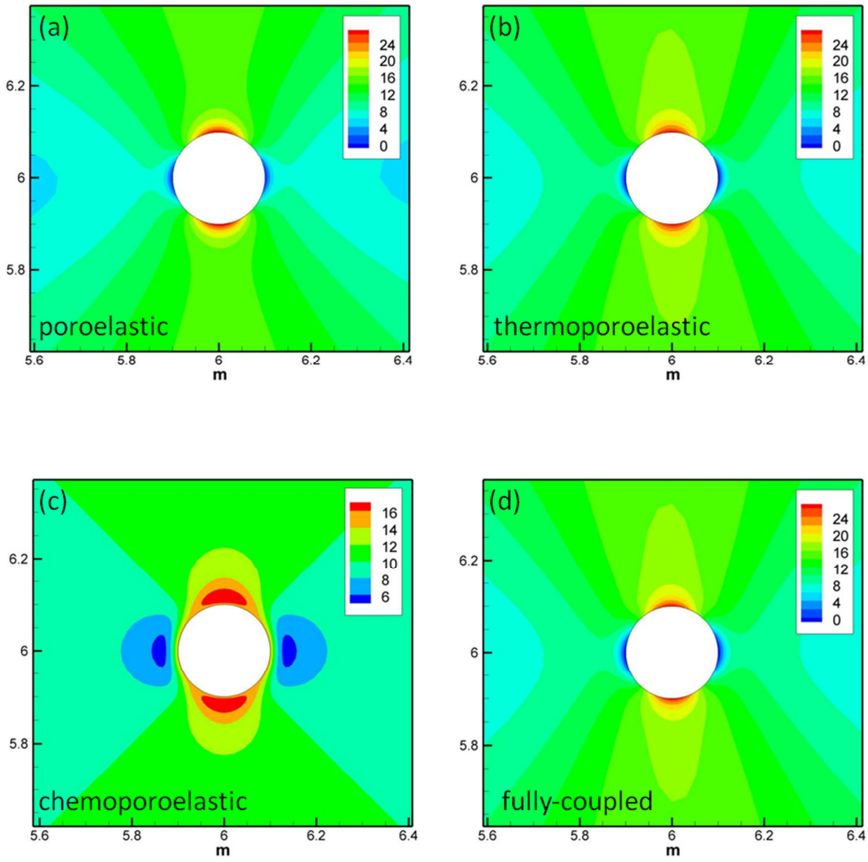

Fig. 5.3. Two-dimensional plots for effective radial stress distribution. The solid-fluid interaction between the drilling mud and shale formation under anisotropic far-field stress is plotted in (a), the influence of thermal stress is in (b), chemical interaction with fluid is in (c), and fully coupled results are in (d).

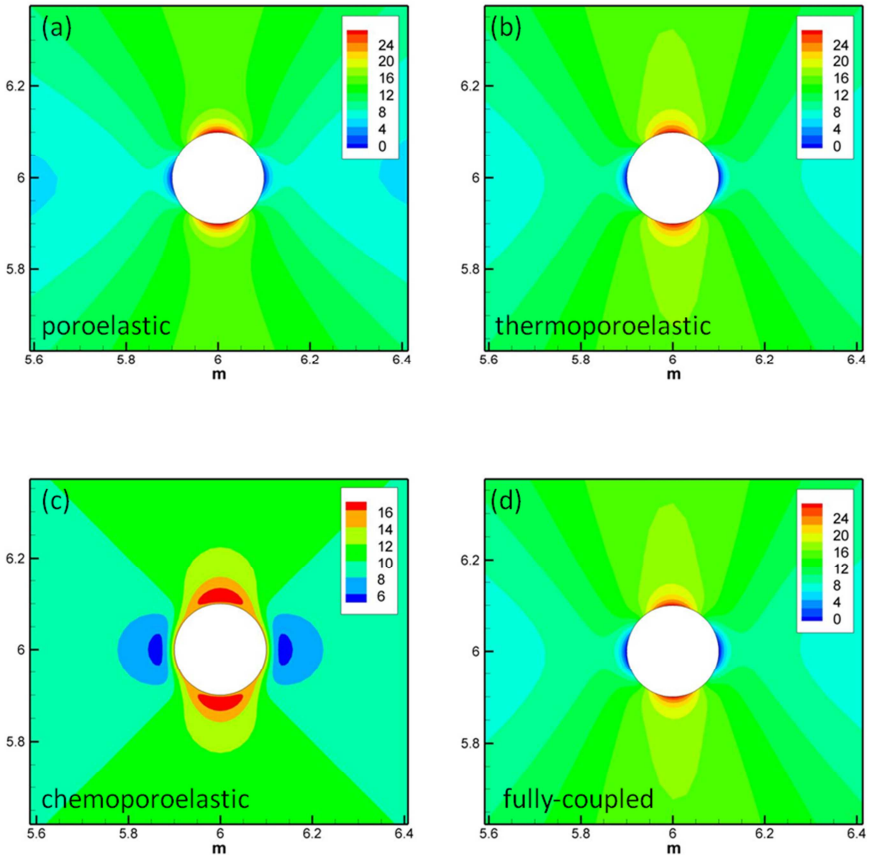

Fig. 5.4. Two-dimensional plots for effective tangential stress distribution. The solid-fluid interaction between the drilling mud and shale formation under anisotropic far-field stress is plotted in (a), the influence of thermal stress is in (b), chemical interaction with fluid is in (c), and fully coupled results are in (d).

5.2 Influence of temperature and salinity in shale damage

To illustrate the role of various mechanisms on wellbore damage, we considered the example of nonisothermal drilling in shale subjected to a stress field given by the maximum component of 25 MPa parallel to the x-axis and a minimum far-field component of 15 MPa in the y-direction. We assumed that initial pore pressure is 10

MPa and the mud pressure is 15 MPa. The initial shale formation temperature is 115°C and mud temperature assumed to be 65°C. Two different mud salinities of 0.3 and 0.1 are considered, and the wellbore integrity is analyzed after 12 hours of drilling.

The roles of temperature, salinity, and stress have been considered (Ghassemi et al., 2009; Zhou and Ghassemi, 2009), and it is known that for conventional rock response, cooling tends to reduce the shear failure potential while enhancing tensile failure. Also, high mud salinity reduces induced pore pressure and increases the effective radial stress at the wellbore wall. A lower mud salinity enhances flow into the rock and contributes to higher pressure distribution around a wellbore.

Fig. 5.5 shows the comparison of damage propagation with respect to the degree of coupling and different chemical gradients. Note that Fig. 5.5 (a)-(d) show different rock failure distributions for different levels of coupling between thermal, poroelastic, and chemical processes. As shown in Fig. 5.5 (a), the poroelastic analysis shows that a small zone of rock damage develops in the direction of minimum stress. If cooling is taken into account, the shear failure is circumvented and no shear damage is observed. However, a small zone of tensile failure occurs in the direction of maximum in-situ stress response to cooling [Fig. 5.5 (b)]. This is because the tendency of rock to shrink reduces the compressive hoop stress and amplifies the tensile stress.

The impact of chemo-poroelastic effect is shown in Fig. 5.5 (c), where it is assumed that the drilling mud has lower salinity than shale. In this case, osmosis and chemically-induced stresses affect damage evolution around the wellbore. Fluid movement from the mud to the shale contributes to the higher pore pressure around a

wellbore, leading to a large damaged area in the direction of minimum in-situ stress. The extent of failure zone is substantially reduced in this case, when the role of cooling is taken into account. Fig. 5.5 (d) shows that a fully-coupled simulation (hydraulic, thermal, and chemical osmosis) shows a much smaller shear failure zone but with a small tensile failure zone.

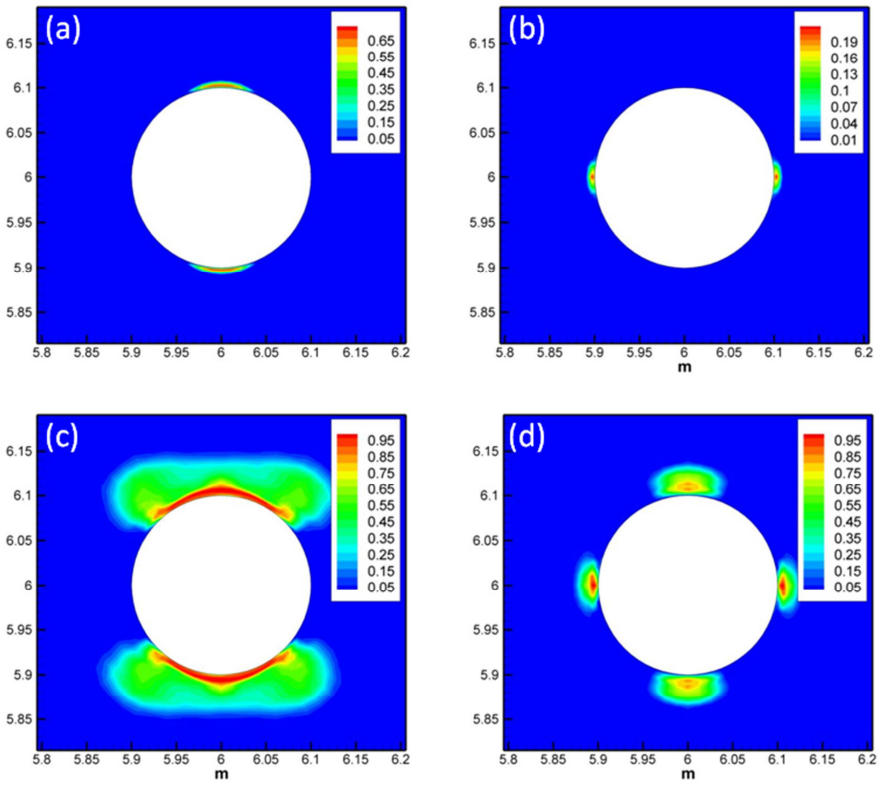

Fig. 5.5. The comparison of damage propagation at 12 hr with different coupling in numerical simulations. Results are compared with same conditions of mud salinity C_{mud} = 0.1, C_{shale} = 0.2, $S_{H,\max}$ = 25 MPa, and $S_{h,\min}$ = 15 MPa. Poroelastic damage I plotted in (a), cooling effects are present with thermo-poroelastic damage in (b), (c) shows the influence of osmosis flow with chemo-poroelastic behavior, (d) is fully-coupled chemo-thermo-poroelastic damage distribution.

The distributions of pore pressure for the different coupling levels (Fig. 5.6) is the lowest in the thermo-poroelasticity case and the highest in the chemo-poroelasticity case of a lower salinity mud.

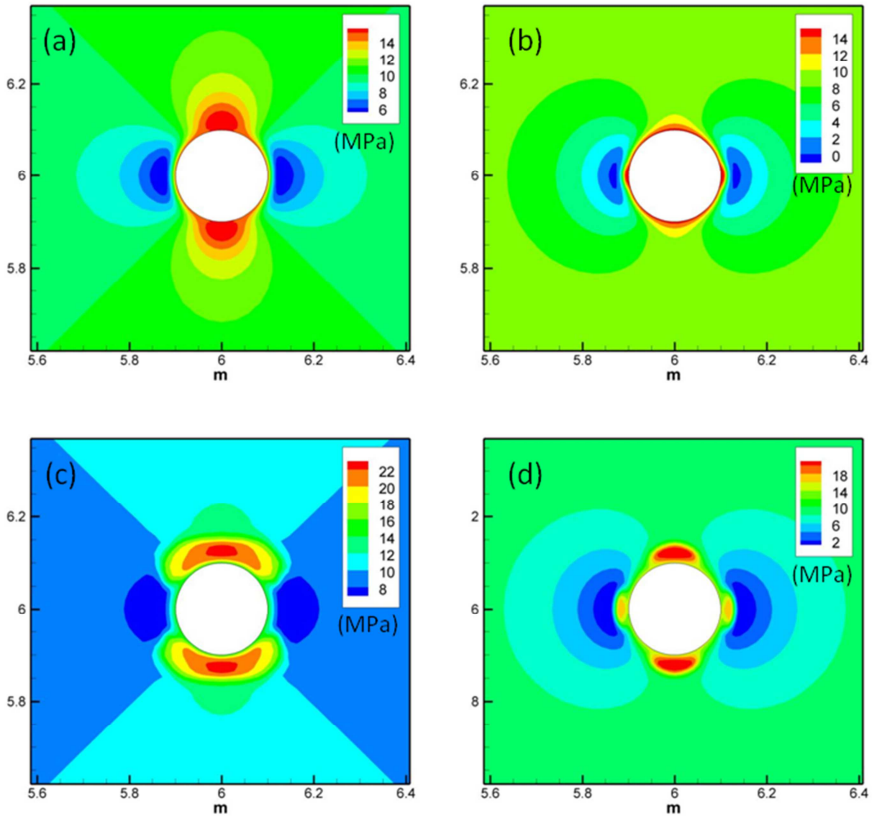

Fig. 5.6. The comparison of pore pressure distributions at 12 hr with different coupling in numerical simulations. Results are compared with same conditions of C_{mud} = 0.1 and C_{shale} = 0.2, $S_{H,max}$ = 25 MPa, and $S_{h,min}$ = 15 MPa. (a) poroelastic, (b) thermo-poroelastic, (c) chemo-poroelastic, (d) chemo-thermo-poroelastic pore pressure distribution.

The impact of stress-dependent modulus and permeability is easily captured with the model. Referring to Fig. 5.7, it is observed that the failed-zone is larger when we consider the variation of modulus and permeability. This effect can be explained by

stress redistribution and the permeability effect. In constant modulus and permeability conditions, the stress distributions are same with rock failure. However, once the modulus reduced and permeability increased in the failed area, effective stresses reduced and pore pressure increased. These discontinuities in stress and pore pressure in the damage phase perform as barriers between the damaged and undamaged areas so that effective stresses are increased at the interface. This amplification of effective stresses in altered modulus and permeability resulted in larger damage distributions than constant modulus and permeability.

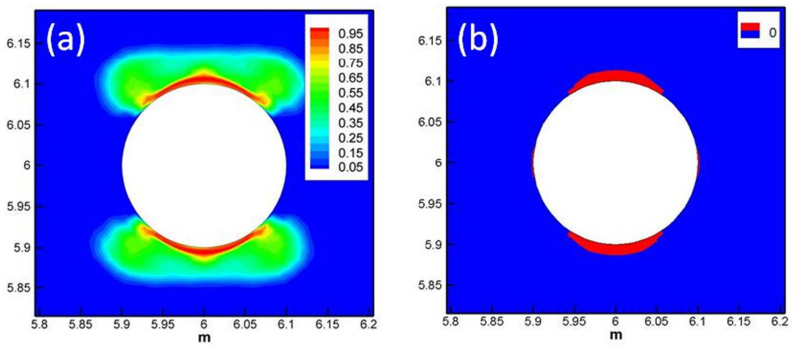

Fig. 5.7. The influence of modulus and permeability change for rock failure distributions. Results are compared with same conditions of lower mud salinity and $S_{H,\max}$ = 25 MPa, $S_{h,\min}$ = 15 MPa. (a) chemo-poroelastic rock failure with altered modulus and stress-dependent permeability (d) chemo-thermo-poroelastic rock failure with constant modulus and permeability model.

Another wellbore example to consider is the influence of mud salinity. The maximum far-field stress is 25 MPa and the minimum far-field stress is 15 MPa. We assumed that the initial pore pressure is 10 MPa and the mud pressure is 15 MPa. The

initial shale formation temperature is 115 °C and the mud temperature is assumed to be 65°C. As before, two different mud salinities of 0.3 and 0.1 were considered, and the wellbore integrity was analyzed after 12 hrs of drilling.

Fig. 5.8 shows that slight damage observed to the maximum far-field stress direction when the mud salinity is higher than shale formation. When the mud salinity is lower than the formation, there are high damage by shear and tensile to the both maximum and minimum far-field stress directions. It is widely known that pore pressure increase in porous rock causes shear or tensile failure because of the effective stress reduction by fluid movement. The influence of osmosis flow from the mud to the shale causes higher pore pressure around a wellbore, and then it reached the shear and tensile failure to the maximum and minimum far-field stress direction. The comparison of pore pressure distributions around a wellbore has been presented in Fig. 5.9.

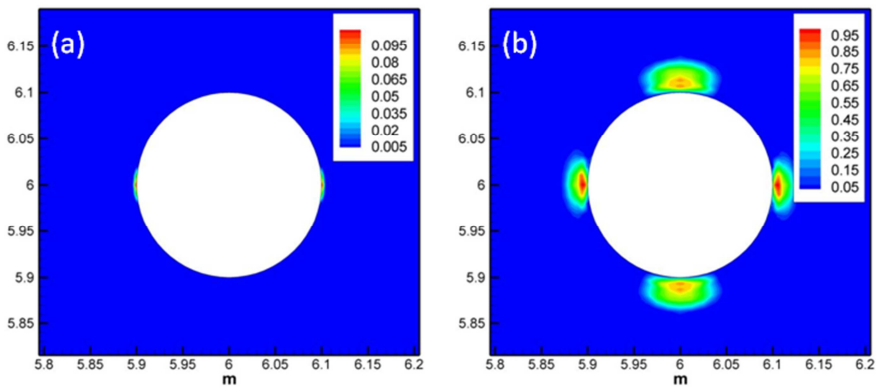

Fig. 5.8. Damage distributions at 12 hr with $S_{H,max}$ = 25 MPa, $S_{h,min}$ = 15 MPa. (a) higher mud salinity ($C_{mud} > C_{shale}$) (b) lower mud salinity ($C_{mud} < C_{shale}$)

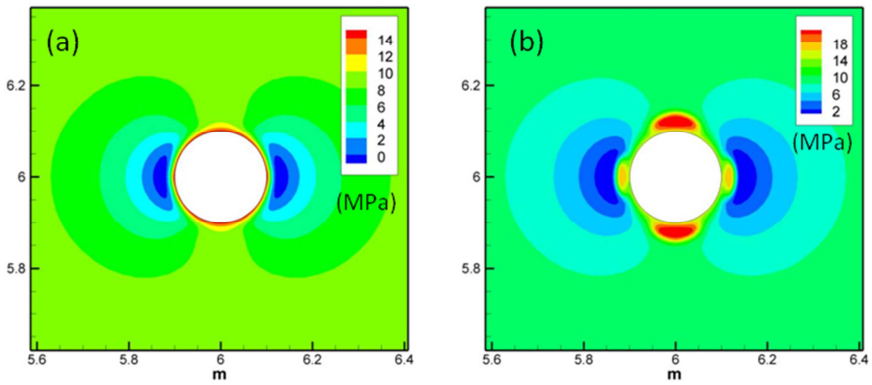

Fig. 5.9. Pore pressure distributions at 12 hr with $S_{H,max}$ = 25 MPa, $S_{h,min}$ = 15 MPa. (a) higher mud salinity ($C_{mud} > C_{shale}$) (b) lower mud salinity ($C_{mud} < C_{shale}$)

Fig. 5.10 shows the damage propagation with time. It is observed that shear failure occurred to the minimum far-field stress direction because of highly compressive effective hoop stress and then tensile failure to the maximum far-field stress direction begins as following the shear failure due to the osmosis flow invasion from the mud to the shale formation with respect to time. The distributions of temperature and solute concentration are plotted in Fig. 5.11 (a) and (b) for the case of lower mud salinity under given mud pressure, in-situ stress, initial pore pressure, and temperature. Note that the effective radial and hoop stress in Fig 5.11 (c) and (d) shows the stresses are relaxed in damage phase and redistributed around a wellbore by modulus reduction and permeability increase in failed zone.

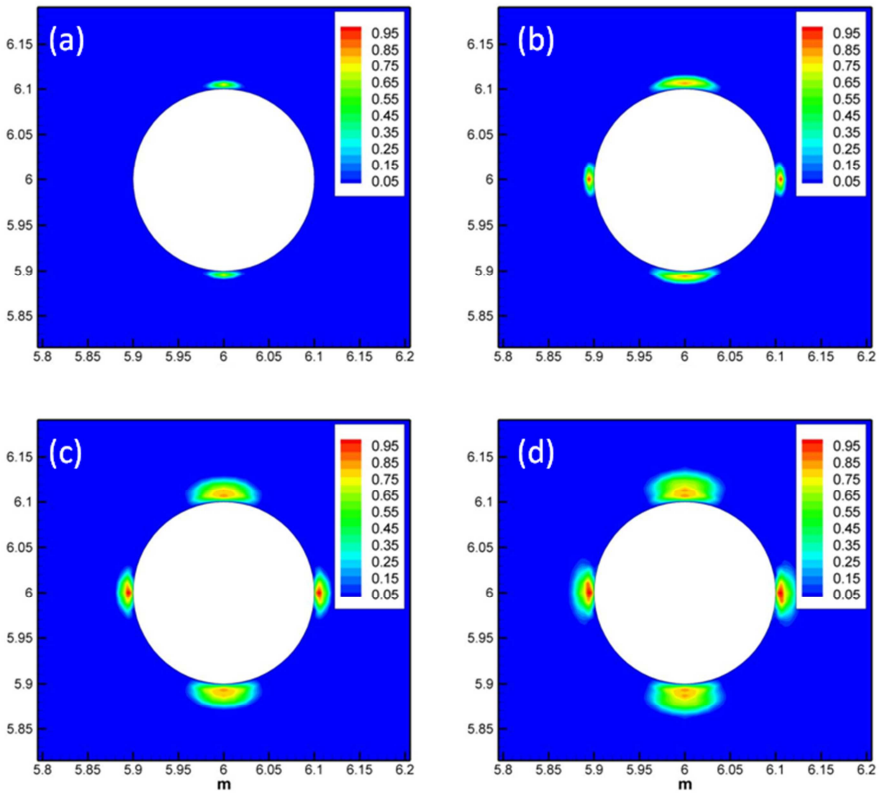

Fig. 5.10. Propagation of damage with respect to time with $S_{H,max}$ = 25 MPa, $S_{h,min}$ = 15 MPa. The case of lower mud salinity comparing shale formation (a) 0.5 hr (b) 1 hr (c) 3 hr (d) 6 hr.

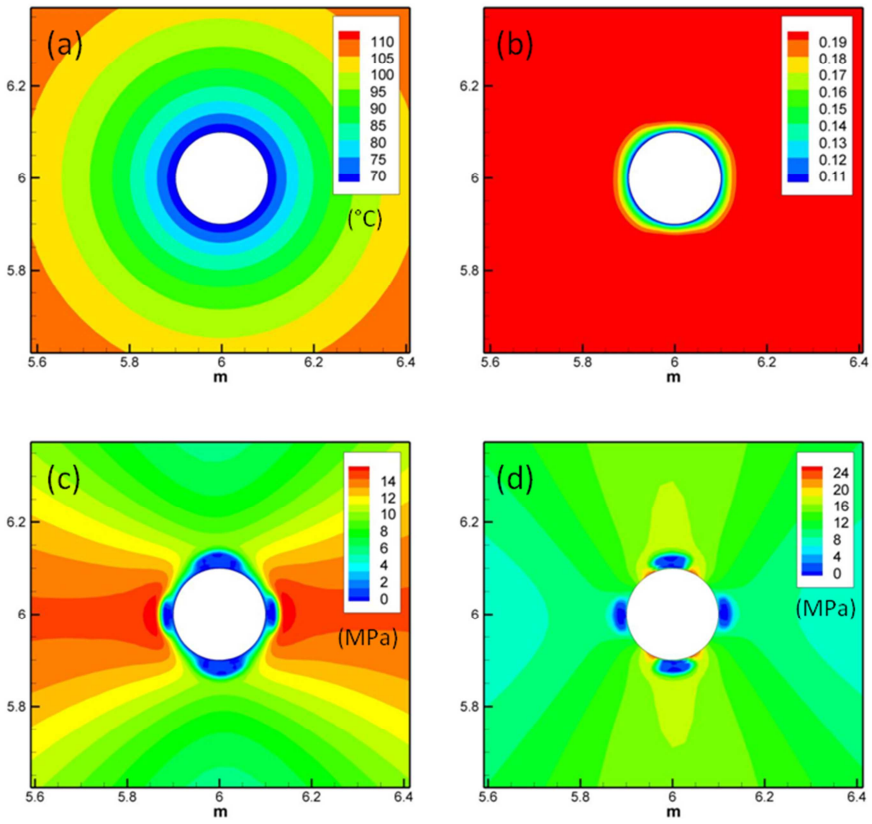

Fig. 5.11. The distributions of temperature (a), solute mass concentration (b) and effective radial and hoop stress distributions (c) and (d), respectively. All results are snap shots of 12 hr and the mud salinity C_{mud} = 0.1 and C_{shale} = 0.2 and $S_{H,max}$ = 25 MPa, $S_{h,min}$ = 15 MPa.

5.3 Conclusions

Two-dimensional fully coupled finite element methods have been developed for modeling damage-induced stress variations and permeability change around a wellbore. Results show the influence of chemical potential and thermal stress around a wellbore. It is clearly presented that the shale is unstable when the mud salinity is lower that

formation by osmosis flow and cooling creates tensile stresses by the difference of thermal expansion coefficients of solid and fluid. Model can explain the different distributions of damage and pore pressure with different mud salinity. Far-field stresses are also important in wellbore stability, it tends to be reached failure condition in lower mud salinity where the far-field stress is low, although the mud pressure is set to the range of initial pore pressure and fracture gradient. In addition, the coupling of hydraulic pressure, solute transport and temperature has been compared under same conditions. Results show the impact of the osmosis and temperature in the analysis of stress distributions. This study indicates that the finite element method with damage mechanics and stress-dependent permeability model can be used to model the swelling shale.

6. TWO-DIMENSIONAL THERMO-PORO-MECHANICAL MODELING OF WELL STIMULATION AND INDUCED MICROSEISMICITY

Stress analysis or rock mass failure in response to water injection is of much interest in geothermal reservoir design. The process involves coupled rock deformation and fluid flow as described in Biot's poroelastic theory (Biot, 1941; Cryer, 1963), and its thermo-poroelastic (McTigue, 1986) and thermo-chemo-poroelastic extension (Ghassemi et al. 2009). Chemical effects can be significant with respect to the clay swelling and solute transport and reactivity. Thermo-poroelasticity can be used to assess the influence of fluid flow and temperature change on the stress variations in the reservoir. This influence is often computed assuming a linear elasticity with constant mechanical and transport rock properties. The assumption of elastic rock skeleton and fluid flow and heat transport in porous media under constant permeability conditions has limitations in predicting the real behavior of the reservoir rock. Generally, the strain-stress behavior of rocks in triaxial tests shows hardening and post-peak softening. This behavior depends on the rock type, pore pressure, stress conditions, and temperature (Jaeger, Cook, and Zimmerman, 2007). The continuum damage mechanics approach is one of the methods that can capture the hardening and softening behavior of the rock (Yuan and Harrison, 2006). Continuum damage mechanics was first introduced by Kachanov and since has been developed and applied by many researchers (Kachanov, 1958; Mazars, 1986; Simankin and Ghassemi, 2005; Tang et al., 2002; Yang et al., 2004; Selvadurai, 2004) who have investigated inelastic behavior caused by crack initiation, microvoid growth,

and fracture propagation. Also, the evolution of rock damage in the presence of poroelastic and thermo-poroelastic effects has been considered. Selvadurai (2004) studied damage in poroelastic brittle rock. His results showed a significant permeability alteration caused by damage evolution in consolidation problems. Hamiel et al. (2005) developed a model with a time dependent damage variable, porosity, and material properties. They proposed different rock behavior with degradation and healing within the framework of the poroelastic theory. Tang et al. (2002) proposed a damage and permeability model based on experimental strain-stress observations and permeability measurements (Tang et al., 2002, Yang et al., 2004). The model was implemented in a finite element model and was used to simulate a uniaxial compression test and also hydraulic fracture propagation.

The permeability variations induced by altered stress and rock failure has been studied by many researchers (Shipping et al., 1994; Kiyama et al.; 1996, Coste et al., 2001; Zoback and Byerlee, 1975). Zoback and Byerlee illustrated the relation between permeability change and microcrack and void evolution. Their experimental results for tests conducted on granite show permeability increasing by a factor of four. Other studies present different magnitudes for the increase in permeability depending on rock type and conditions (De Paola et al. 2009; Wang and Park, 2002).

The stimulation of the reservoir rock mass is often accompanied by multiple microseismic events. Microseismic event characteristics such as their locations, spatial patterns of distribution, and temporal relations between the occurrence of seismicity and reservoir activities are often studied for enhanced geothermal systems (EGS).

Microseismic event detection and interpretation is used for estimating the stimulated volume and fracture growth, resulting reservoir permeability, and geometry of the geological structures and the in-situ stress state (Pine, 1984). The process commonly is referred to as seismicity-based reservoir characterization. Although progress has been made in quantitative and qualitative analysis of reservoir stimulation using micro earthquakes (Shapiro et al., 1997; 1999; 2002; Rothert and Shapiro, 2003), the process of rock failure and permeability change is not considered. Also, in-situ stress and thermal effects on fluid-rock interaction have not been considered.

In this work, we present the development of a finite element model to study the influence of thermo-poro-mechanical coupling on rock damage evolution and permeability variation with reference to reservoir stimulation and induced seismicity. The damage model we used corresponds to the brittle rock failure behavior with post peak softening and permanent deformation prior to the fracture. To capture the full effects of rock cooling by injection in the presence of higher fluid fluxes caused by rock failure and permeability enhancement, the model considers both the conductive and convective heat transfer in porous media. Two types of injection schemes are considered in this work: explicit wellbore geometry for small scale simulations and a point source approach for large scale simulations. A number of numerical simulations are presented to verify the model and to illustrate the role of various mechanisms in rock fracture,

6.1 Well stimulation and injection-induced microseismicity

Two-dimensional fully-coupled thermo-poromechanical simulations have been conducted with an altered modulus and permeability model. Mesh information for these simulations is as follows: 12,000 quadrilateral elements for a 200×200 m^2 simulation domain which has a wellbore geometry with 0.1 m radius (Fig. 6.1). The reservoir rock is granite with properties listed in Table 6.1. The in-situ stress state is given by 30 MPa maximum horizontal stress in the x-direction and 20 MPa in the y-direction for minimum horizontal stress. Heterogeneous simulation was carried out using Weibull distribution functions for elastic modulus and permeability distributions. We assumed that the rock properties follow the Weibull distribution function in which the shape of the heterogeneities are n=2.0 for modulus and permeability, respectively. The same values are used for the tensile and cohesive strength distributions. The initial pore pressure is 10 MPa and wellbore pressure increased 5 MPa every 0.5 hr until it reached 30 MPa.

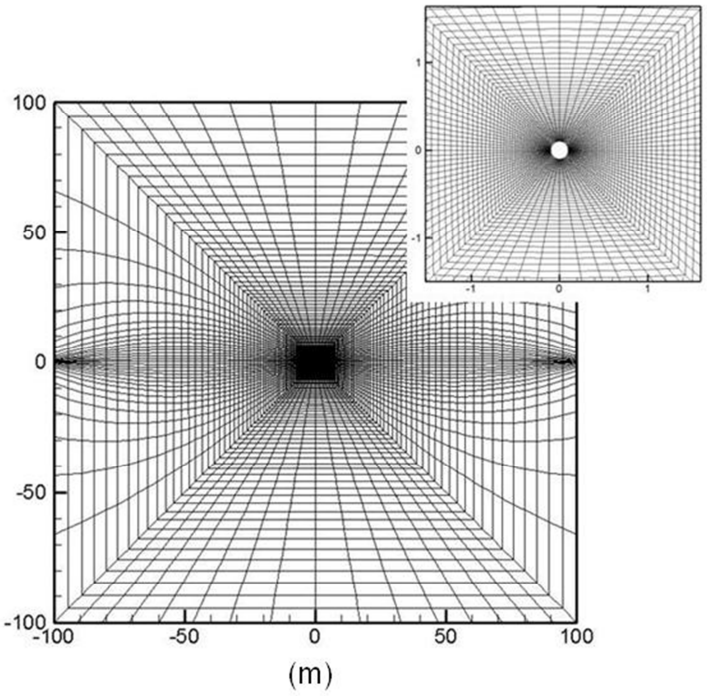

Fig. 6.1. Mesh used in damage evolution test with thermo-poro-mechanical simulations.

Table 6.1
Input material properties for granite.

Young's modulus E (GPa)	10
Drained Possoin's ratio υ	0.25
Undrained Possoin's ratio υ_u	0.33
Biot's coefficient, α	0.44
Permeability, $k_{H,\max}$ (md)	0.01
Permeability, $k_{H,\min}$ (md)	0.001
Fluid mass density, ρ_f (kg/m^3)	1111.11
Fluid viscosity, μ (Pa·s)	1×10^{-3}
Thermal expansion coefficient of solid, α_m (K^{-1})	2.4×10^{-5}
Thermal expansion coefficient of fluid, α_f (K^{-1})	2.1×10^{-5}
Thermal diffusivity, c^T (m^2/s)	2.0×10^{-6}
Porosity, ϕ	0.01

The simulation results are shown in Figs. 6.2 and 6.3. Injection-induced rock failure occurred around the wellbore and propagated out into the rock as shown in Fig. 6.2. In this simulation, we considered an initially anisotropic permeability distribution in the rock, and so the fluid flow in the damaged area is mostly focused in the direction of maximum permeability. Note that the far-field stress influences damage propagation significantly in this coupled fluid injection analysis. The far-field stress anisotropy around a wellbore contributes to tensile stress in the maximum far-field stress direction and causes compressive stress in the minimum far-field stress direction. Also, fluid injection causes tensile hoop stresses. Therefore, both anisotropic far-field stress and fluid-induced stress lead to tensile failure propagation in the maximum far-field stress direction. The simulated micro-seismic events are plotted in Fig. 6.3. We assumed that seismic events are checked in each Gaussian point and events occurred when the rock failed. These widely scatted events are observed in an early time step because of the initial failure. The injection-induced localized seismic events propagate into the rock with the passage of time.

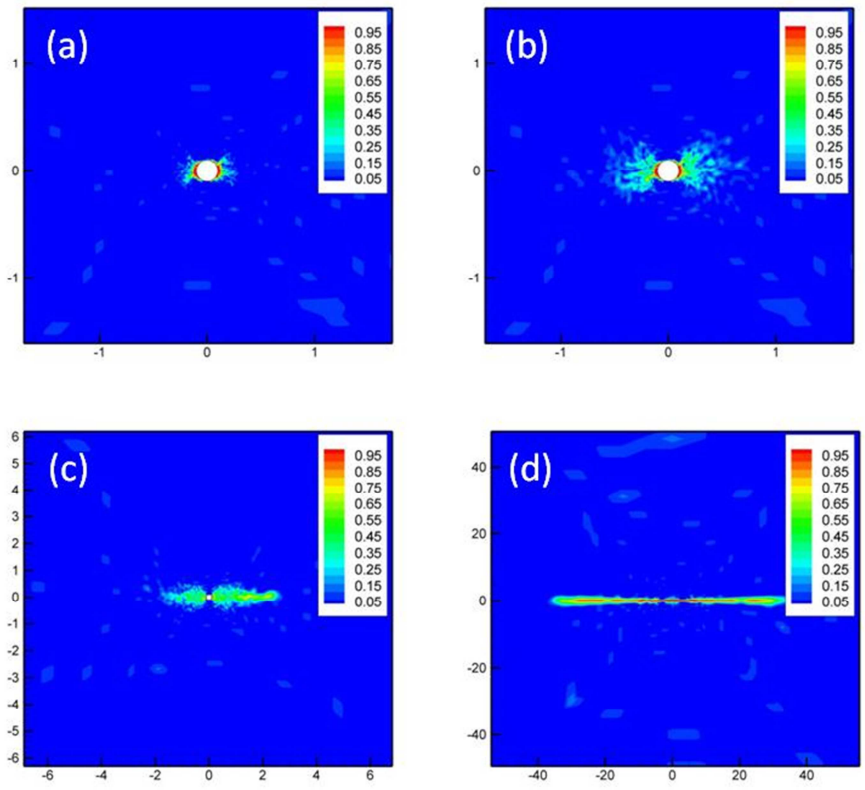

Fig. 6.2. Damage propagation with time; (a): 1 hr, (b): 3 hr, (c): 6 hr, and (d): 12 hr.

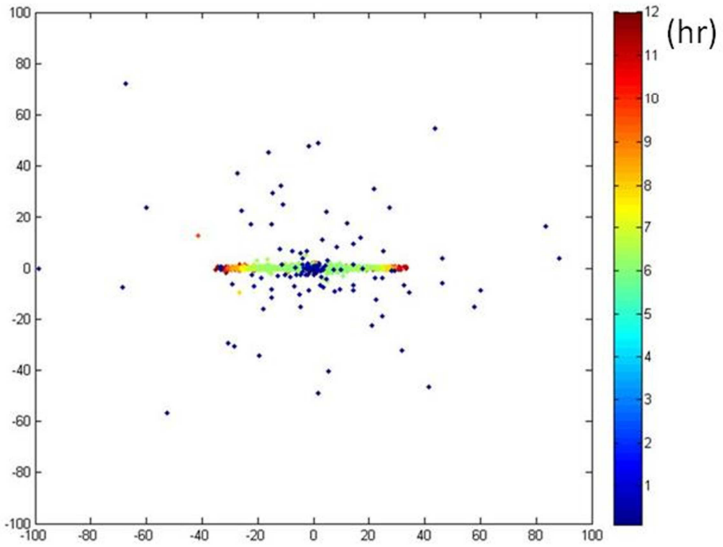

Fig. 6.3. Results of two-dimensional seismic events plot with time.

6.2 Point source injection and microseismicity

We next applied two-dimensional point source injection for large reservoir simulation using quadrilateral regular mesh and anisotropic far-field stress distributions with 10,000 elements and reservoir size of 1 km × 1 km. Injection rate boundary conditions were applied to the point source element while injecting with step increases from 0.1 $m^3/m^3 \cdot s$ to 0.15 $m^3/m^3 \cdot s$. Maximum and minimum far-field stresses are 30 MPa and 20 MPa, and initial pore pressure is 15 MPa. Physical parameters for the granite reservoir we used in this simulation are described in Table 6.1. Fig. 6.4 represents the failure propagation in the homogeneous modulus and permeability to the maximum far-field stress direction with respect to time when fluid is moving from the point source to the reservoir. Results show that fluid injection induces the effective stress change where

fluid contacts the area and causes tensile failure propagation in the maximum far-field stress direction. Injection-induced effective stress variations (σ_{xx}, σ_{yy}) are plotted in Fig. 6.5. In this study, rock failure propagated horizontally to tensile failure, which is similar to the previous well stimulation simulation. This horizontal propagation can be explained by the interaction of fluid with the rock skeleton that altered the modulus, and increased permeability created the stress relaxation in the damage area and amplification of stress distributions at the interface.

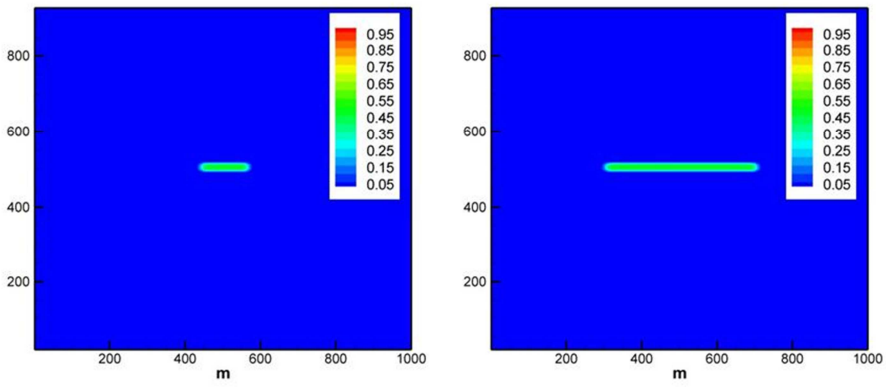

Fig. 6.4. Fluid induced damage (rock failure) distributions at 3 hrs and 12 hrs.

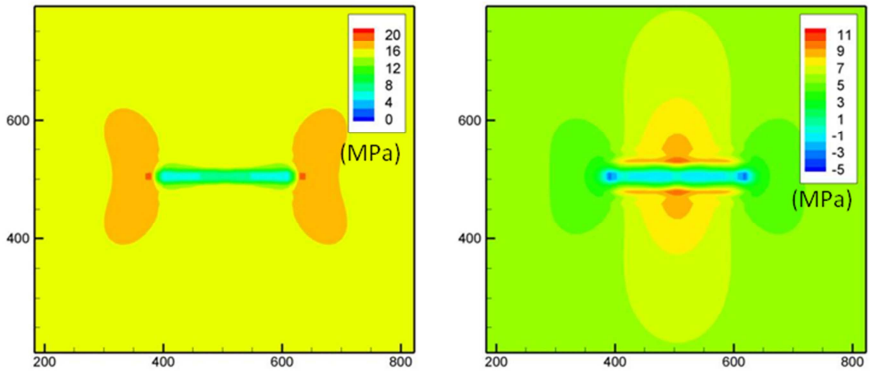

Fig. 6.5. Effective stress distribution of x (σ_{xx}) and y-direction (σ_{yy}).

Heterogenous properties for modulus and permeability have been applied to depict more realistic simulations. We assumed that physical properties have Weibull distribution functions and seismic events are triggered when the rock stress reaches the Mohr-Coulomb failure criterion with fluid injection. Initial modulus and permeability distributions are illustrated in Fig. 6.6. We used n=2 for controlling the degree of heterogeneity in Weibull distribution functions. Initial modulus distributions varied from 2 GPa to 18 GPa with mean values of 10 GPa and the average of initial permeability was 0.01 md with a range of 0.002 ~ 0.02 md as shown in Fig. 6.6.

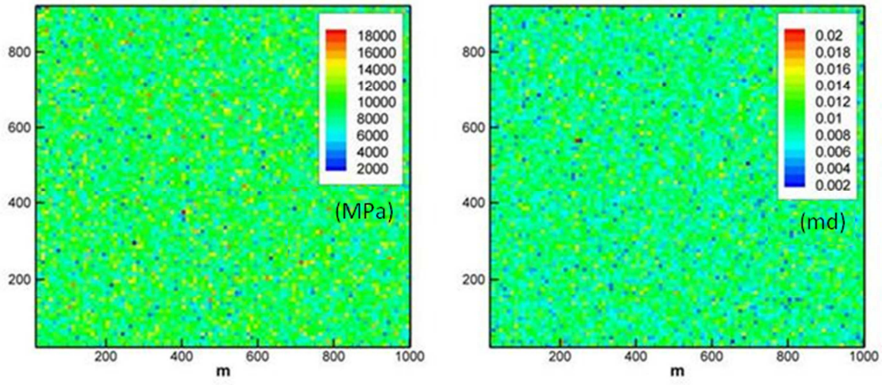

Fig. 6.6. Initial modulus and permeability distribution. The range of modulus is 2 GPa ~ 18 GPa and permeability is 0.002 ~ 0.02 md.

Results show that the damage by injection-induced rock failure propagates to the maximum far-field stress distribution; however, heterogeneity creates deviations of damage propagation caused by shear and tensile failure (Fig. 6.7). Pore pressure distributions are localized because of the permeability increase in the damaged area (Fig. 6.8). One of the features in the thermo-hydro-mechanical process of injection simulation is the localization of pore pressure caused by the localized propagation of rock failure and permeability increase. The result in Fig. 6.9 shows the seismicity plots with respect to time. Small circles are initial rock failure caused by far-field stress and large circles represent fluid injection-induced shear and tensile failure with time.

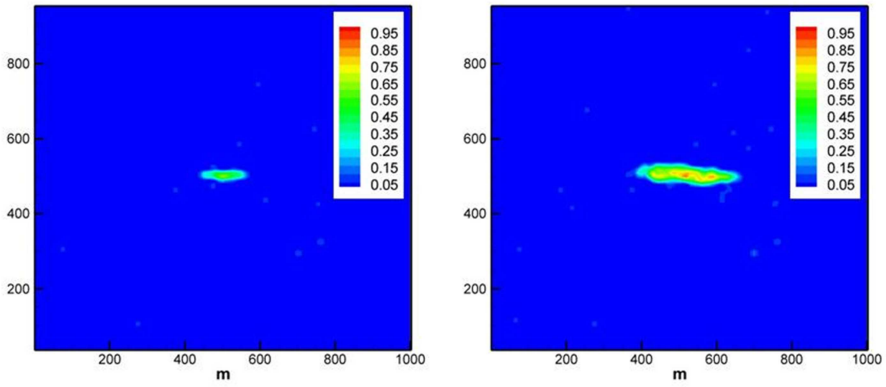

Fig. 6.7. Damage distributions at 3 hrs and 12 hrs in the heterogeneous case.

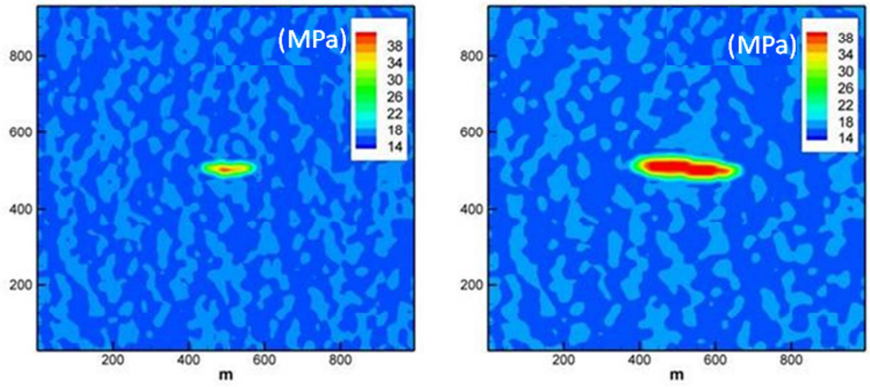

Fig. 6.8. Pore pressure distributions at 3 hrs and 12 hrs in the heterogeneous case.

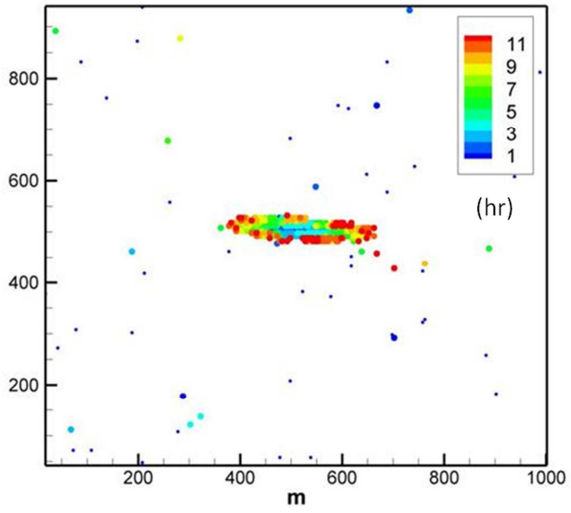

Fig. 6.9. Results for microseismic event propagation by fluid injection with time. The small circle is the initial rock failure by far-field stress and the large circle represents injection-induced triggering of microseismic events.

6.3 Discussion

Thermo-poroelastic modeling for microseismic event propagations with damage mechanics and the stress-dependent permeability model are presented in this section. Previous work from Shapiro (1997; 1999; 2002) for microseismicity modeling was developed from the fluid flow equation and criticality. He introduced concept of criticality values for pore pressure, assuming that microseismic events occurred if the pore pressure exceeded a certain value of criticality. This approach is reasonable from a certain point of view, because usually high pore pressure is needed to trigger rock failure. Shapiro's approach also has limitations in that it takes no consideration of permeability change, localization of stress distribution, or temperature effects in microseismic event

modeling. Fig. 6.10 illustrates the simulation results for induced microseismicity with critical pressure and rock failure criteria. We applied the same heterogeneity and injection schedule. Maximum far-field stress is to the x-direction and minimum far-field stress is to the y-direction. Results show that microseismic events propagate isotropically in critical pressure conditions, as opposed to the rock failure criterion. From the comparison, we conclude that the rock failure criterion can more effectively describe the ellipsoidal patterns from observation data. The main differences in this numerical simulation from Shapiro's model are the coupled impact of fluid flow, temperature, and stress change for the analysis of microseismic event propagation. The other improvement in this simulation is that permeability increases in the event locations, leading to the discontinuity of pore pressure and stress relaxations. In turn, it can explain the propagation of localized microseismic events in certain conditions. The influence of convective heat transfer is plotted in Fig. 6.11. Results show a larger region of cooling by permeability increase when we consider the convective heat transfer. The impact of convective heat transfer becomes important when the model considers fluid flow in fractures.

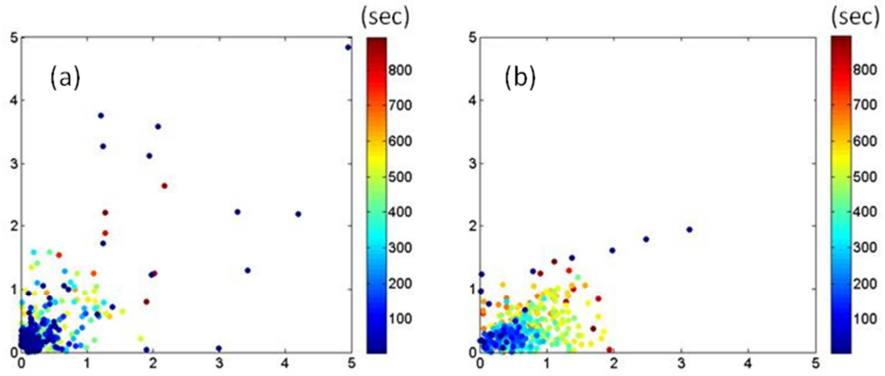

Fig. 6.10. Comparison of injection-induced microseimic event propagation under the same initial heterogeneity and injection schedule. Microseismic events based on critical pressure are plotted in (a), and rock failure criteria are plotted in (b).

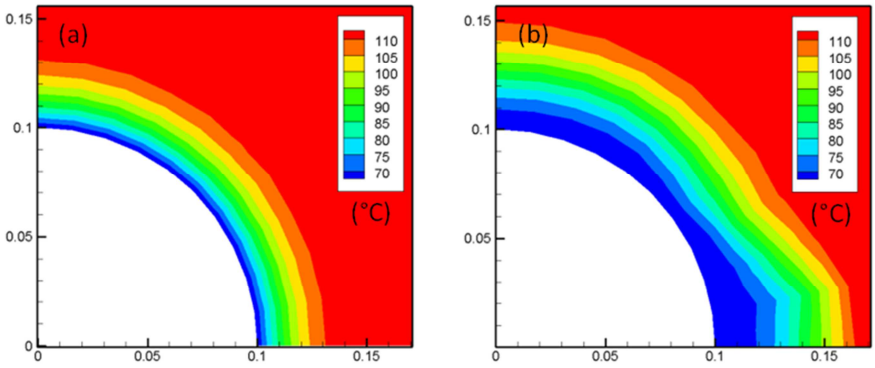

Fig. 6.11. Comparison of temperature distributions between conductive cooling and convective heat transfer in simulation of a sandstone reservoir which has 10 md for initial permeability and 100 md after rock failure. Only the conductive heat transfer case is plotted in (a) and convective with conductive heat transfer is plotted in (b). Both results are the snap shots at 180 sec.

6.4 Conclusions

Damage mechanics and the stress-dependent permeability model have been applied to fully-coupled thermo-poroelasticity. It is observed that effective stresses are relaxed in the damaged area and increased at the interface of the damaged and intact rock by the change of modulus and permeability with injection-induced rock failure. The model has been applied to the microseismic event simulation. Two types of injection schemes are used for geometrical well injection in small scale simulations and point source injection in large scale simulations. Results show distributed shear and tensile failure in the reservoir. The resulting rock failure and permeability enhancement is a function of the in-situ stress. Realistic patterns of micro-seismicity have been generated. Results show the significant roles of stress state and initial rock permeability in the resulting pattern. The results of this study indicate that the finite element method with damage can be used to model reservoir stimulation and induced seismicity.

7. THREE-DIMENSIONAL FINITE ELEMENT MODELING OF THERMO-PORO-MECHANICAL WELL STIMULATION AND INJECTION-INDUCED MICROSEISMICITY

The study of stress variations by fluid injection is important in enhanced geothermal reservoir (EGS). Especially near the wellbore, there is a significant change of stresses by temperature, fluid flow and far-field stresses. The influence of fluid flow and porous rock has been developed by Biot (Biot, 1941; Cryer, 1963), and its extension version of thermo-poroelasticity has been proposed (McTigue, 1986; Kurashige, 1995; Wang and Papamichos, 1994). They showed that the impact of thermo-poroelasticity around a wellbore that thermally-induced pore pressure distribution is significant if the rock permeability is low. The influence of chemical potential also has been developed that considered the influence of chemical potential, temperature and fluid flow in shale (Heidug and Wong, 1996; Ghassemi and Diek, 2003; Ghassemi et al., 2009). Most of the geothermal reservoir rock is granite so that we should consider the low permeable and brittle rock with cold water injection. Thermo-poroelasticity can be used to assess the influence of temperature and fluid flow change on the stress variations; however, there are some limitations that the rock skeleton is assumed to be elastic and constant permeability in fluid flow. Generally, the modulus and permeability are changed if the rock reaches the failure criterion. The strain-stress behavior in triaxial test shows hardening and softening after post-peak stress. This behavior depends on the rock type, pore pressure, stress condition and temperature (Jaeger, Cook, and Zimmerman, 2007).

Experimental results for permeability variation with stress also have been studied by many researchers (Shipping et al., 1994; Kiyama et al.; 1996, Coste et al., 2001; Zoback and Byerlee, 1975). Their experimental results for tests conducted on granite show permeability increase by a factor of four. Other studies present different magnitudes for the increase in permeability depending on rock type and conditions (De Paola et al. 2009; Wang and Park, 2002).

Continuum damage mechanics is used to consider the crack initiation, void growth, and crack propagation that can capture the hardening and softening behavior of a rock. Continuum damage mechanics was first introduced by Kachanov and since has been developed and applied by many researchers (Kachanov, 1958; Mazars, 1986; Simankin and Ghassemi, 2005; Tang et al., 2002; Li et al., 2005; Selvadurai, 2004). It can be contrasted with fracture mechanics in that damage mechanics describes crack initiation, microcracks, void growth, and crack propagation based on the failure criterion, whereas fracture mechanics assumes an initial crack for propagation. The impact of damage mechanics has been applied in the presence of poroelasticity. Selvadurai (2004) studied damage in poroelastic consolidation problems with a stress-dependent permeability model. His results showed a significant permeability alteration caused by damage evolution in consolidation problems. Hamiel et al. (2005) developed a model with time dependent damage variable, porosity, and material properties. They proposed different rock behavior with degradation and healing within the framework of the poroelastic theory. Tang et al. (2002) proposed a brittle damage and permeability model based on experimental strain-stress observations and permeability measurements (Tang

et al., 2002; Li et al., 2005). The model was implemented in a finite element model and was used to simulate a uniaxial compression test and hydraulic fracture propagation.

Damage mechanics has an advantage of considering the microfracture so that it can be one of the promising tools to predict injection-induced microseismic events. Microseismic event characteristics such as their locations, spatial patterns of distribution, and the temporal relation between seismicity and reservoir activities are often studied for enhanced geothermal systems (EGS). Microseismic event detection and interpretation is used for estimating the stimulated volume and fracture growth, resulting reservoir permeability, and geometry of the geological structures and the in-situ stress state (Pine, 1984). The process commonly is referred to as seismicity-based reservoir characterization. Although progress has been made in quantitative and qualitative analysis of reservoir stimulation using micro earthquakes (Shapiro et al., 1997; 1999; 2002; Rothert and Shapiro, 2003), the process of rock failure and permeability change has not been considered. In-situ stress and thermal effects on fluid-rock interaction have also not been considered.

In this work, we present the development of a three-dimensional (3D) finite element model to study the influence of thermo-poro-mechanical coupling on rock damage evolution and permeability variation with reference to reservoir stimulation and induced seismicity. The damage model we used corresponds to brittle rock failure with post-peak softening and permanent deformation prior to fracture. In order to capture the full effects of rock cooling by injection in the presence of higher fluid fluxes caused by rock failure and permeability enhancement, the model considers both the conductive and

convective heat transfer in porous media. A number of numerical simulations are presented to verify the model and to illustrate the role of far-field stress and permeability change in rock fractures, distributed damage evolution, and induced seismicity.

7.1 Injection-induced damage propagation

In this section, we present numerical examples for hydraulic fracturing experiments under the influence of different far-field stresses while taking into account fluid and temperature variations around a wellbore.

Before conducting large reservoir simulations, we tested a small simulation domain consisting of a 3D block of rock with dimensions of $10\times10\times5$ m^3 (Fig. 7.1) with a 0.2-m injection interval. We use an 8-noded hexahedron element for displacement and 8 nodes for pore pressure and temperature. All reservoir properties represented a granite reservoir (Table 6.1).

We compared the numerical solutions with analytical solutions for effective vertical stress distribution. We assumed zero far-field stress and pore pressure on the wall acting with 10 MPa along the vertical wellbore surface. The induced effective vertical stress component contributes to tensile stress since the pore pressure invasion to the reservoir leads the effective stress distribution from zero to the tensile stress as seen in Fig. 7.1. The plot in Fig. 7.2 compares the numerical solutions for effective vertical stress with analytical solutions with time. The comparison of pore pressure, total radial stress components, and total tangential stress components are presented in Figs. 7.3 to 7.5.

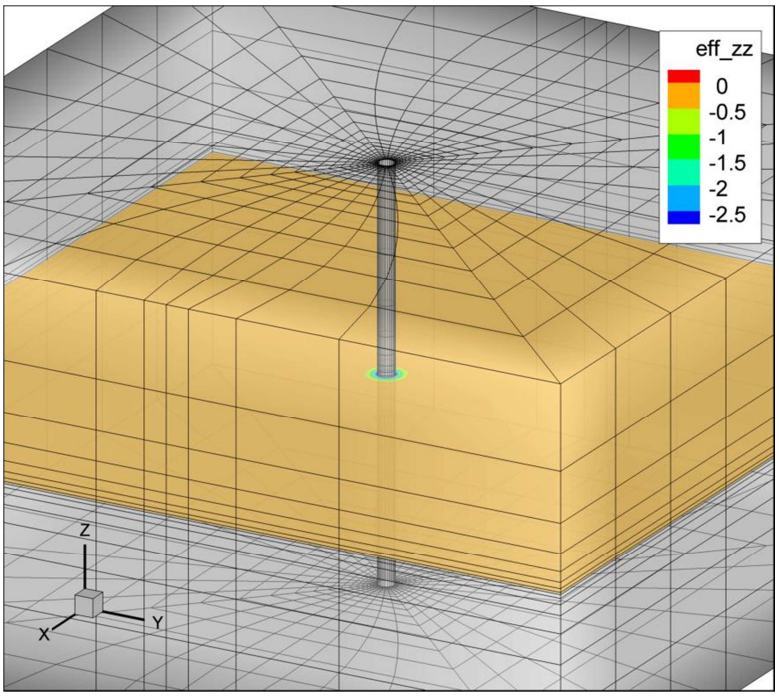

Fig. 7.1. Induced effective vertical stress variation by fluid injection.

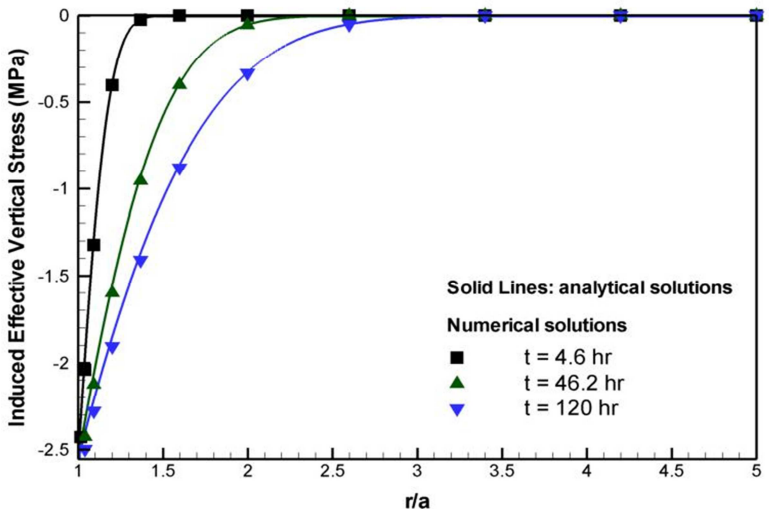

Fig. 7.2. Comparison of numerical solutions with analytical solutions for effective stress component, $\sigma'_{zz,}$, distribution.

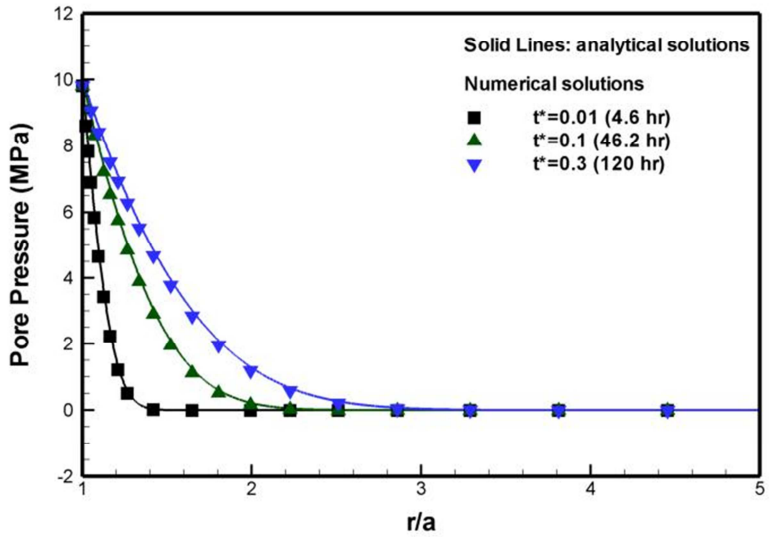

Fig. 7.3. Comparison of numerical solutions with analytical solutions for pore pressure distribution along to the radial direction.

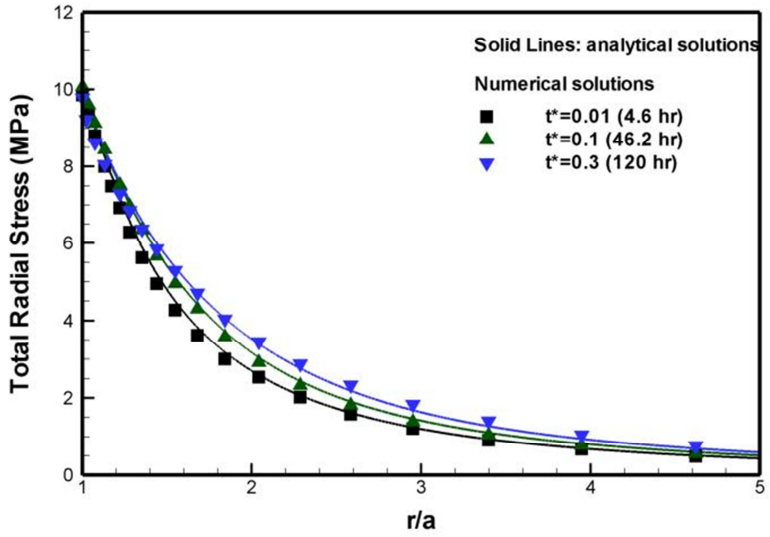

Fig. 7.4. Comparison of numerical solutions with analytical solutions for total radial stress, σ_{rr}, distribution.

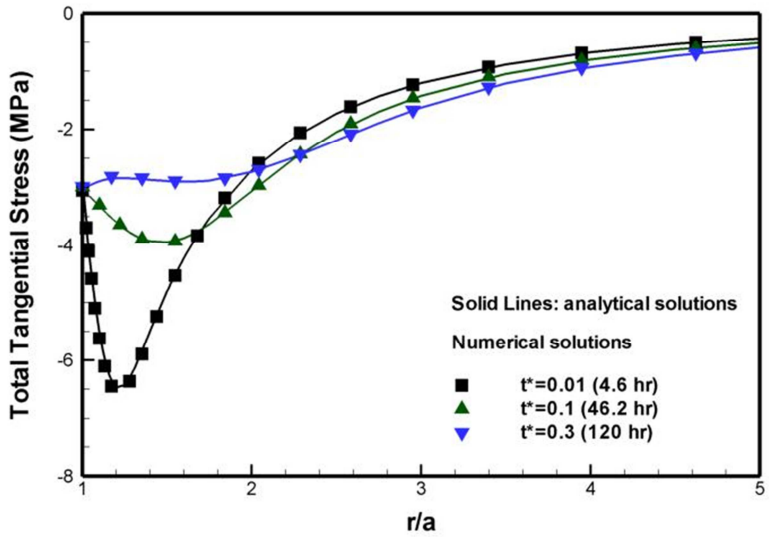

Fig. 7.5. Comparison of numerical solutions with analytical solutions for effective stress component, $\sigma_{\theta\theta}$, distribution.

For the analysis of injection-induced rock failure and permeability change, we assumed that permeability in the maximum far-field stress direction (x-direction) is 5 times higher than that in the minimum far-field stress direction (y-direction). The vertical permeability value is assumed to be 10% of the permeability in the minimum far-field stress direction. The experimental results for the permeability anisotropy showed that the permeability path is higher in the maximum stress direction (Khan and Teufel, 2000). In this example, the maximum horizontal stress is 30 MPa (x-direction), minimum horizontal stress is 20 MPa (y-direction), and the vertical stress is 10 MPa (z-direction). The injection pressure starts at 13 MPa and is increased at 0.5-hr intervals until it reaches 20 MPa.

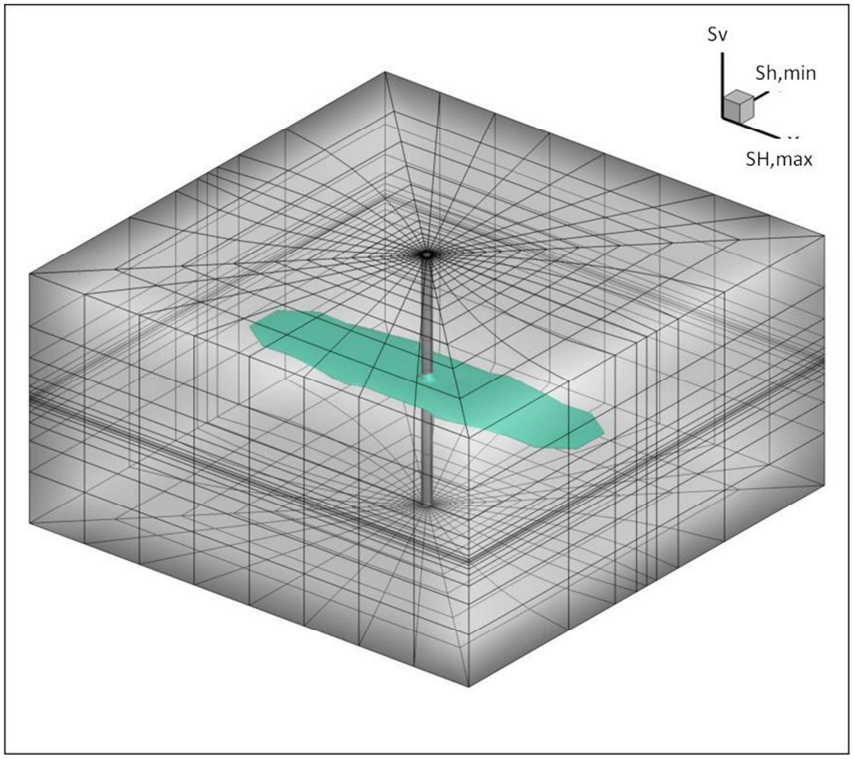

Fig. 7.6. Iso-surface (20%) of injection induced damage variable for the case when the minimum in-situ stress is S_v.

The iso-surface of the area damaged 20% by 6-hr fluid injection is plotted in Fig. 7.6. The permeability and pore pressure distributions in the fracture zone are represented in Fig. 7.7. Note that axial stress (σ_{zz}) distribution and horizontal tangential stress contribute to failure around the wellbore. In our fracture simulation, the damaged area (microcrack and void-growth area) becomes sharper when damage variable convergences are satisfied. Also, the anisotropic permeability model under anisotropic far-field stress shows more realistic results since fluid injection plays an important role in this process and its simulation.

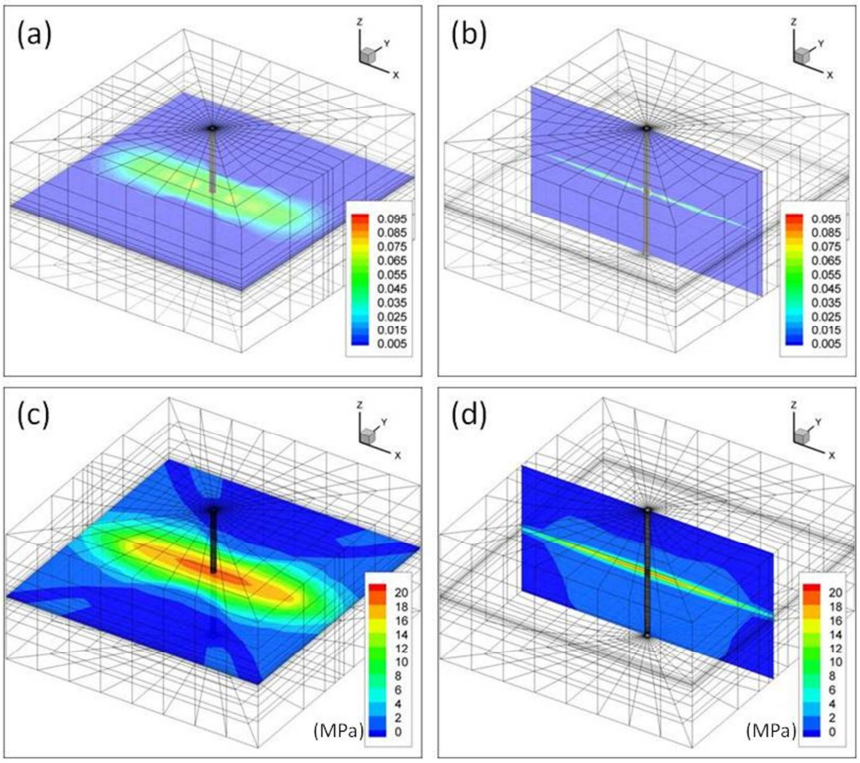

Fig. 7.7. Cross sectional view of permeability and pore pressure distributions. Results are for a time of 6 hrs. Permeability distributions: (a) and (b); pore pressure distributions: (c) and (d). See Table 7.1 for units. Unit for permeability is md.

7.2 Damage propagation under different stress regimes

After carrying out small reservoir geomechanical simulations, we conducted large scale reservoir simulations using a large mesh with 83,232 8-noded hexahedron elements for a reservoir size of 240×120 ×150 m^3 as shown in Fig. 7.8. We tested three different far-field stress regimes: strike-slip: ($S_{H,\max}$=30 MPa, $S_{h,\min}$=10 MPa, S_v=20 MPa), with horizontal far-field stresses as the maximum and minimum in-situ stresses; thrust ($S_{H,\max}$=30 MPa, $S_{h,\min}$=20 MPa, S_v=10 MPa), with vertical far-field stress as the

minimum stress component; and normal faulting ($S_{H,max}$=20 MPa, $S_{h,\,min}$=10 MPa, S_v=30 MPa), with the vertical far-field stress as the maximum in-situ stress component. All reservoir properties are the same as the previous simulations, and permeability anisotropy is oriented according to the far-field stress direction; for example, $k_{h,\,min}=0.1\times10^{-3}$ md, $k_{H,\,max}=10\times10^{-3}$ md, and $k_v=0.1\times10^{-3}$ md are applied for the strike-slip regime, $k_{h,\,min}=1\times10^{-3}$ md, $k_{H,\,max}=10\times10^{-3}$ md, and $k_v=0.1\times10^{-3}$ md for the thrust regime, and $k_{h,\,min}=0.1\times10^{-3}$ md, $k_{H,\,max}=1.0\times10^{-3}$ md, and $k_v = 0.1\times10^{-3}$ md are applied for the normal fault regime.

Table 7.1
Reservoir properties used in the simulations.

	Case 1 (Strike-Slip)	Case 2 (Thrust)	Case 3 (Normal)
$S_{H,\,max}$	30 MPa	30 MPa	20 MPa
$S_{h,\,min}$	10 MPa	20 MPa	10 MPa
S_v	20 MPa	10 MPa	30 MPa
$k_{H,\,max}$ (md)	10×10^{-3}	10×10^{-3}	0.1×10^{-3}
$k_{h,\,min}$ (md)	1×10^{-3}	1×10^{-3}	1×10^{-3}
k_v (md)	0.1×10^{-3}	0.1×10^{-3}	0.1×10^{-3}

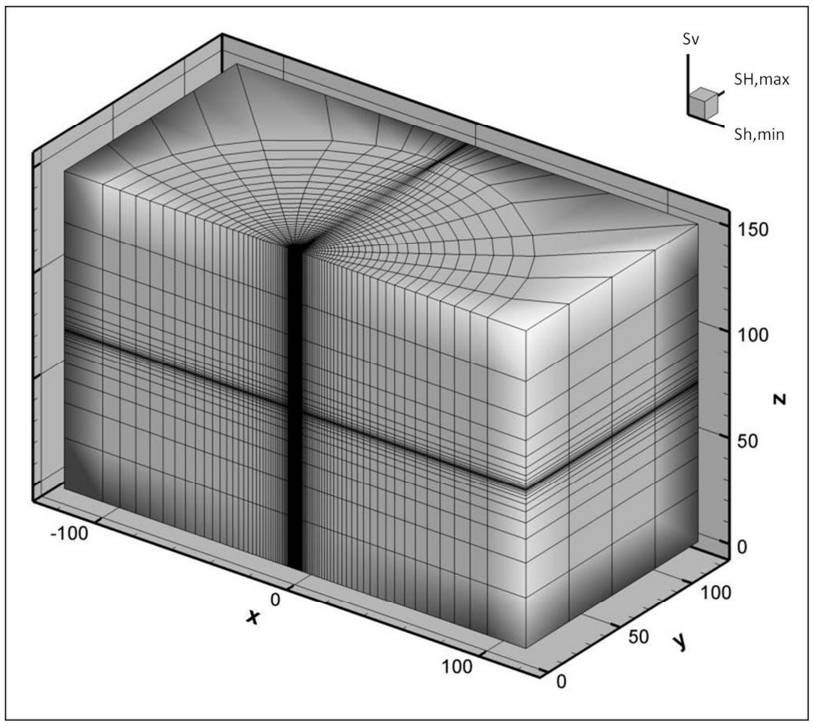

Fig. 7.8. Mesh used in simulation; $S_{H,\max}$ represents maximum horizontal stress, $S_{h,\min}$ is minimum horizontal stress, and S_v is vertical stress.

In these simulations, damage propagation caused by fluid injection was investigated in relation to the in-situ stress regime. The first case was when the minimum in-situ stress is horizontal (Case 1). The injection interval zone is 2 m and injection pressure begins at 8 MPa and is increased at 2.5 MPa increments every 0.5 hr until it reaches 32 MPa. Fluid injection causes both effective tangential and effective axial stresses to become tensile. These two stress components contribute to tensile principal stress inside the rock. Fig. 7.9 shows the 20% damaged area. Note that damage and fractures propagate vertically and horizontally in this case where the minimum stress is horizontal. Height growth occurs rapidly near the wellbore where the axial stress effects

dominate. Away from the wellbore, the in-situ stress controls the manner of damage zone propagation similar to a hydraulic fracture. The effective axial stress and pore pressure distributions are shown in Fig. 7.10.

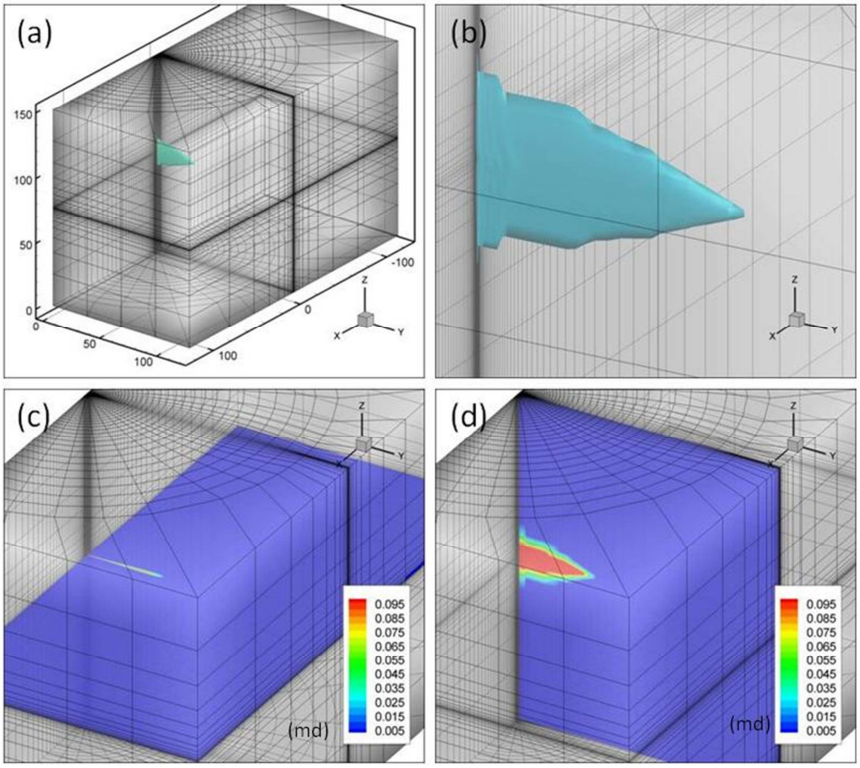

Fig. 7.9. Damage and permeability distributions for minimum horizontal far-field stress at 12 hrs. 20 % damage of iso-surface is plotted in (a), and (b) is a magnified image. Cross-sectional views of permeability distributions are illustrated in (c) and (d).

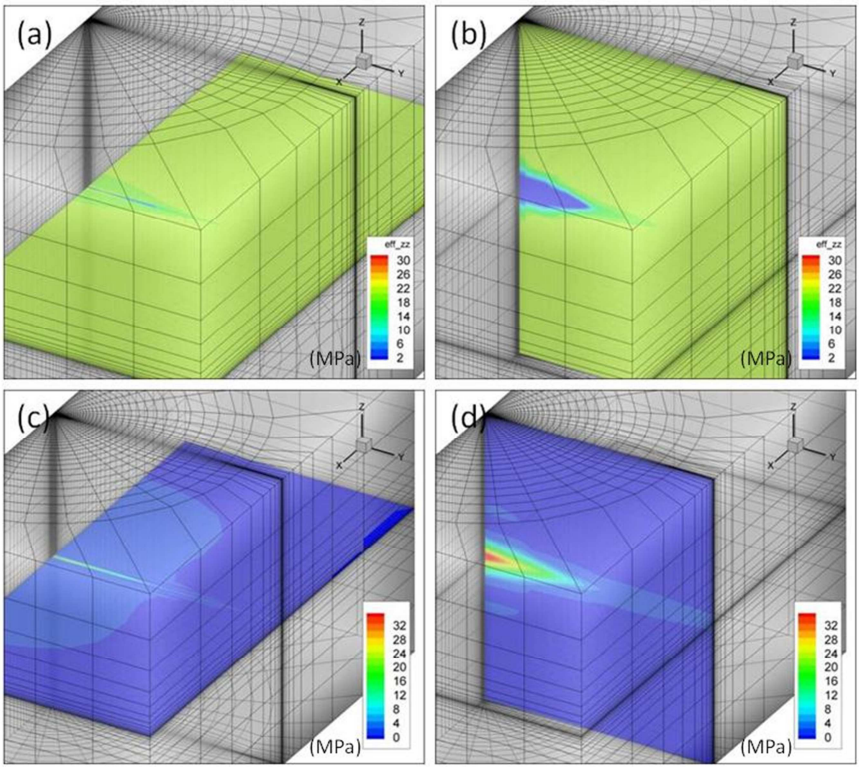

Fig. 7.10. Effective vertical stress and pore pressure distributions for minimum horizontal far-field stress at 12 hrs. Cross-sectional views of effective vertical stress are in (a) and (b), and pore pressure distributions are in (c) and (d), respectively.

For Case 2, the vertical minimum in-situ stress regime, the injection interval zone is 0.2 m and the pressure begins at 20 MPa and increases at 2.5 MPa at 0.5 hr until it reaches 42 MPa. Fig. 7.11 shows the fluid- induced 20% damaged area and the permeability distribution. Results show that injection-induced damage and the fractured area propagate horizontally. The propagation of damage is much larger in the maximum horizontal far-field stress direction than in the minimum horizontal far-field stress direction, which is influenced by permeability anisotropy.

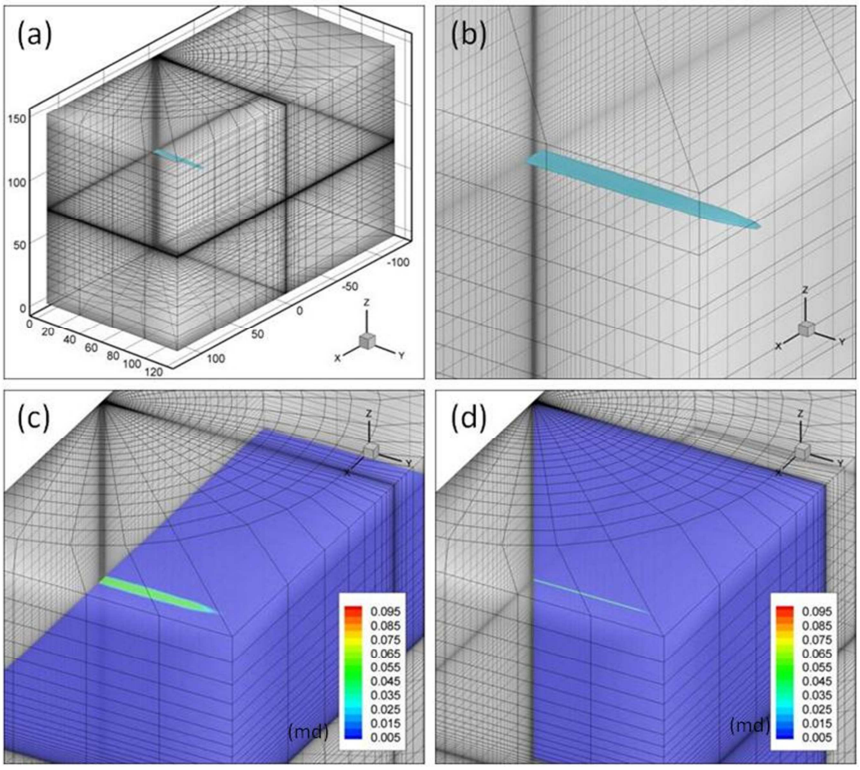

Fig. 7.11. Damage and permeability distributions for minimum vertical far-field stress at 6 hrs. 20 % damage of iso-surface is plotted in (a) and (b) is magnified image. Cross-sectional view of permeability distributions are illustrated in (c) and (d).

For the Case 3, vertical stress as the maximum far field stress, the same injection rate conditions of Case 1 are used for the comparison of the normal fault regime with the strike-slip regime (Case 1). The only different properties are far-field stress distribution and permeability anisotropy because maximum far-field stress directions are varied from the y-direction to the z-direction. Results show a stronger tendency for the induced damaged and fractured zone to propagate vertically; however, as shown in Fig 7.12, the damage area is smaller (for the same injection rate of Case 1) because of the influence of the large, vertical far-field stress.

The different geometry of the failure plane for the case of $S_{h,\min}$ and S_v as the minimum in-situ stress components can be attributed to different patterns of fluid and stress distribution in each case. In this simulation, the effective axial stress caused by fluid injection and deviatoric stress from the horizontal far-field stress are the main contributors to tensile failure across the wellbore for case 1 and case 3 ($S_{h,\min}$ as the minimum). However, in the case of S_v as the minimum stress, the effective axial stress is not significant compared to the minimum $S_{h,\min}$ and the wellbore hoop stress which serve to propagate the damage. We observe that a higher injection pressure is needed to generate the fracture plane in the homogeneous rock case, when *Sv* is the minimum in-situ stress rather than $S_{h,\min}$, because of the effective stress contributions for tensile failure. This is reasonable since there is additional hoop tensile stress (as opposed to only axial) when the fracture is initiated in a vertical plane.

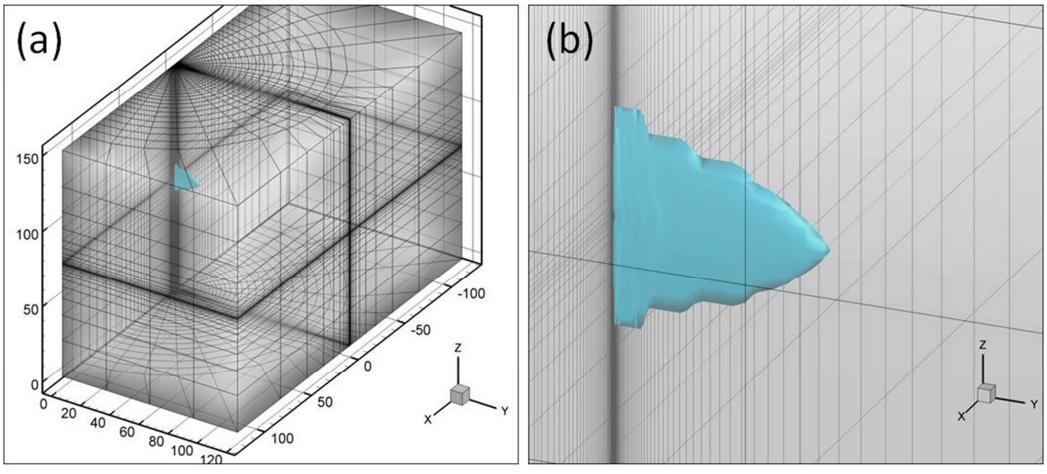

Fig. 7.12. Damage and permeability distributions for minimum vertical far-field stress at 6 hrs. 20 % damage of iso-surface

The variation of damage propagations with time for the strike-slip, thrust, and normal fault regimes are illustrated in Figs. 7.13 to 7.15 for comparison.

Hydraulic fracturing with cold water injection has been illustrated in Fig 7.16. Initial reservoir temperature is 200 °C and cold water temperature is 65 °C. Injection pressure is maintained 35 MPa for 6 hr, starting from 8 MPa. Both fluid injection and temperature difference contribute to fracture propagation. In this simulation, we assume the hydraulic fracture (macrocrack) as 90% damage. Results show that the 90% damage zone length is 24 m, height is 8 m, and average thickness near the well 10 cm. Note that temperature distribution is influenced by fluid flow, which is related with convective heat transfer, but the transfer rate is very slow. It is important to define the hydraulic fracturing in fluid injection. The main difference in the theory of fracture and damage mechanics is that the fracture considers macrocrack propagation, whereas damage mechanics considers the micro-fracture. Macrocrack propagation can be explained to be a sudden localization of microcracks (Mazars and Pijaudier-Cabor, 1996) so that the distributions of damage are generally broader than fracture propagations.

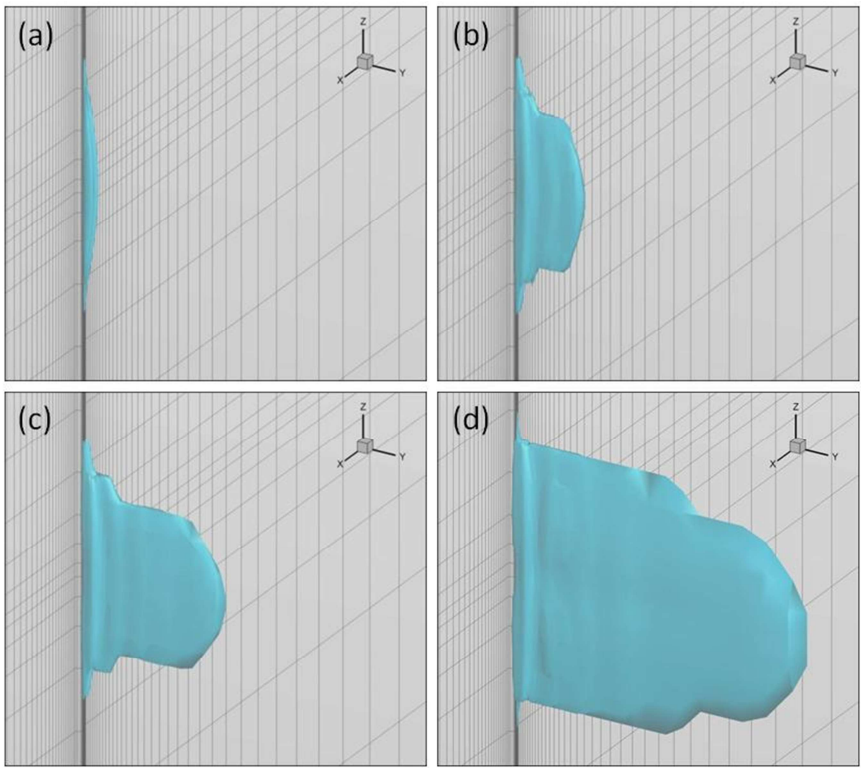

Fig. 7.13. Iso-surface 20% damage plot of 3D damage propagation with respect to time under horizontal far-field stress as the minimum: (a): 0.5hr, (b): 1 hr, (c): 1.2 hr, (d): 1.5 hr.

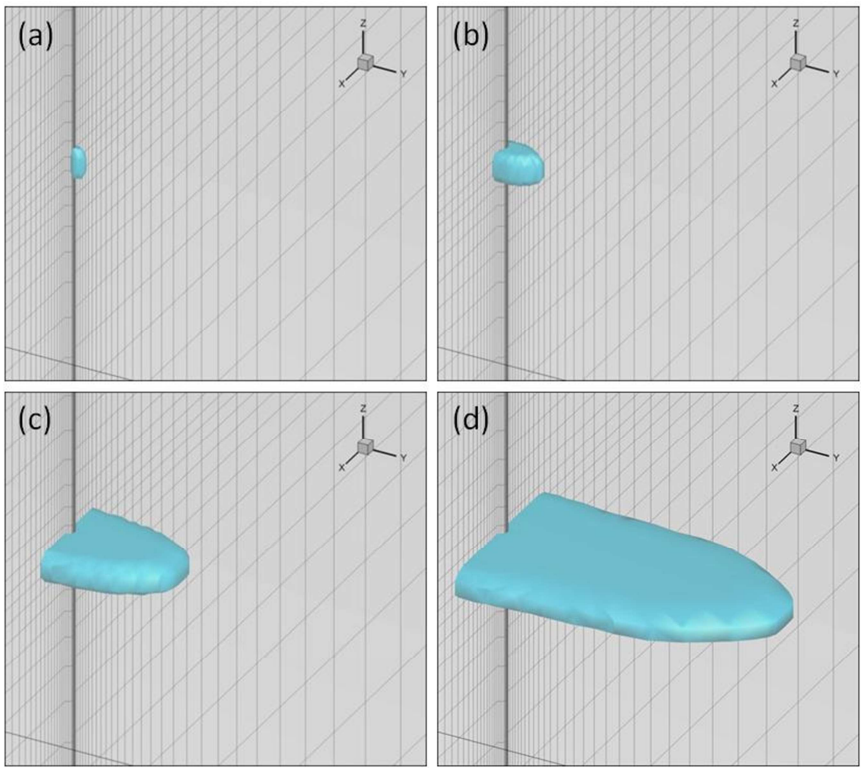

Fig. 7.14. Iso-surface 20% damage plot of 3D damage propagation with respect to time under vertical far-field stress as the minimum: (a): 1 hr, (b): 1.2 hr, (c): 1.5 hr, (d): 1.9 hr.

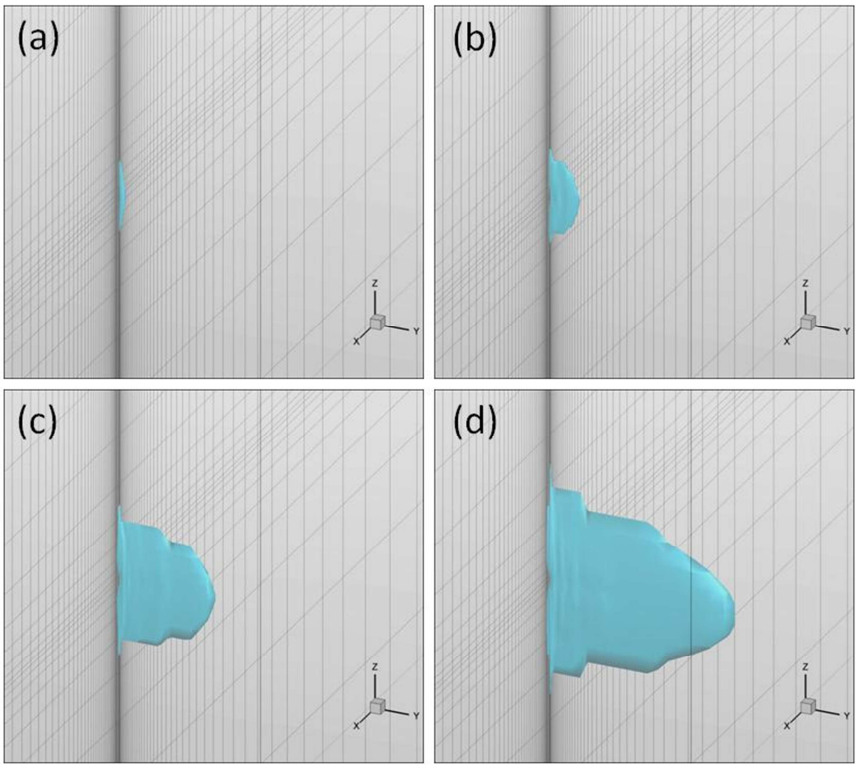

Fig. 7.15. Iso-surface 20% damage plot of 3D damage propagation with respect to time under vertical far-field stress as the maximum: (a): 1 hr, (b): 1.5 hr, (c): 2 hr, (d): 3 hr.

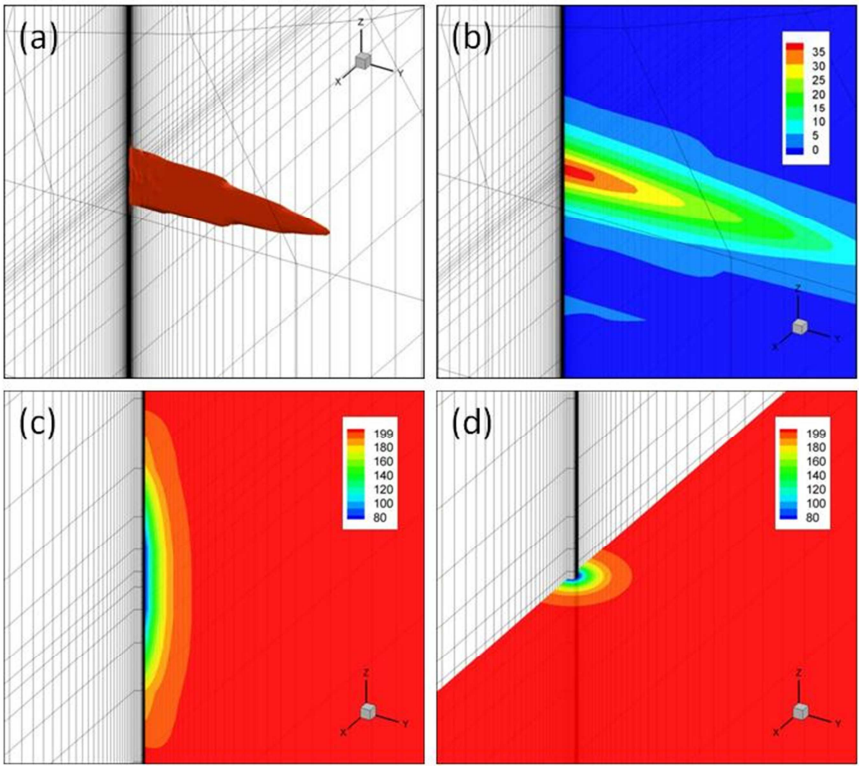

Fig. 7.16. Plot for hydraulic fracturing zone (90% damaged area) with minimum horizontal (a) and pore pressure distribution (b). Different plane views of temperature distributions in (c) and (d). All results have the same time step at 6 hr.

7.3 Injection volume analysis

The influence of injection volume under different stress regimes is reported in this section. Well pressure in this comparison is a step increase of 15 to about 44 MPa for normal regimes and 20 to about 48 MPa for thrust regimes. Initial well pressure is set to the pressure before the rock failure and damage evolution begins after the next step increase of wellbore pressure. Fig. 7.17 shows the comparison of a 40% damaged area with different far-field stresses when we inject 968 L for 3 days in the normal regime ($S_{H,}$

$_{max}$ = 20 MPa, $S_{h,\,min}$ = 10 MPa, S_v = 30 MPa, $k_{H,\,max}$ = 10×10^{-3} md, $k_{h,\,min}$ = 1×10^{-3} md, and k_v = 0.1×10^{-3}) and 340 L for 3 days in the thrust regime ($S_{H,\,max}$ = 30 MPa, $S_{h,\,min}$ = 20 MPa, S_v = 10 MPa, $k_{H,\,max}$ = 1×10^{-3} md, $k_{h,\,min}$ = 1×10^{-3} md, and k_v = 0.1×10^{-3} md). The normal regime led to a larger damaged area and higher injection volume than the thrust regime. This is because of the influence of the horizontal deviatoric stress to increase damage distribution with similar injection pressure schedules. Injection pressure is similar to the case of thrust regime, but tangential stress creates larger failure in the maximum far-field stress direction around a wellbore in the normal regime. However, in the thrust regime the contribution of tangential stress is weak and induced vertical stress cause it to fail. Results indicate that larger damage and injection volume can be predicted with the same injection pressure where the minimum far-field stress is horizontal than in the thrust regime. The thrust regime needs a higher injection pressure schedule to create a fracture plane with given far-field stress condition.

Damage distribution and injection volume have been studied in the same injection pressure schedule with different far-field stress (Fig. 7.18). The conditions for far-field stress and permeability are $S_{H,\,max}$ = 20 MPa, $S_{h,\,min}$ = 10 MPa, S_v = 30 MPa, $k_{H,\,max}$ = 10×10^{-3} md, $k_{h,\,min}$ = 1×10^{-3} md, k_v = 0.1×10^{-3} for the normal regime and $S_{H,\,max}$ = 40 MPa, $S_{h,\,min}$ = 20 MPa, S_v = 30 MPa, $k_{H,\,max}$ = 10×10^{-3} md, $k_{h,\,min}$ = 1×10^{-3} md, k_v = 0.1×10^{-3} for the strike-slip regime. The injection pressure is scheduled as step increases from 5 MPa to 32.5 MPa every 1 hr for both cases. Injection volume is 473 L with 3 day injection for the normal regime and 121 L also with 3 day injection for the strike-slip regime. Deviatoric stress for the strike-slip regime is 10 MPa, whereas it is

5 MPa for the normal regime. Larger damage and injection were observed in the normal-regime than in the strike-slip regime. Previous comparison shows the influence of deviatoric stress in damage distribution with the same initiation of rock failure. However, in this comparison, the failure beginning time is different in the normal and strike-slip regimes with same injection pressure schedule. Injection-induced damage propagation begins later in the strike-slip regime because of higher compressive horizontal stresses. This analysis shows that the roles of horizontal deviatoric stress and failure initiation pressure aare important to predict injection volume and fracture propagation. This analysis indicates that fracture propagation results from the complex interactions of the fluid injection pressure, far-field stress, permeability, and rock strength.

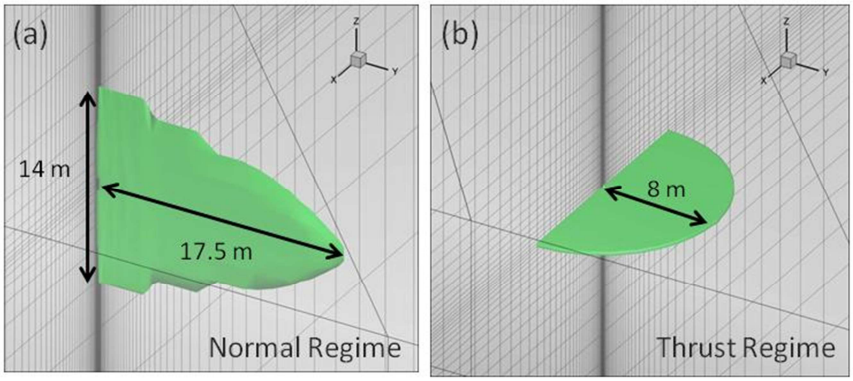

Fig. 7.17. The comparison of damage distribution under different stress regimes. (a) normal regime, 968 L for 3 days (b) thrust regime, 340 L for 3 days.

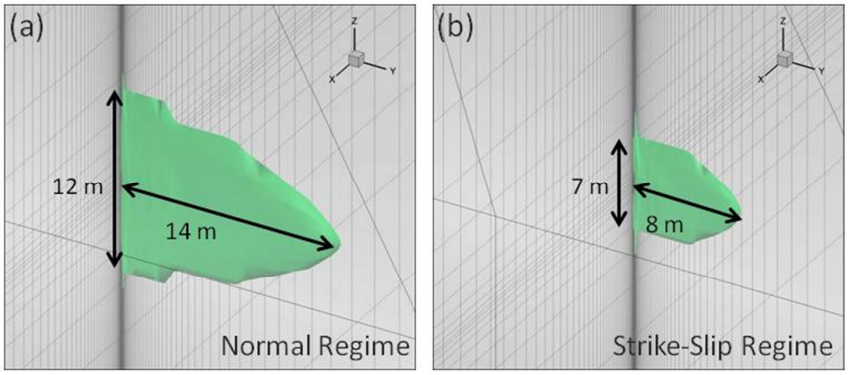

Fig. 7.18. The comparison of damage distribution under different stress regimes. (a) normal regime, 473 L for 3 days (b) strike-slip regime, 121 L for 3 days.

7.4 Heterogeneous microseismicity simulations

In this section, we consider induced microseismicity simulations with damage evolution. We assumed that seismic events are generated when the effective rock stress reaches the level prescribed by the failure criterion (Mohr-Coulomb) as fluid infiltrates the rock and stresses change. The simulation mesh is the same as in the previous homogeneous 3D simulations. However, heterogeneities of modulus and permeability are considered using Weibull distribution functions. The initial modulus and permeability distributions are illustrated in Fig. 7.19. As before, three different far-field stress regimes were tested: one with horizontal stress as the minimum, another with vertical stress as the minimum, and the other with vertical stress as the maximum. To investigate the permeability and far-field stress relationship, we also considered two different permeability models: (1) reservoir permeability properties are highly related to the far-field stress (anisotropic permeability), and (2) permeability is independent of the

far-field stress (isotropic permeability). Details of reservoir properties are described in Table 7.2. In the case of anisotropic permeability, we simply assumed a permeability that is 10 times higher in the maximum in-situ stress direction and 10 times lower in minimum in-situ stress direction.

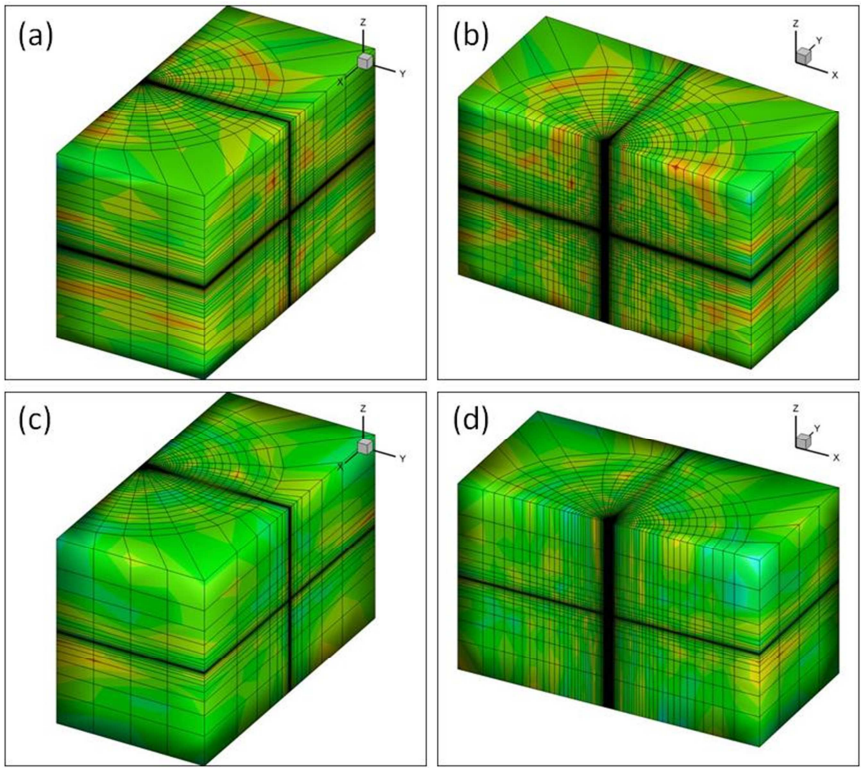

Fig. 7.19. Initial heterogeneous modulus which ranges from 4 GPa to 16 GPa in (a) and (b), and permeability distribution (0.004 to about 0.016 md) is presented in (c), (d).

Table 7.2.
Reservoir properties used in 3D heterogeneous simulations.

	Case 1	Case 2	Case 3	Case 4	Case 5	Case 6
Stress regime	Strike-slip		Thrust		Normal	
E	10 GPa (n=1.5)		10 GPa (n=1.5)		10 GPa (n=1.5)	
k, [md] (n=1.5)	10^{-2}	$k_{max}=10\times10^{-2}$ $k_{min}=0.1\times10^{-2}$ $k_v=1.0\times10^{-2}$	10^{-2}	$k_{max}=10\times10^{-2}$ $k_{min}=1.0\times10^{-2}$ $k_v=0.1\times10^{-2}$	10^{-2}	$k_{max}=1\times10^{-2}$ $k_{min}=0.1\times10^{-2}$ $k_v=10\times10^{-2}$
C_0	100 MPa (n=2)		100 MPa (n=2)		100 MPa (n=2)	
T_0	5 MPa (n=2)		5 MPa (n=2)		5 MPa (n=2)	

The resulting seismic events distributions are plotted in Figs. 7.20 to 7.22 for different reservoir permeabilities in different in-situ stress regimes. Fig. 7.20(a) shows the seismic events in time for the conditions of isotropic permeability with minimum horizontal far-field stress. Fig. 7.20(b) shows a plot for the same far-field stress conditions and injection rate but with anisotropic permeability. The seismic events are scattered broadly when permeability is isotropic since there are no significant differences in fluid sweep velocities in the x-, y-, and z-directions. However, in the case of anisotropic permeability, seismic events are highly localized because fluid invasion is focused in the maximum far-field stress direction, and this leads to localized seismic events. Same conditions are simulated for the minimum vertical far-field stress case (Fig. 7.21). Similarly, broad distributed seismic events occur under isotropic permeability conditions, and scattered localized events are observed in the anisotropic permeability case. Vertical stress as the maximum has been plotted in Fig. 7.22. Note that same

injection conditions are used for both stress regime simulations. Results show that for the normal faulting case, the induced seismicity does not propagate but stabilizes earlier because vertical stress is higher than the thrust regime, where a higher injection rate is needed to generate tensile failure for fracture propagation in the vertical direction. It is worth pointing out that the smaller gray points show the distribution of micro-seismic events as a result of the far-field stresses and might be interpreted as background values.

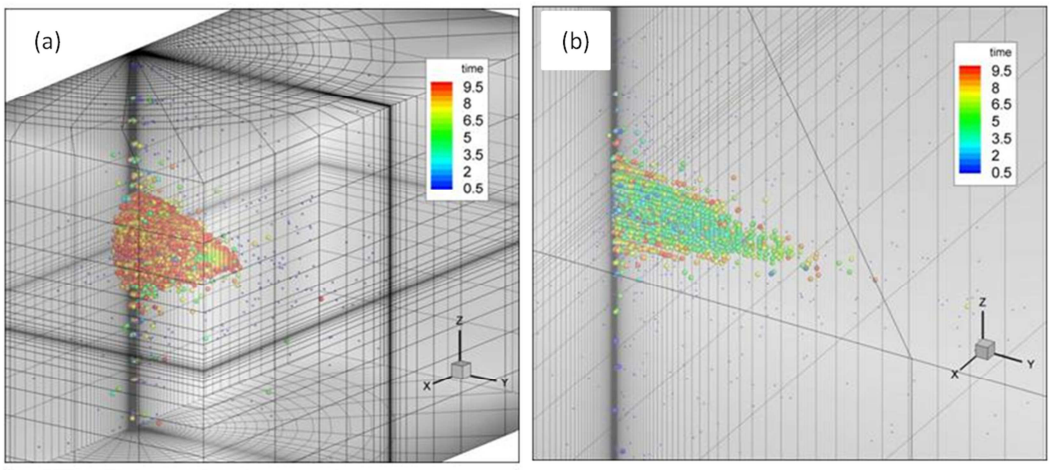

Fig. 7.20. Predicted micro-seismic events after 10 hrs of pumping for the case of horizontal stress as the minimum far-field stress: (a) isotropic permeability and (b) anisotropic permeability.

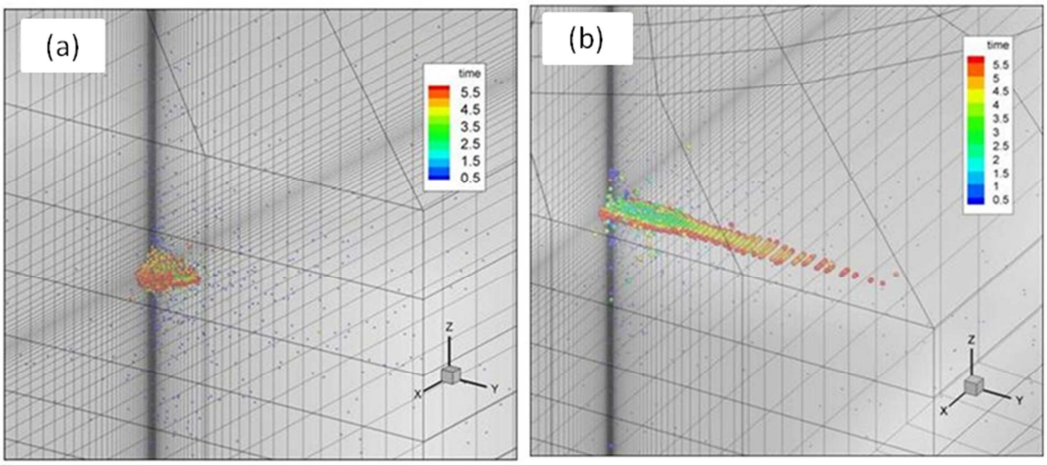

Fig. 7.21. Micro-seismic events after 6 hrs of pumping for the case that the vertical stress is the minimum far-field. (a) isotropic permeability and (b) anisotropic permeability.

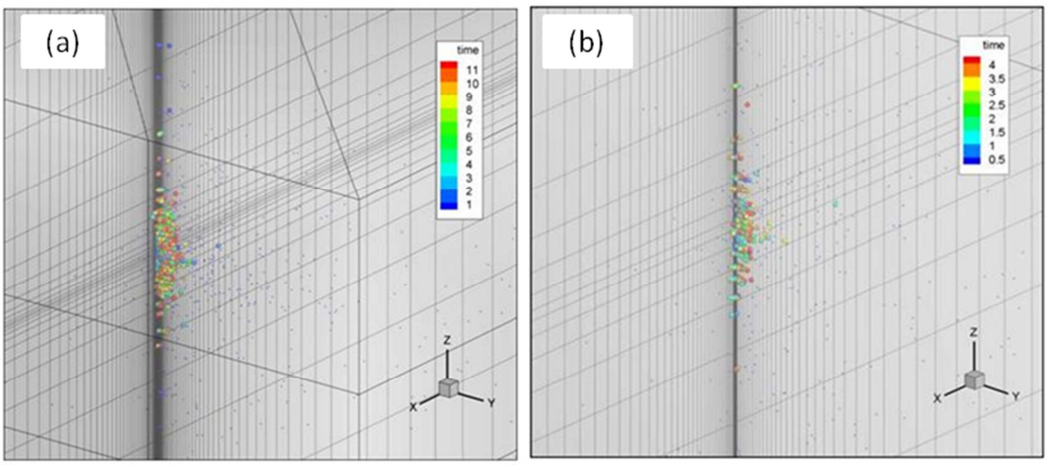

Fig. 7.22. Micro-seismic events after 6 hrs of pumping for the case that the vertical stress is the maximum far-field. (a) isotropic permeability and (b) anisotropic permeability.

The influence of cooling has been compared in Fig. 7.23. Initial reservoir temperature is assumed 200°C and injection cold water temperature is 50°C. The heat

transfer by conduction and convection between the fluid flow and hot reservoir causes tensile stress, which creates larger induced microseismic events. For the cooling case, the fluid contact in an early time step contributes significantly to tensile stress, resulting in larger failure than in the isothermal case. Results show that larger initial microseismic events occurred for the case of cooling [Fig. 7.23(a)] than in the isothermal condition [Fig. 7.23(b)]. Since the heat transfer rate is slower than fluid transport, the effects of thermal stress are important for the long-term fluid injection (3 to 12 months). However, the thermal stress also plays an important role in short-term fluid injection (3 to 6 days) to estimate the microseismic event propagation since the cooling that creates more tensile stress in an early time step on the wall of the wellbore results in larger rock failure with the same fluid injection.

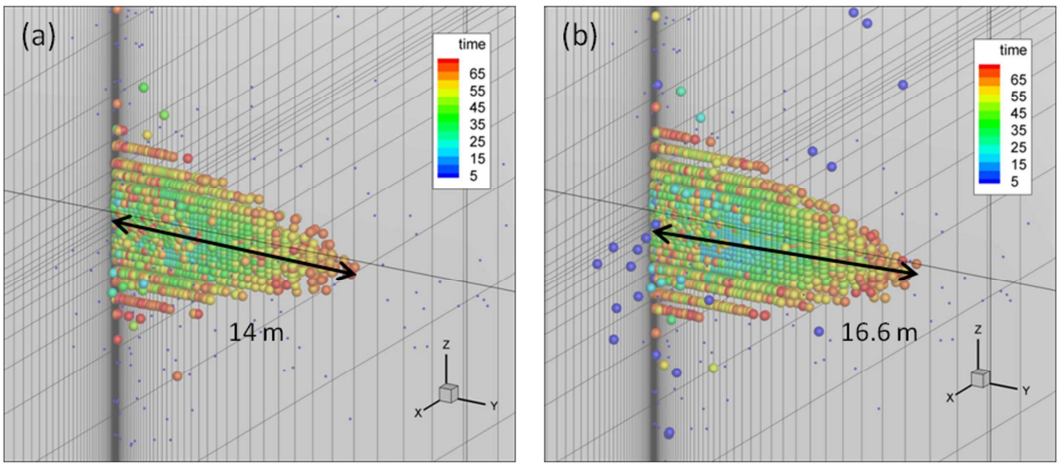

Fig. 7.23. Comparison of microseismic events after 65 hrs of pumping for the case of isothermal condition and cooling condition. (a) isothermal and (b) cold water (50°C) to the hot reservoir (200°C).

7.5 Conclusions

Damage mechanics and stress-dependent permeability models have been applied to injection induced stress variations in thermo-poroelasticity. The parameters for strain-stress and strain-permeability can be obtained by triaxial simulations comparing the experimental results. The modulus and permeability changes caused by rock failure influence the stress distributions, which in turn affect the impact of damage propagation. The results show that the failure plane is perpendicular to the minimum far-field stress distribution. Cold water injection in the normal or strike-slip regime shows penny-shape propagation which can capture the hydraulic fracturing. The study of injection volume indicates that the influence of far-field stress, injection pressure schedule, and fracture initiation pressure can be used to predict the drainage volume and fractured area related to fluid injection. We considered a heterogeneous modulus and permeability in microseismicity simulations and compared the effect of permeability anisotropy. The propagation of microseismic events is localized when the reservoir permeability is anisotropic because of fluid path localizations. The results of this study indicate that the finite element method with damage can be used to model reservoir stimulation and induced seismicity.

8. THREE-DIMENSIONAL THERMO-PORO-MECHANICAL ANALYSIS WITH POINT SOURCE FOR INDUCED MICROSEISMICITY

Three-dimensional injection induced damage/fracture propagation at well scalewas presented in the previous section. To simulate microseismic event propagation in larger space, it is efficient to consider the point source injection scheme because injection well radius (~0.1 m) is negligible compared to reservoir size. Point source is localized fluid and heat flux without geometry considerations for mathematical approximation to simplify the problem. The development of numerical implementation of the point source method was described in Section 3.1.3.

We performed three-dimensional (3D) simulation with point source fluid loading. We used an 8-node hexahedron element for displacement, pressure, and temperature, and the total element number used in this simulation is 32,000. Reservoir size is 1 km × 1 km × 0.5 km, and we assume that the depth of injection is 2.5 km and the injection interval is 25 m at the middle point of the reservoir (Fig. 8.1). We also considered gravitational force to the z-direction which has gradual change for vertical stress and maximum and minimum horizontal far-field stresses are constant to the vertical direction. Three different types of far-field stress regimes are studied with same injection rate to analyze the influence of far-field stresses as shown in Table 8.1. Newberry geothermal reservoir stress regimes are used for strike-slip and normal regime. For thrust regime, we tested Cooper basin geothermal reservoir stress regime. Initial reservoir properties for modulus and permeability are generated using Weibull distribution functions.

To apply gravity in the simulations, we used the measured reservoir data as initial pore pressure and far-field stress for initial background stresses that increase with depth. The other method to apply gravity in the simulation is by applying the force to the z-direction in each element on a basis of rock density data. We performed the simulations based on reservoir stress data. The progress of reservoir stress distribution during fluid injection can be computed by summing the induced stress variation and the background far-field stress field in each Gaussian point of the element.

Fig. 8.2 shows initial heterogeneity with average modulus of 10 GPa and average permeability of 0.01 md. The injection schedule and pressure changes are plotted in caused by rock failure and the propagation of the damaged area.

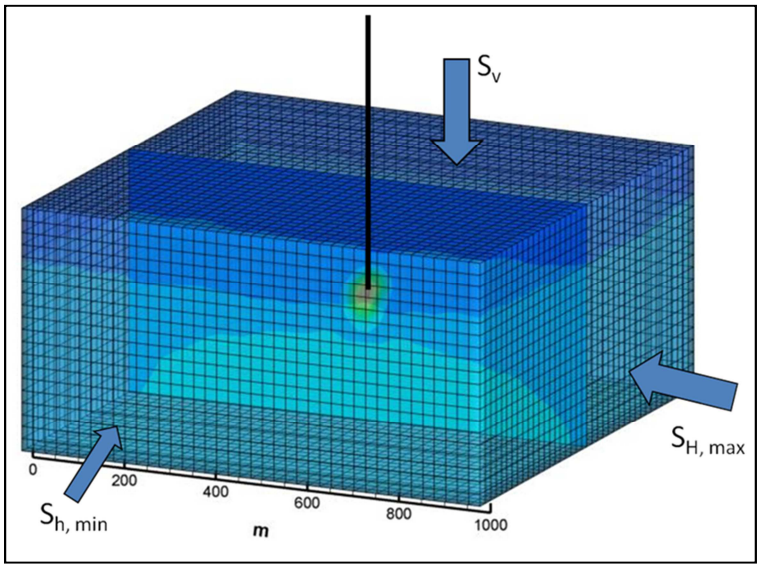

Fig. 8.1. Mesh used in three-dimensional simulation; $S_{H,\max}$ represents maximum horizontal stress, $S_{h,\min}$ is the minimum horizontal stress, and S_v is the vertical stress.

Table 8.1
Reservoir properties used in 3D simulations.

	Case 1 (Strike-slip)	Case 2 (Thrust)	Case 3 (Normal)
$S_{H,\,max}$	70 MPa	95 MPa	48 MPa
$S_{h,\,min}$	46 MPa	70 MPa	36 MP
S_v	60 MPa	60 MPa	60 MPa
$k_{H,\,max}$	1×10^{-2} md	1×10^{-2} md	1×10^{-2} md
$k_{h,min}$	1×10^{-2} md	1×10^{-2} md	1×10^{-2} md
k_v	0.1×10^{-2} md	0.1×10^{-2} md	0.1×10^{-2} md

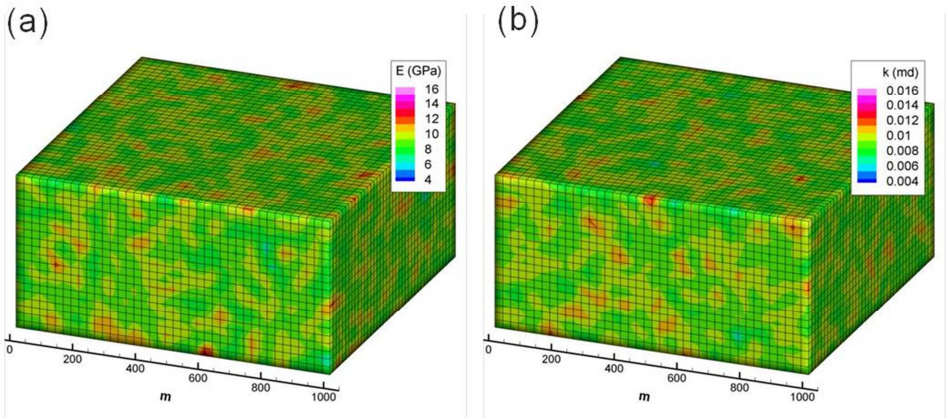

Fig. 8.2. Initial heterogeneous modulus (a) and permeability (b).

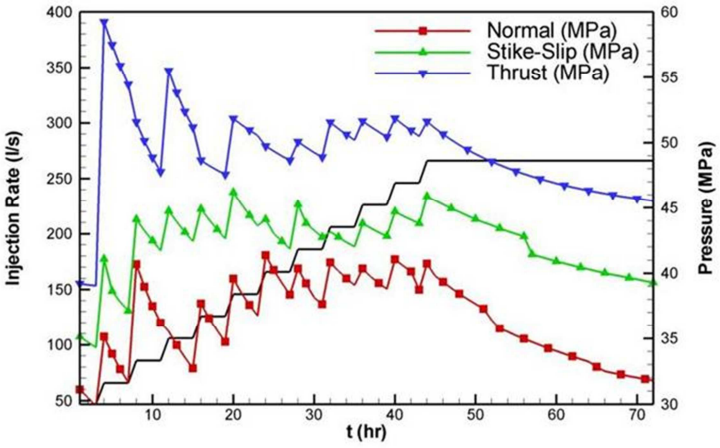

Fig. 8.3. Injection rate and injection pressure are plotted in normal, strike-slip, and thrust regime.

8.1 Microseismicity in strike-slip regime

Three-dimensional injection-induced stress and permeability change were performed under a strike-slip regime (horizontal far-field stresses are the maximum and the minimum, and vertical stress is intermediate) for a Newberry geothermal reservoir. Fig. 8.4 describes the injection-induced microseismic events with respect to time. We assumed that microseismic events occurred if the effective rock stresses reached the shear or tensile failure criterion. Change of color represents the time scale from the initial time step to 72 hrs. Results show that seismic events are propagated irregularly because of the heterogeneity from fluid injection, but a cross-sectional view shows that the seismic event propagation follows the maximum horizontal stress direction as shown in Fig. 8.5. The different mode of rock failure is plotted in Fig. 8.6, where the red

denotes the shear failure and the blue is tensile failure caused by the stimulation. The distributions of S1-S3 (maximum principal stress – minimum principal stress) and minimum far-field stress distributions are plotted in Fig. 8.7 and Fig. 8.8. The stress distribution along the vertical direction increases as the depth increases because of the gravity in the far-field stress. The results of stress distribution show that fluid injection decreases the effective stress level, which results in shear and tensile failure and stress relaxation at the microseismic event location. Pore pressure distributions are plotted for 1-hr and 3-day stimulations in Fig. 8.9; it dispersed nonhomogeneously due to the heterogeneous permeability.

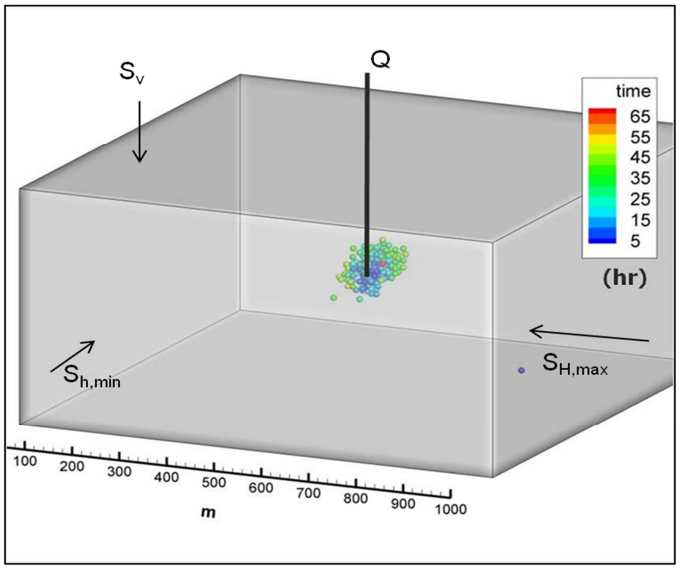

Fig. 8.4. Micro-seismic events after 3 days pumping for the case of strike-slip regime.

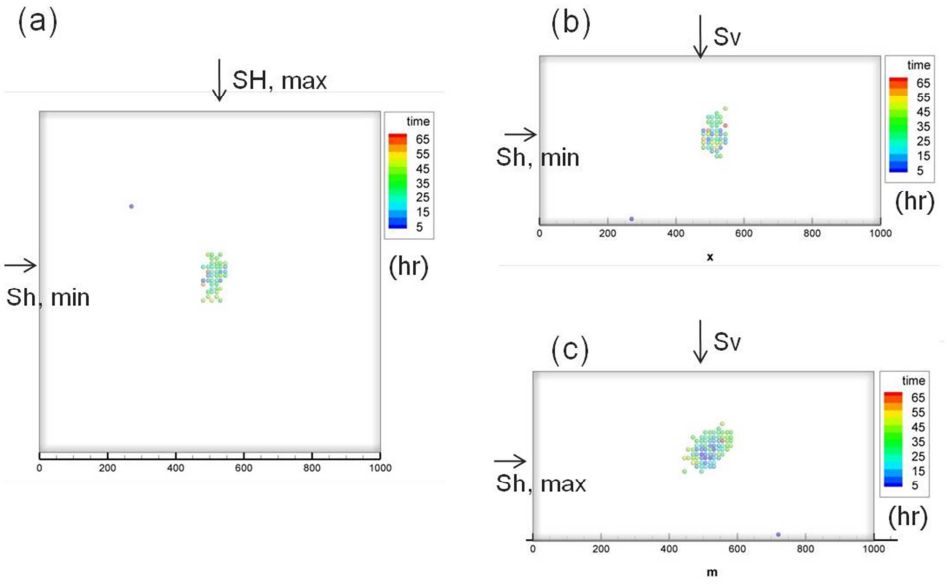

Fig. 8.5. Cross-sectional views for strike-slip regime. (a) represents top view, (b) is maximum directional side view, and (c) is minimum directional side view.

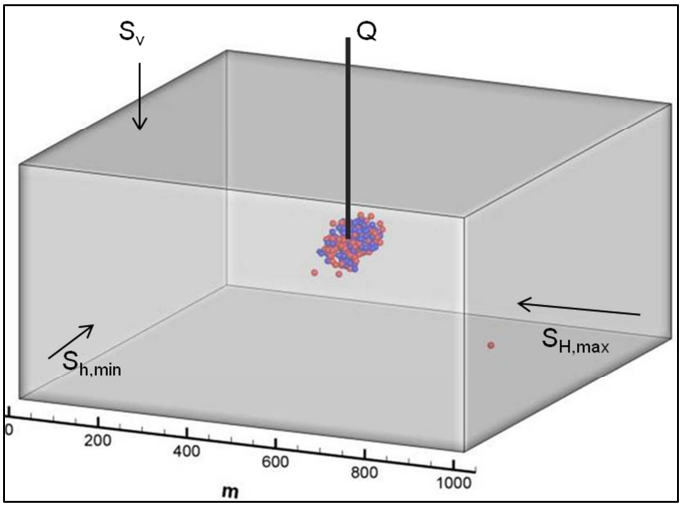

Fig. 8.6. Injection-induced failure analysis. Blue represents tensile failure and red shows shear failure.

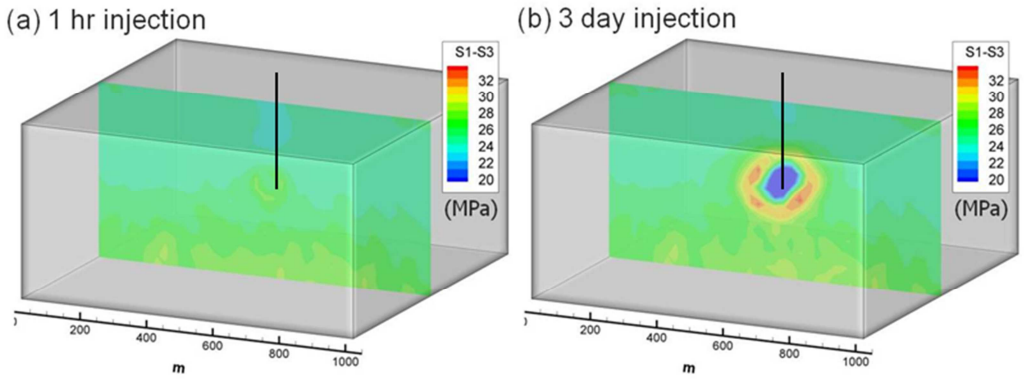

Fig. 8.7. The difference of maximum and minimum principal stress distribution for 1 hr injection (a) and after 3 days pumping (b).

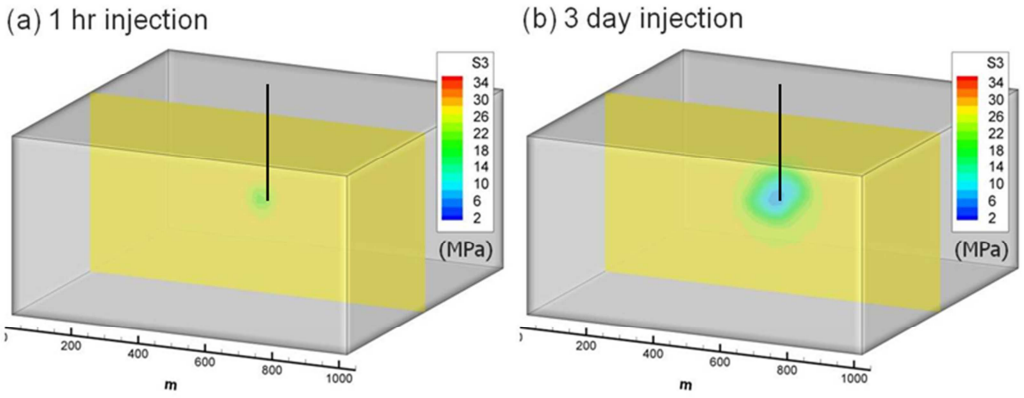

Fig. 8.8. Minimum principal stress distribution for 1 hr injection (a) and after 3 days pumping (b).

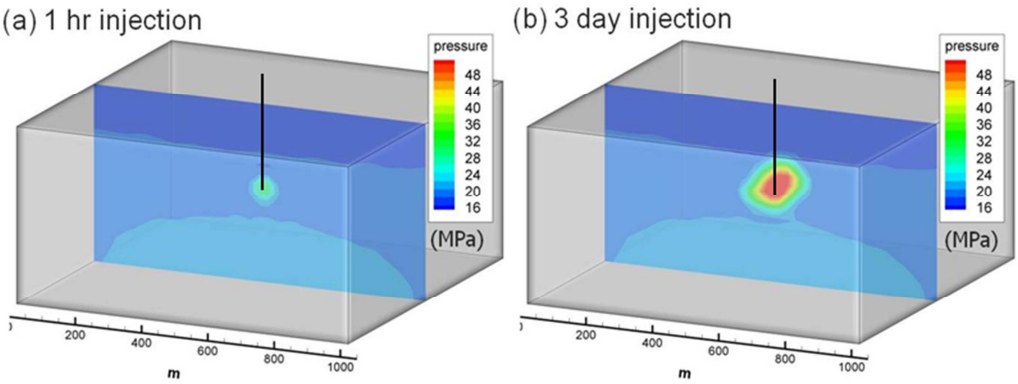

Fig. 8.9. Pore pressure distribution for 1 hr injection (a) and after 3 days pumping (b).

8.2 Microseismicity in thrust regime

In the Cooper Basin geothermal reservoir, the vertical far-field stress is the minimum (thrust regime). It has been tested with the same heterogeneity and injection rate schedule as performed in previous strike-slip regime. Injection-induced seismic events in a 3-day injection schedule are plotted in Fig. 8.10. Microsesimic events did not happen and the formation stabilized after 40 hrs because the rock failure did not occur with the given injection rate and far-field stress. The shape of the seismic-event clouds is spherical (Fig. 8.11) and the number of events is less than in the strike-slip regime case because the compressive far-field stress in the thrust regime case is higher; therefore, the possibility of rock failure was less with the same injection rate. Most seismic events were generated by shear failure in this simulation. Stress distributions for maximum and minimum principal are illustrated in Figs. 8.13 and 14.

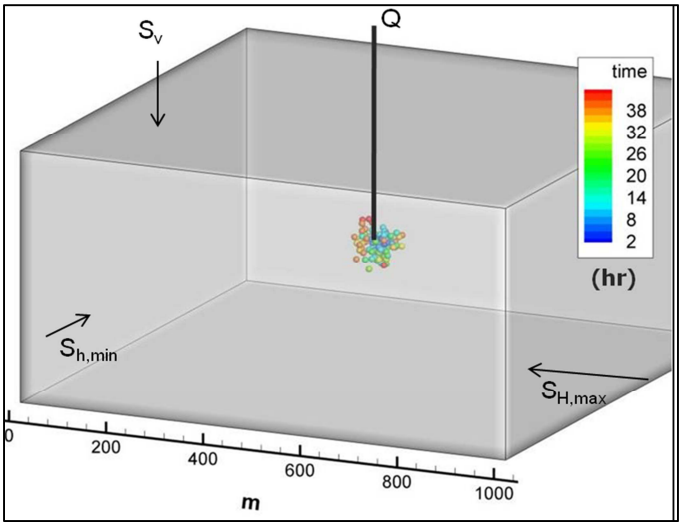

Fig. 8.10. Micro-seismic events after 3 days pumping for the thrust regime.

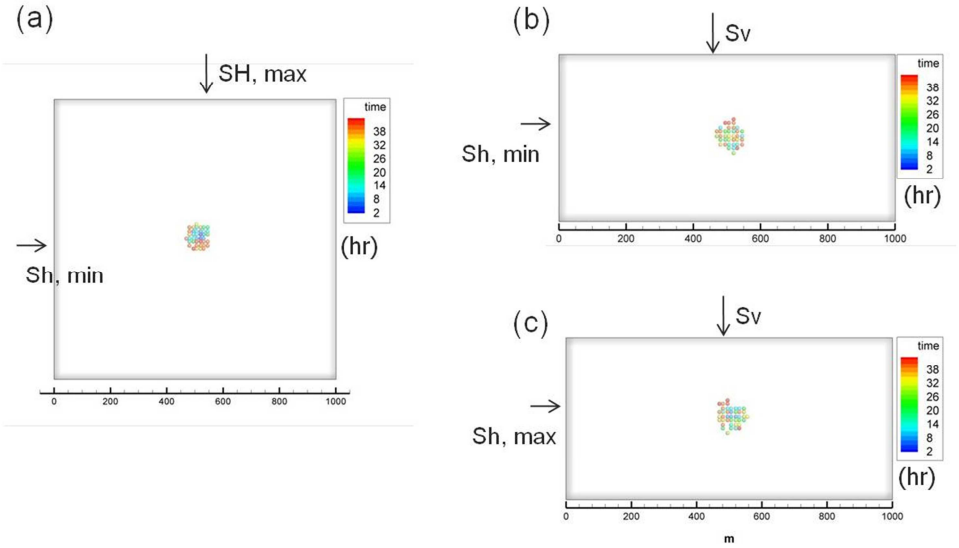

Fig. 8.11. Cross-sectional views for thrust regime. (a) represents top view, (b) is maximum directional side view, and (c) is minimum directional side view.

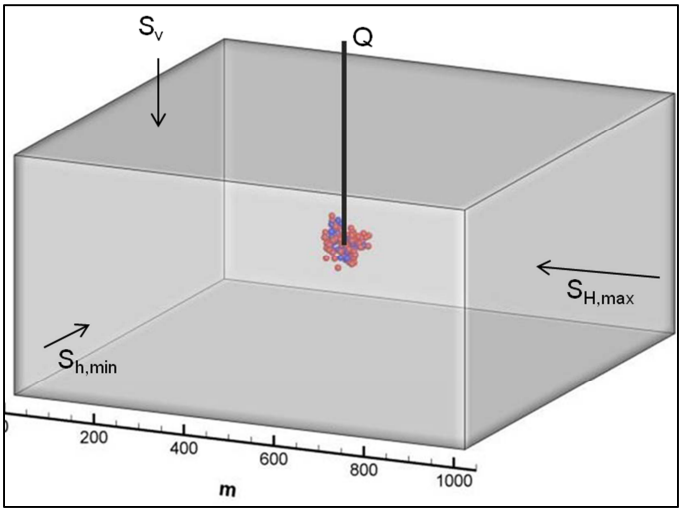

Fig. 8.12. Injection-induced failure analysis. Blue represents tensile failure and red shows shear failure.

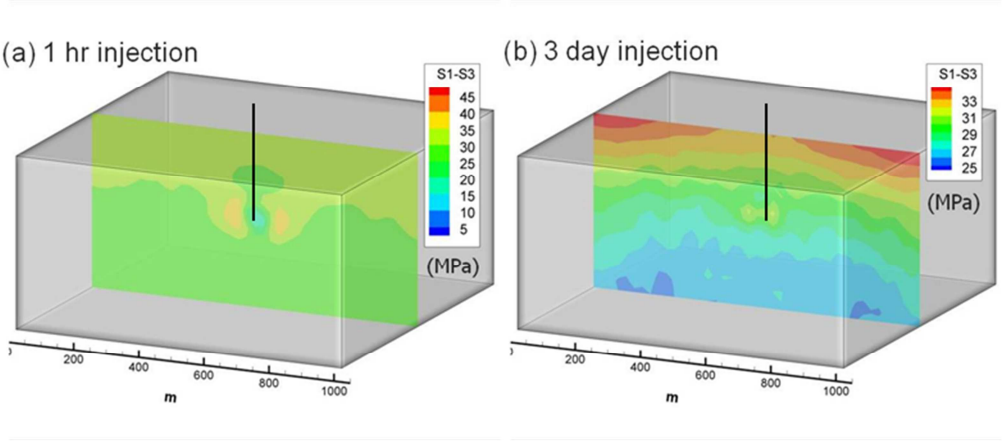

Fig. 8.13. The difference of maximum and minimum principal stress distribution for 1 hr injection (a) and after 3 days pumping (b).

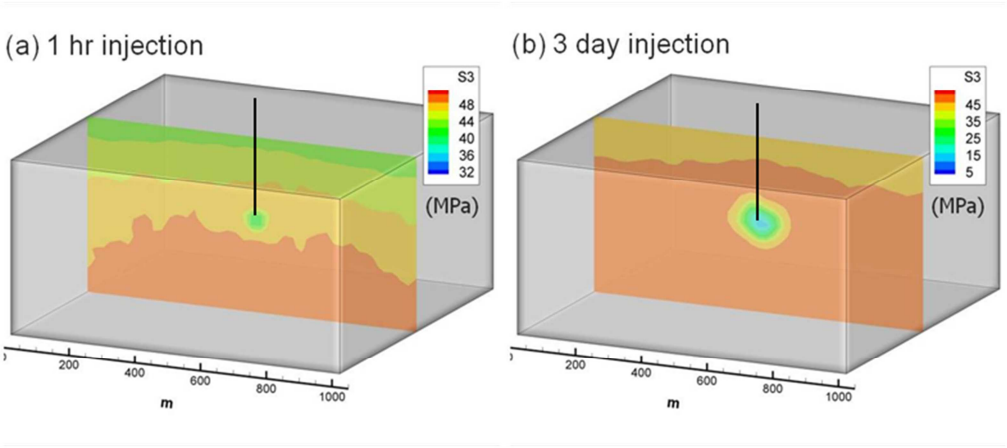

Fig. 8.14. Minimum principal stress distribution for 1 hr injection (a) and after 3 days pumping (b).

8.3 Microseismicity in normal regime

One of the most common stress regimes in reservoirs is the normal stress regime. In this stress regime, vertical fracturing is observed and the microseismic event shape is ellipsoidal because of the stress differences in horizontal far-field stress. Injection-induced seismic events are illustrated in Fig. 8.15. Small dots represent initial shear failure caused by natural compressive far-field stress. Cross-sectional views in Fig. 8.16 show that microseismic events are propagated to the maximum horizontal far-field stress direction and also to the vertical far-field stress direction. The pattern of events cloud is a penny shape, which is similar to hydraulic fracturing, but the events can be observed broadly since microseismic events include not only microcrack but also macrocrack generation by fluid injection. Shear and tensile failure modes are plotted in Fig. 8.17, which shows that shear failure is randomly observed at the bottom side because of the

increase in vertical far-field stress due to gravity, and also induced shear and tensile failure are observed because of water injection. Changes in principal stress distributions and pore pressure distributions are plotted in Figs. 8.18 to 8.20.

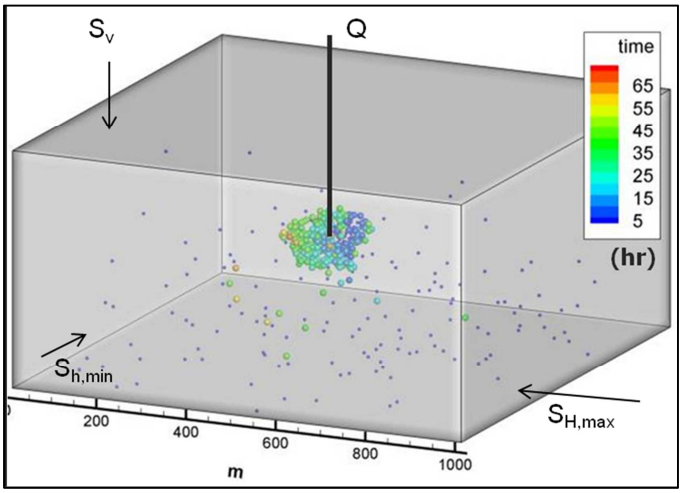

Fig. 8.15. Micro-seismic events after 3 days pumping for the normal regime.

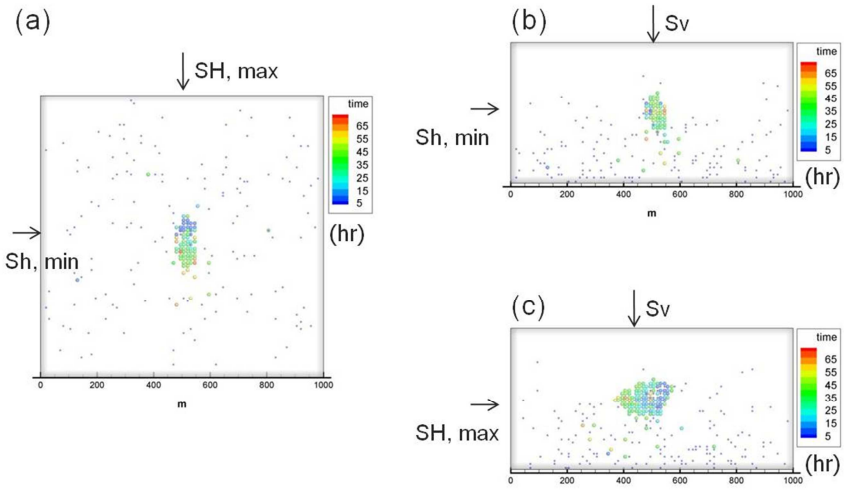

Fig. 8.16. Cross-sectional views for normal regime. (a) represents top view, (b) is maximum directional side view, and (c) is minimum directional side view.

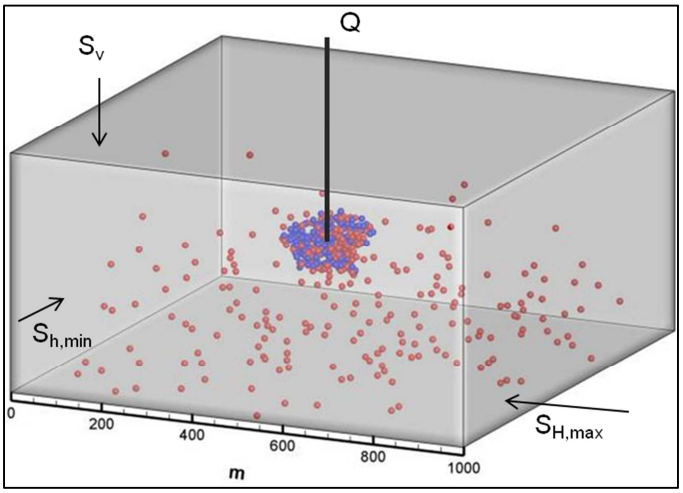

Fig. 8.17. Injection-induced failure analysis. Blue represents tensile failure and red shows shear failure.

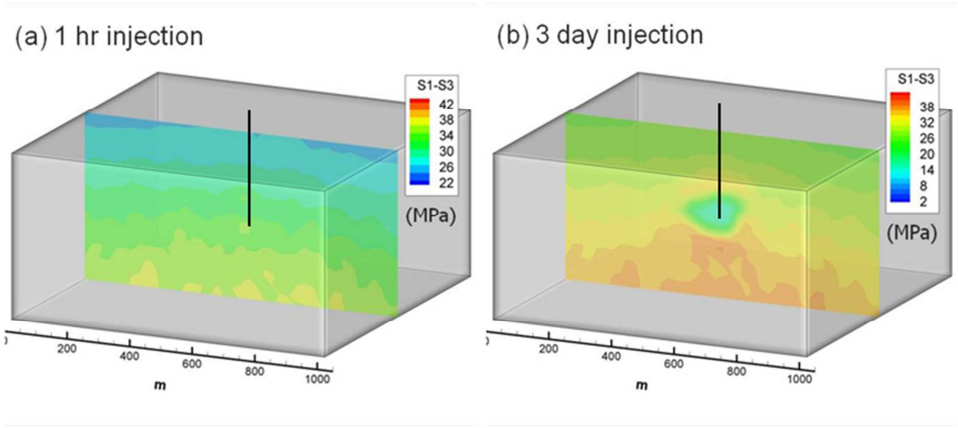

Fig. 8.18. The difference of maximum and minimum principal stress distribution for 1 hr injection (a) and after 3 days pumping (b).

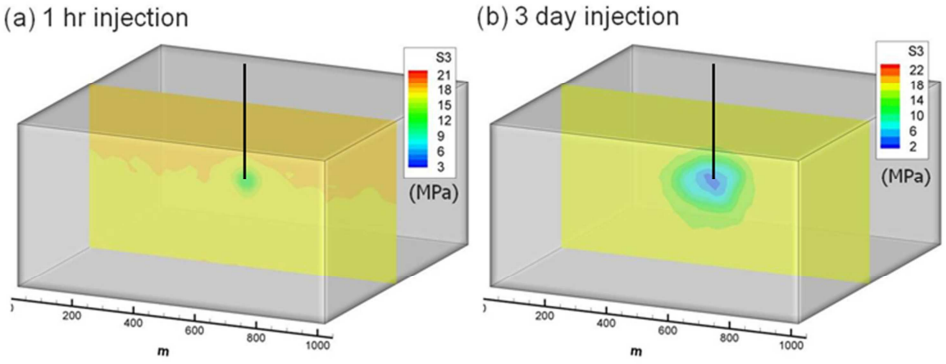

Fig. 8.19. Minimum principal stress distribution for 1 hr injection (a) and after 3 days pumping (b).

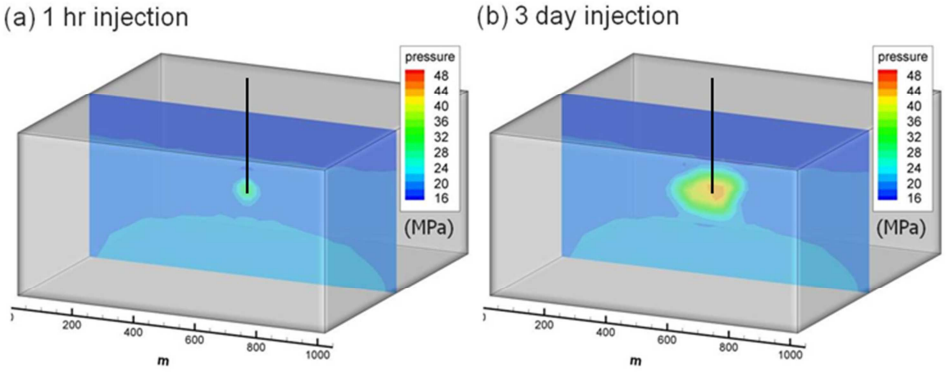

Fig. 8.20. Pore pressure distribution for 1 hr injection (a) and after 3 days pumping (b).

8.4 Discussion of microseismicity in three different stress regimes

We presented microseismic event propagation under three different stress regimes (strike-slip, thrust, normal regime) with the same injection schedule and the same distribution of heterogeneity of modulus and permeability. Results show that the patterns of microseismic events are penny shaped for strike-slip and normal regimes.

However, we observed differences in the event locations and times with changes in far-field stress conditions. Especially in the normal regime case, initial rock failure increased as the depth increased, and it also influenced the injection induced microseismic event propagation. The difference of seismic events with normal and strike-slip regimes is compared in Fig. 8.21. For the thrust regime in the simulation, it the distance of events from the injection source is relatively shorter than in the strike-slip and normal regimes because of the effective stress contributions toward shear and tensile failure. This is also observed in well-scale simulation (Section 7) for the thrust regime.

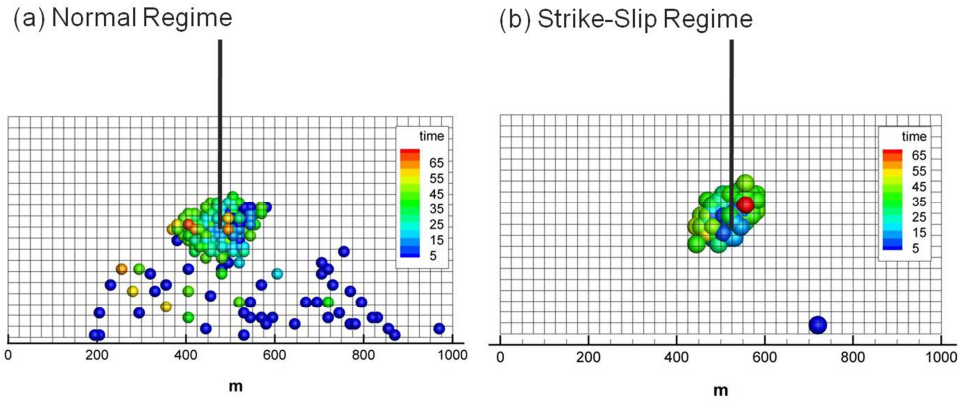

Fig. 8.21. Comparison of seismic events in normal and strike-slip regimes.

We tested the influence of permeability anisotropy in a thrust regime that had 10 times higher permeability in the horizontal directions and 10 times lower permeability in the vertical directions. This assumption is accompanied by the experimental results that the maximum fluid path increases proportionally as the deviatoric stress increases in rock. Results in Fig. 8.22 show that injection-induced microseismic events are

horizontally scattered. Note that small dots represent initial rock failure in the reservoir. Cross-sectional views in Fig. 8.23 show the microseismic events localized to the horizontal direction by fluid injection. This result indicates that the fluid flow path highly influences the stress distribution, and it causes the shape of the rock failure and microseismic events. Permeability distribution for the initial injection and after 3 days for the thrust regime is described in Fig. 8.24. The rock failure induced by injection increased permeability and triggered microseismicity.

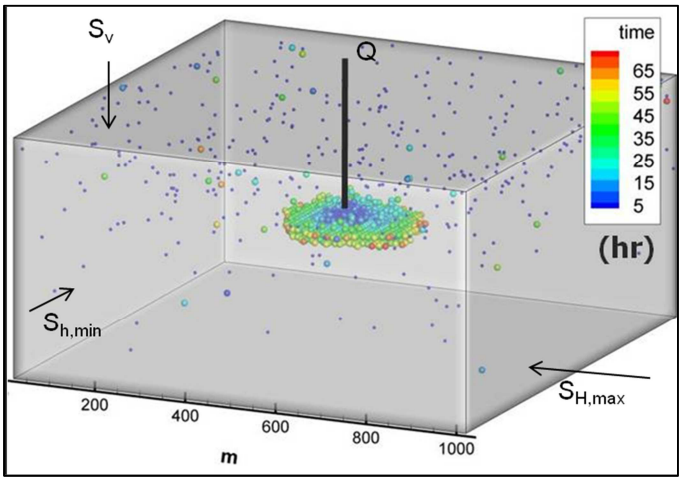

Fig. 8.22. Microseismic events after 3 days pumping in the highly anisotropic permeability case.

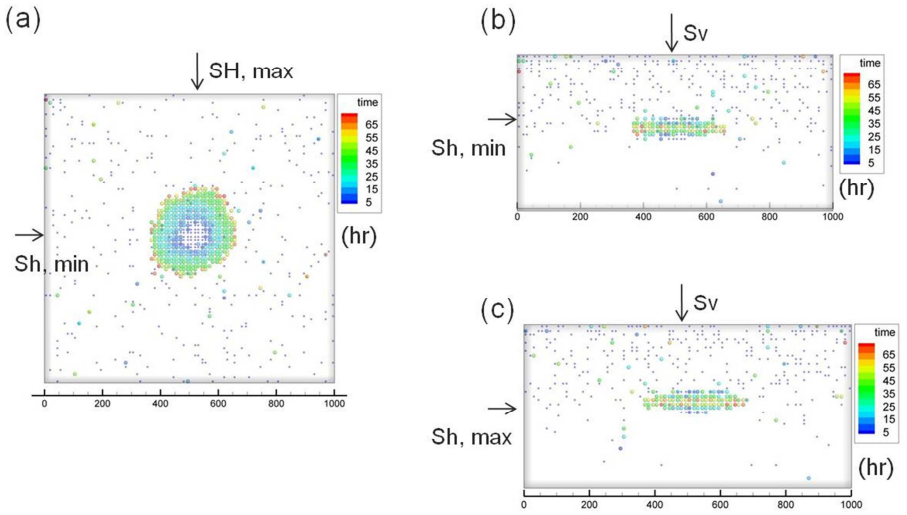

Fig. 8.23. Cross-sectional views for thrust regime. (a) represents top view, (b) is maximum directional side view, and (c) is minimum directional side view.

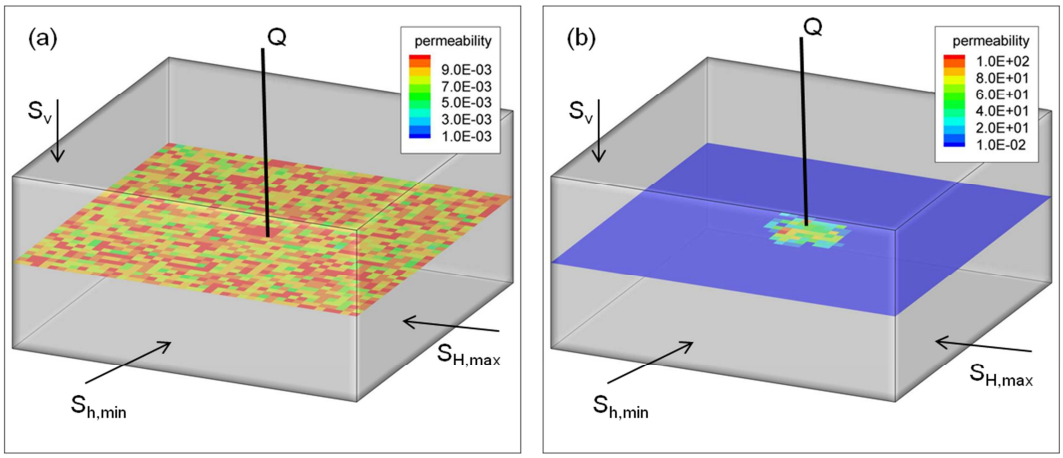

Fig. 8.24. Cross-sectional views for permeability distribution. (a) initial permeability distribution, (b) permeability distribution after 3 days injection.

8.5 Influence of deviatoric stress

In this section, we present the results of microseismic event propagation under three stress regimes that show different event propagation with the same injection schedule and the same distribution of heterogeneity. This indicates that the far-field stress plays an important role in induced seismicity. We studied the influence of deviatoric far-field stress in microseismic events propagations as changing horizontal deviatoric stresses. The simulation conditions for this study are presented in Table 8.2, in which horizontal far-field stress is changed with same vertical far-field stress (strike-slip regime). Permeability anisotropy is considered so that the vertical direction has 10 times lower permeability.

Table 8.2
Reservoir properties used in the simulations for stress regime and permeability anisotropy.

	Case 1	Case 2	Case 3
$S_{H,\,max}$	55 MPa	60 MPa	65 MPa
$S_{h,\,min}$	45 MPa	40 MPa	35 MPa
S_v	50 MPa	50 MPa	50 MPa
$k_{H,\,max}$	1×10^{-2} md	1×10^{-2} md	1×10^{-2} md
$k_{h,min}$	1×10^{-2} md	1×10^{-2} md	1×10^{-2} md
k_v	0.1×10^{-2} md	0.1×10^{-2} md	0.1×10^{-2} md

In contrast with the result for the thrust regime, the events cloud scattered horizontally. In the small deviatoric stress reservoir condition, the fluid path has the

dominant effect in microseismic event propagation since permeability anisotropy in horizontal direction is 10 times higher than in the vertical direction. However, if the horizontal deviatoric stresses increase as in cases 2 and 3, the influence of horizontal deviatoric stresses becomes significant as the deviatoric stresses increase. Figs. 8.25 to 8.27 show that microseismic events propagate to the maximum far-field stress direction, and the cloud shape is sharper in the maximum horizontal far-field stress direction as the deviatoric stress increases. The results indicate that permeability anisotropy is critical for event propagation when the deviatoric stress is not severe, and also the far-field stress influences the microseismic pattern as the deviatoric stress increases.

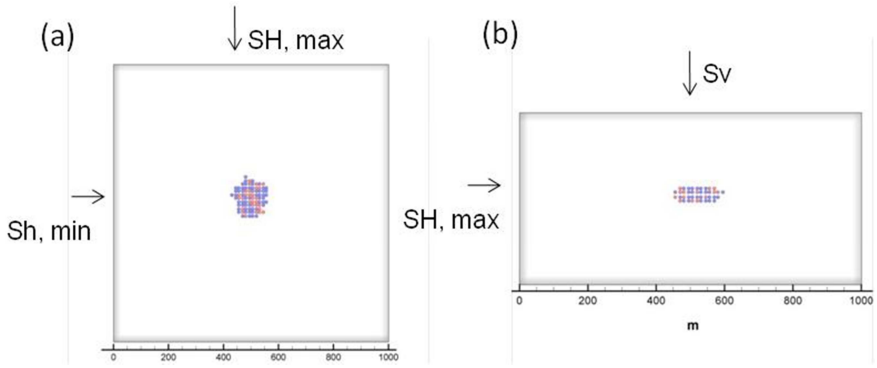

Fig. 8.25. Cross-sectional views for the case of 5 MPa as deviatoric stress after 3 day injection. (a) represents top view and (b) is minimum directional side view. Blue dots represent tensile failure and red dots are shear failure.

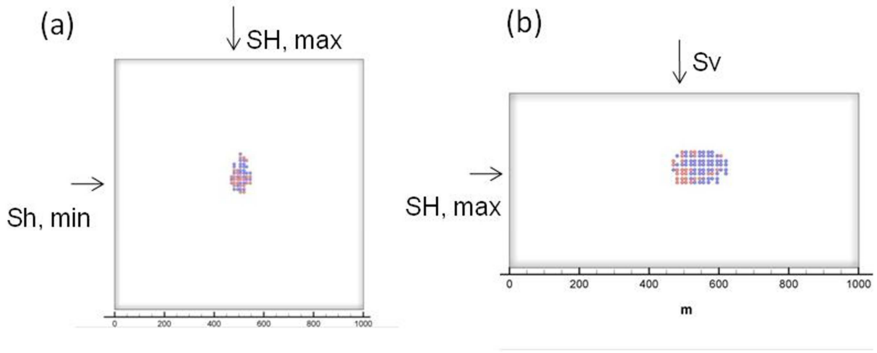

Fig. 8.26. Cross-sectional views for the case of 10 MPa as deviatoric stress after 3 day injection. (a) represents top view and (b) is minimum directional side view. Blue dots represent tensile failure and red dots are shear failure.

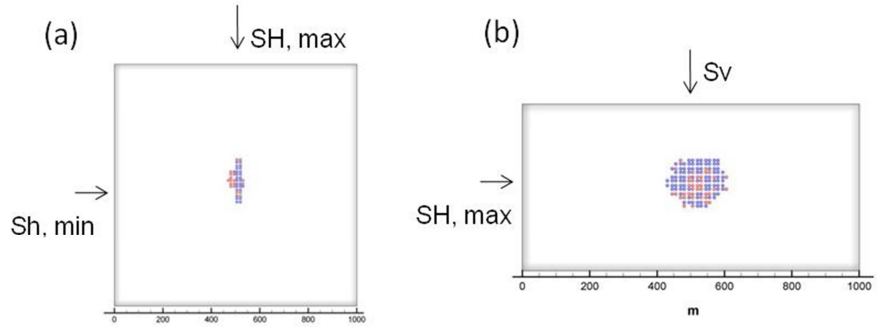

.

Fig. 8.27. Cross-sectional views for the case of 15 MPa as deviatoric stress after 3 day injection. (a) represents top view and (b) is minimum directional side view. Blue dots represent tensile failure and red dots are shear failure.

8.6 Anisotropic permeability

As we have seen in previous results, fluid path is one of the key factors for microseismic event analysis. In this simulation, we studied the influence of permeability anisotropy. Table 8.3 shows different permeability anisotropy, which increases the

permeability in the direction of the maximum horizontal far-field stress. Note that vertical permeability is lower than horizontal permeability and only the values of $k_{H,\,max}$ are changed and far-field stress conditions are the same.

Table 8.3.
Input parameters for stress regime and permeability anisotropy.

	Case 1	Case 2	Case 3
$S_{H,\,max}$	60 MPa	60 MPa	60 MPa
$S_{h,\,min}$	40 MPa	40 MPa	40 MPa
S_v	50 MPa	50 MPa	50 MPa
$k_{H,\,max}$	2×10^{-2} md	5×10^{-2} md	10×10^{-2} md
$k_{h,min}$	1×10^{-2} md	1×10^{-2} md	1×10^{-2} md
k_v	0.1×10^{-2} md	0.1×10^{-2} md	0.1×10^{-2} md

Figs. 8.28 to 8.30 show seismic event clouds for different permeability anisotropy after 3 day injection. The shape of the microseismic event clouds becomes narrow and sharper as the permeability anisotropy increases in the maximum direction because of the localization in the fluid path. Note that few events appear in the vertical direction because vertical permeability is 10 times lower than horizontal permeability.

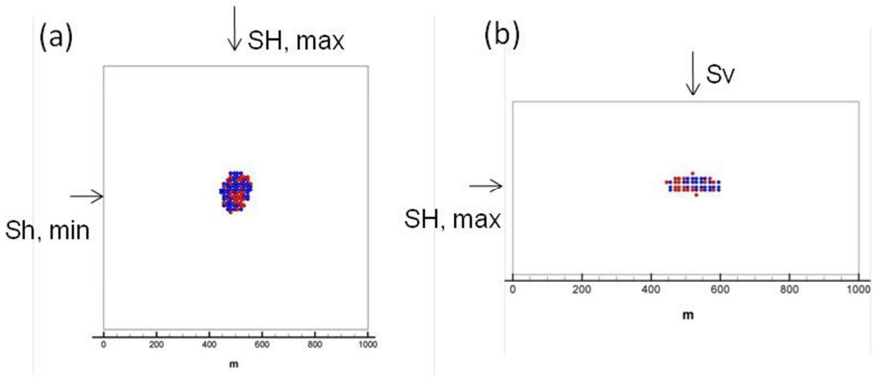

Fig. 8.28. Cross-sectional views for the case of $k_{H,\,max} = 2 \times k_{H,\,min}$ after 3 day injection. (a) represents top view and (b) is minimum directional side view. Blue dots represent tensile failure and red dots are shear failure.

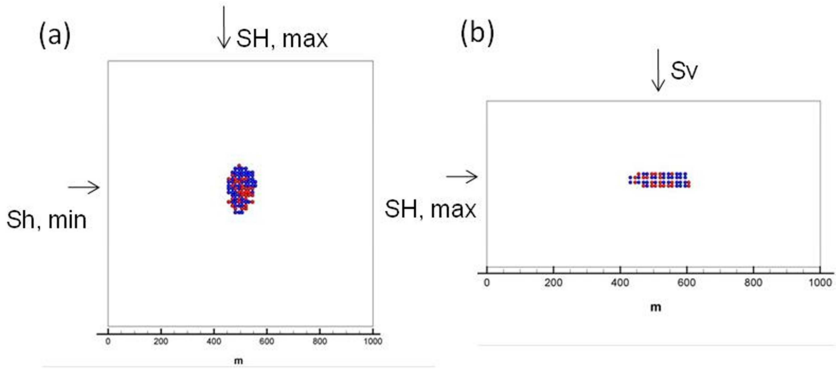

Fig. 8.29. Cross-sectional views for the case of $k_{H,\,max} = 5 \times k_{H,\,min}$ after 3 day injection. (a) represents top view and (b) is minimum directional side view. Blue dots represent tensile failure and red dots are shear failure.

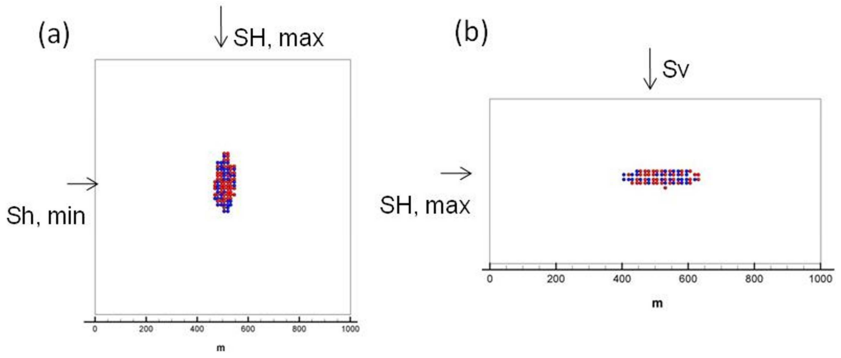

Fig. 8.30 Cross-sectional views for the case of $k_{H,\,max} = 10 \times k_{H,\,min}$ after 3 day injection. (a) represents top view and (b) is minimum directional side view. Blue dots represent tensile failure and red dots are shear failure.

8.7 Microseismic simulations in Soutz-Sous-Forets stress regime

We performed microseismicity simulation with a Soultz-Souls-Forest stress regime. One of the most important characteristics in the GPK-1 and GPK-2 stress regime is a transition of stress regime froma normal regime to a strike-slip regime as the reservoir depth increases, as shown in Fig. 8.31. Three different stress regimes have been tested: the normal regime (1.25 km – 1. 75 km), the transition (2.75 km – 3.25 km), and the strike-slip regime (4.25 km – 4.75 km). We assumed that there are no natural fracture and fault in this simulation.

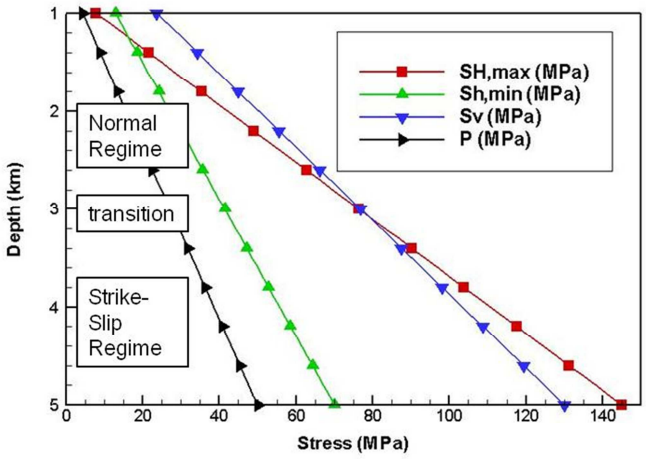

Fig. 8.31. Change of far-field stress with respect to depth in Soultz-Sous-Forets geothermal reservoir.

Microseismic events propagation with time and failure mode at 1.25 km–1.75 km are plotted in Fig. 8.32 and Fig. 8.33 (normal regime). Microseismicity propagated perpendicular to the minimum horizontal far-field stress direction. Transition and strike-slip regime cases are also plotted in Figs. 8.34 to 8.37. The minimum far-field stress does not change with depth variations as the minimum; therefore, microseismic events are propagated normal to the minimum far-field stress directions. Both shear and tensile failure from fluid injection were observed. The comparison of microseismic events propagation as the depth increase is illustrated in Fig. 8.38.

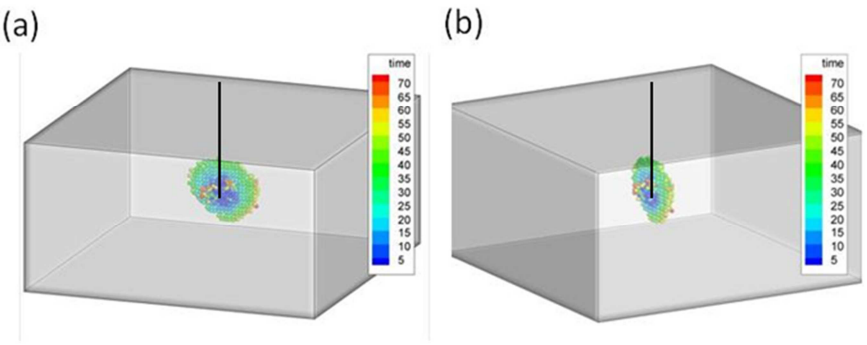

Fig. 8.32. Cross-sectional views for the normal regime (1.25km – 1.75km) after 3 day injection. (a) represents top view and (b) is minimum directional side view.

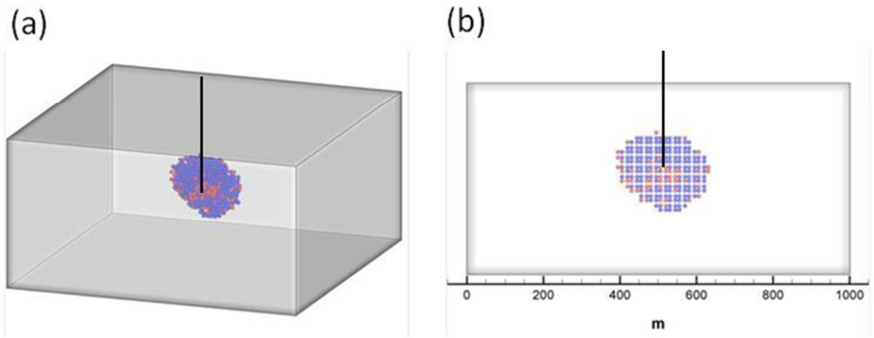

Fig. 8.33. Shear and tensile failure plot for the normal regime (1.25km – 1.75km) after 3 day injection. (a) represents top view and (b) is minimum directional side view. Blue dots represent tensile failure and red dots are shear failure.

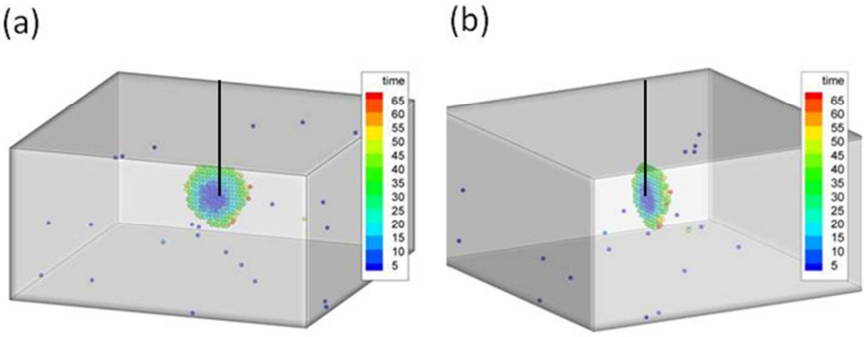

Fig. 8.34. Cross-sectional views for the transition regime (2.75km – 3.25km) after 3 day injection. (a) represents top view and (b) is minimum directional side view.

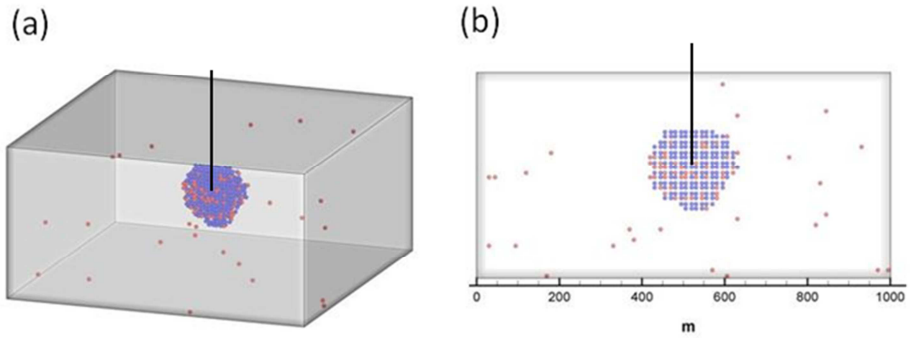

Fig. 8.35. Shear and tensile failure plot for the transition regime (2.75km – 3.25km) after 3 day injection. (a) represents top view and (b) is minimum directional side view. Blue dots represent tensile failure and red dots are shear failure.

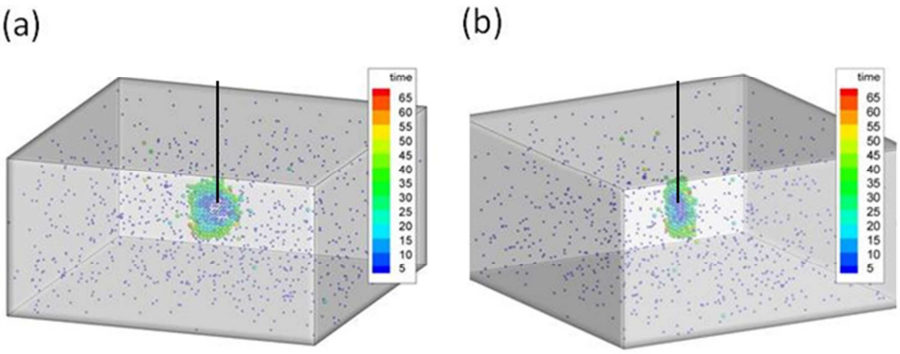

Fig. 8.36. Cross-sectional views for the strike-slip regime (4.25km – 4.75km) after 3 day injection. (a) represents top view and (b) is minimum directional side view.

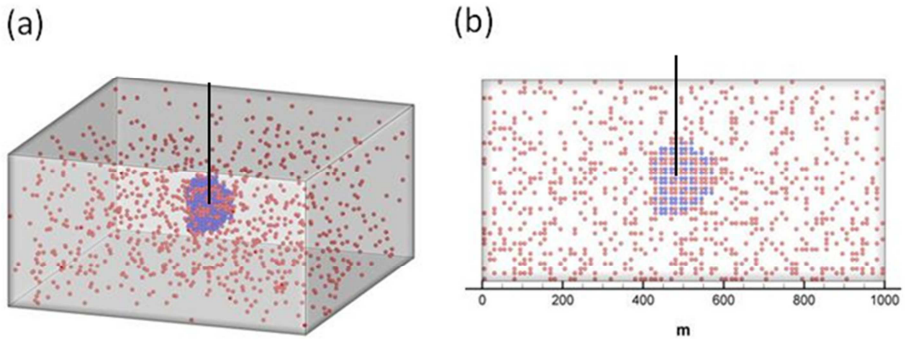

Fig. 8.37. Shear and tensile failure plot for the strike-slip regime (4.25km – 4.75km) after 3 day injection. (a) represents top view and (b) is minimum directional side view. Blue dots represent tensile failure and red dots are shear failure.

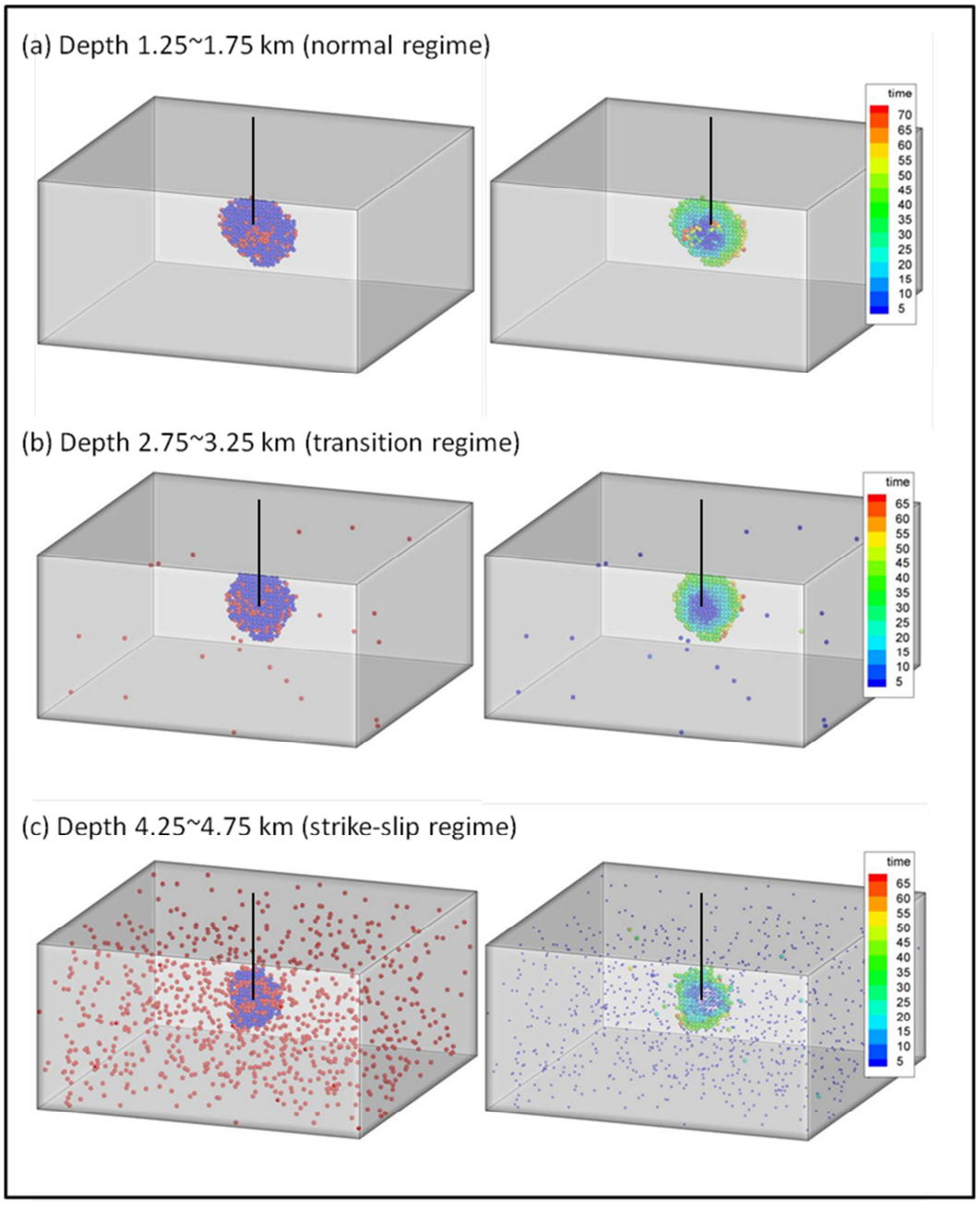

Fig. 8.38. Comparison of microseismic events propagation under different depth. (a) injection depth is 1.5 km in normal regime (b) 3 km in transition regime, and (c) 4.5 km in strike-slip regime.

We also performed injection-induced microseismic event propagations in existing natural fractures. The mesh used in this simulation is 250 m×250 m×250 m with an 8-node hexahedron element and one simplified, circular natural fracture (representing the conceptual model of a Soutz-Sous-Forets geothermal reservoir). The natural fracture is inclined by 20° from the vertical direction, and its fracture radius is 50 m (Bruel, 2002). To describe the natural fracture in finite element modeling, we assumed that is modulus is 10^{-5} times lower (~0.1 MPa) and permeability is 10^{6} times higher (~10^{3} md) than an intact granite reservoir, and its cohesive strength is zero in the naturally fractured zone. The mesh for numerical modeling is presented in Fig. 8.39. Fig. 8.40 shows the initial natural fracture configuration and initial distribution of modulus. The stress regime in this simulation is a normal regime with $S_{H,\max}$ = 50 MPa, $S_{h,\min}$ = 30 MPa, and S_v = 60 MPa; the injection rate is 24 L/sec.

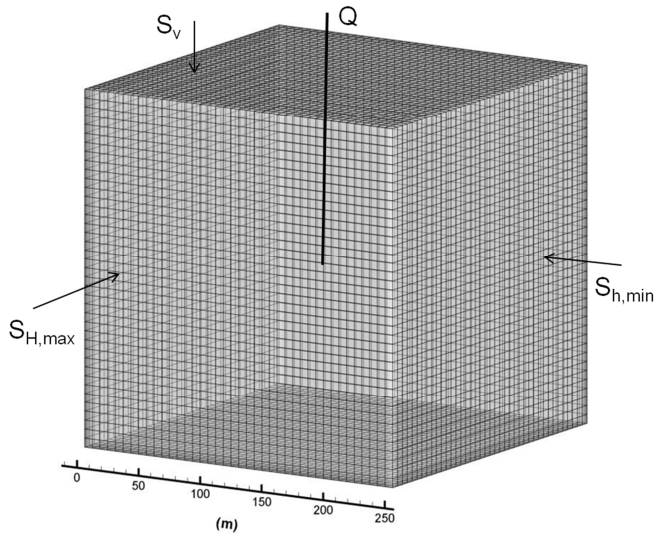

Fig. 8.39. Mesh used in naturally fractured reservoir simulation; 250×250×250 m^3 with 64,000 elements.

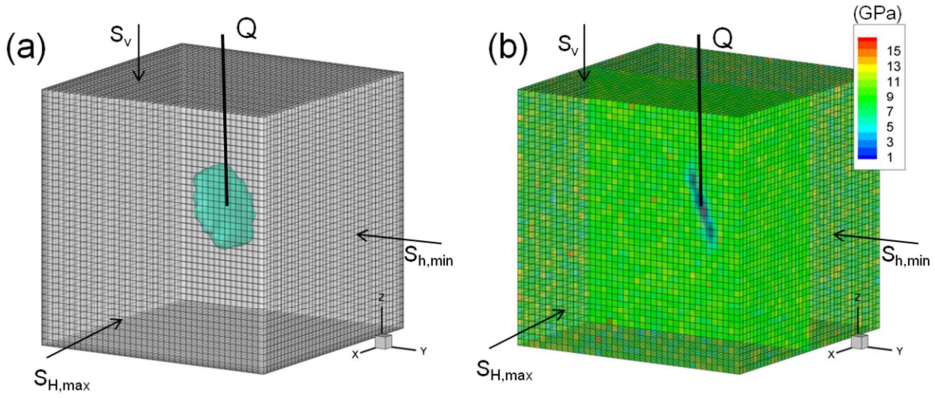

Fig. 8.40. Natural fracture configuration is illustrated in (a), and initial distribution of modulus properties are plotted in (b).

The results for microseismic event propagation with time and pore pressure distribution after a 3 day injection schedule are presented in Fig. 8.41. The microseismic event propagation in Fig 8.41(a) shows almost the same growth rate in the up and down direction because the influence of gravity in far-field stress, initial pore pressure, and fluid gravity is ignored in this simulation. Note that the microseismic event propagation is fast inside the natural fracture in early time steps because of quick fluid movement to the natural fracture, and then there is a small delay to generate propagation of new events. A possible reason is that it needs more pore pressure to propagate the rock failure in the intact rock since rock properties and permeability are discontinuous between the natural fracture and the intact rock. The comparison of numerically obtained microseismicity with real field date is presented in Fig. 8.42. The numerical simulation that assumed a single large fracture can describe the main features of the experimental

data in Soultz-Sous-Forets. However, the distribution of microseismicity between the simulation and field data is different. To improve the numerical modeling for microseismicity, it is necessary to consider not only large main fracture but also other factors that can influence microseismicity, such as localized permeability distribution, modulus, and rock strength in small natural fractures around the injection area.

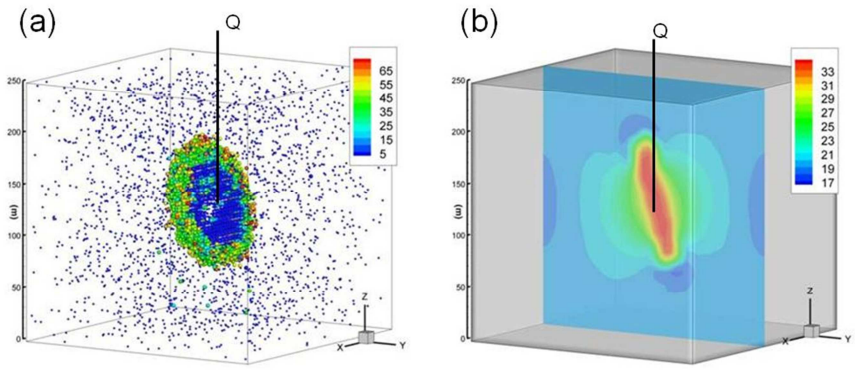

Fig. 8.41. Microseismic event propagation and pore pressure distribution with fluid injection to the natural fracture. (a) microseismic events propagation with time (b) pore pressure distribution after 3 days injection.

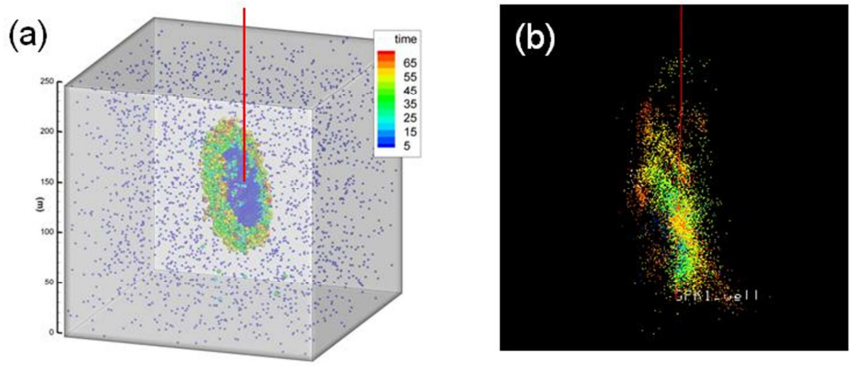

Fig. 8.42. Comparison of numerical results for injection-induced microseismicity with experimental data. (a) numerical results assuming the injection in single large fracture (b) experimental data at GPK1-well in Soultz-Sous-Forets geothermal reservoir.

8.8 Conclusions

The influence of far-field stress and permeability anisotropy has been studied through a thermo-hydro-mechanical model with damage evolution. Point source injection was applied to simulate a large reservoir efficiently. A fully-coupled finite element method with damage mechanics provided the tools to analyze injection induced microseismicity. Results show that the far-field stress and permeability anisotropy influence the stress distributions, which in turn impact microseismic event propagations. The event propagation is perpendicular to the minimum far-field stress distribution. Cold water injection in normal or strike-slip regime leads to vertical propagation, which can capture the effects of hydraulic fracturing, but the event cloud shape is also related with permeability anisotropy when deviatoric stress is small. Thermal stress plays an important role for predicting the stress distribution by cold water injection and triggered microseismicity in early time steps. The pattern of microseismic events becomes elliptical and localized when the reservoir permeability anisotropy increases. Injection induced microseismicity in single large, fractured reservoirs also has been presented. Results show that event propagations are triggered quickly inside the fracture because of low modulus and higher permeability in natural the fracture. Comparing the simulated microseismicity with real data for Soultz-Sous-Forets qualitatively showed that numerical results with the assumption of a single large fracture can capture the main distribution of microseismicity in field experimental data.

9. CONCLUSIONS AND RECOMMENDATIONS

9.1 Conclusions

Thermo-poro-mechanical and chemo-thermo-poro-mechanical models for the rock response to fluid injection and drilling mud infiltration were developed using the finite element method. The rock failure and damage propagation were modeled by considering the nonlinear strain-stress behavior of rock. Damage mechanics and stress-dependent permeability were also implemented into the finite element model. The model has been applied to plain-strain wellbore stability analysis in shale to study the effects of solute transport, heat transfer, and stress distribution around a wellbore. Also, a thermo-poro-mechanical process with damage mechanics and stress-dependent permeability was applied to two- and three-dimensional damage/fracture propagation and microseismicity. Especially for three-dimensional simulation, both well-scale and reservoir-scale numerical modeling was presented.

Finite element simulation of triaxial compression behavior of rock was carried out to find out optimum damage mechanics material parameters which can describe microvoid and microcrack growth and crack propagation. The hardening and softening behavior of rock and strain-permeability behavior under compression were compared with the experimental results. We described the influence of material parameters to determine the peak stress and residual strength regime.

The alteration of modulus and permeability with rock damage has been studied. The results show that the discontinuity of modulus and permeability causes retardation of fluid movement between the high permeability damaged and low permeabilty undamaged rock. Stress relaxation by modulus reduction in the damaged zone also plays an important role in propagation of damage and leads to the stress concentration between the interface of damaged and undamaged rock.

In shale instability analysis, if mud salinity is lower than the formation, it enhances rock damage by shear and tensile failure around a wellbore because of osmosis effects between the drilling mud and shale formation. Cooling of the rock causes more tensile hoop stress and reduces the pore pressure around a wellbore than in isothermal conditions. Results show that thermally induced tensile stress contributes to stabilize the shear failure in the minimum far-field stress direction; however, it enhances tensile failure potential in the maximum far-field stress direction.

We studied distribution of two- and three-dimensional injection-induced damage propagation microseismic events using the fully-coupled thermo-poroelastic finite element methods. To simulate the rock mass more realistically, heterogeneous modulus and permeability were implemented in the numerical modeling of microseismic events. We assumed that the rock properties follow a statistical distribution generated using the Weibull distribution function. Both well-scale and reservoir-scale simulation have been developed for the analysis of injection-induced rock damage and microseismic event propagation. We found that deviatoric far-field stress and permeability anisotropy contribute to predict the localization of microseismic event propagation. The results

show that the shape of injection-induced microseismic events becomes elliptical and sharper as the deviatoric far-field stress and permeability anisotropy increase. Also we illustrated that the microseismic events are localized when we use rock failure criteria for comparing the pore pressure criticality.

Results show that a finer mesh provides more accurate numerical solutions but there are limitations of computational speed and memory storage to solve large-scale, fully-coupled problems. To optimize the mesh size and element numbers, we used a finer mesh around the wellbore and saw significant changes of pore pressure, temperature, and solute mass concentration. For the wellbore stability problem, the system domain size is relatively small compared to the injection simulation, so we used a much finer mesh around a 2-meter radius zone around the wellbore. However, for the injection simulations, damage propagation in the maximum direction is longer than wellbore stability problem. So that a fine mesh is used not only around a wellbore but also in the areas parallel to the maximum far-field stress direction. There is a possibility of unrealistic large damage propagation if the mesh size is too large to accurately compute the stress localizations within elements.

9.2 Recommendations

In this dissertation, we considered single-phase water injection and a mechanical damage model. For future studies, the following topics are recommended.

- Multiphase flow simulation (water and steam in geothermal reservoirs, oil, gas, and water in petroleum reservoirs)

- Naturally fractured reservoir simulation
- Damage model improvement (thermal, chemical, and mechanical damage model)
- Extended finite element method to simulate fracture propagation efficiently
- Discrete heterogeneous model to depict more realistic geomechanics simulation
- Multilayer simulation
- Anisotropic damage mechanics

The applications of heterogeneous reservoir modulus and permeability have been used to depict more realistic geomechanics simulations. In this work, a continuous stochastic model approach was used to simulate heterogeneous reservoirs. However, in reality geological media have a lot of discrete features such as fissures, faults, and natural fractures. To simulate these more realistically, we recommend introducing a combined approach of stochastic and discrete modeling. For example, we can model the natural fracture and faults by discrete modeling and other regions can be described with continuous stochastic modeling. Finer mesh will be better for near injection and production well, and coarse mesh is recommended for the regions where fluid injection and production do not cause much variation in stress, etc. The choice of finer and coarser mesh sizes is relative to the total reservoir size that needs be simulated, the numerical accuracy requirements for each case, and the variations of numerical variables by boundary conditions such as injection rate, well pressure, production rate, and far-field stress. The mesh dependency problem is more significant when we consider the nonlinear stress-strain behavior. Fig. 9.1 shows a typical example of damage/fracture

trajectory with different scales of mesh size. We observed that damage distributions are localized as mesh density increases with the same loading conditions. Particularly for the simulation of damage propagation, the loading condition and post-peak response contributes to mesh density (Abu Al-Rub and Kim, 2010). As the mesh size decreases, average variation of displacement decreases during the damage propagation because of damage localization in finer mesh. Therefore, it is necessary to use finer mesh in finite element modeling for the nonlinear behavior of rock and stress dependent permeability.

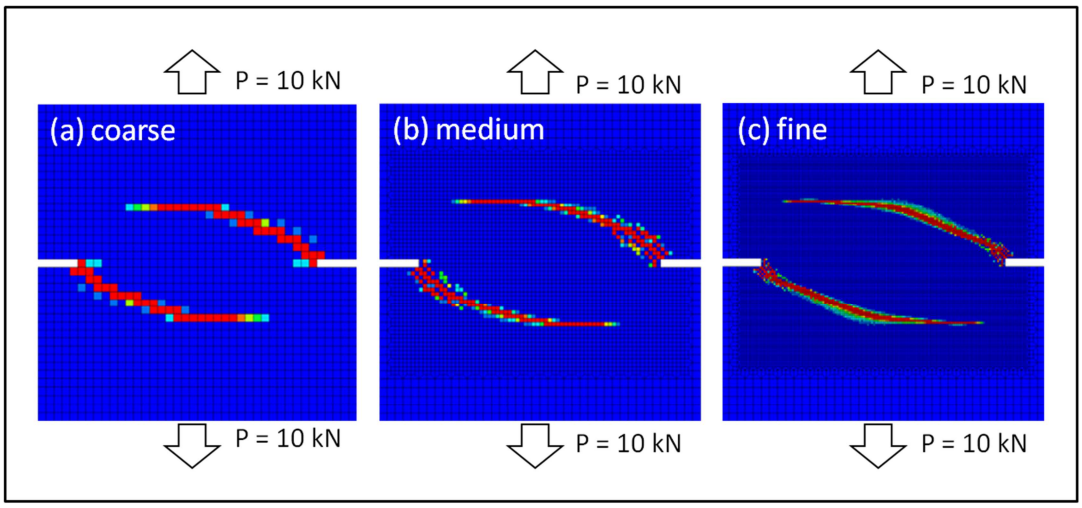

Fig. 9.1. Simulated crack propagation for three mesh densities: (a) coarse, (b) medium, and (c) fine (Abu Al-Rub and Kim, 2010).

NOMENCLATURE

a	Compressibility
A	Cross-sectional area
A^D	Damaged cross-sectional area
B	Skempton coefficient
c_f	Fluid diffusion coefficient
c_F	Cohesive strength
c_p	Specific heat capacity
c_T	Thermal diffusivity
C^S	Solute concentration
d	Damage variable
D^S	Solute diffusivity
E	Elastic modulus
f	loading pressure
f_c	Maximum compressive strength
f_{cr}	Residual compressive strength
f_{tr}	Residual tensile strength
f_q	fluid injection rate
G	Shear modulus
h	Depth between bottom and surface
J^f	Fluid flux

J^S	Solute mass flux
k	Permeability
k_0	Initial permeability
$k_{H,max}$	Maximum horizontal anisotropic permeability
$k_{h,min}$	Minimum horizontal anisotropic permeability
k_v	Vertical anisotropic permeability
k^T	Thermal conductivity
$\boldsymbol{K}$	Elastic stiffness matrix
$\boldsymbol{J}$	Jacobian matrix
M	Biot modulus
$\boldsymbol{N}$	Shape function vector
p	Pore pressure
p_0	Initial pore pressure
P_0	Isotropic far-field stress
s	the variables of s_0
s_0	mean value of the corresponding of s
S_0	Finite shear stress
S_0	Deviatoric component in far-field stress
S_1	Finite shear stress
$S_{H,max}$	Maximum horizontal far-field stress
$S_{h,min}$	Minimum horizontal far-field stress
S_v	Vertical far-field stress

t	Time
T	Temperature
T_0	Initial temperature
u	Displacement of x-direction
v	Displacement of y-direction
w	Displacement of z-direction
w_s	Displacement of z-direction at the surface
α	Biot's constant
α_f	Volumetric thermal expansion coefficient of fluid
α_S	Volumetric thermal expansion coefficient of solid
β	Thermal expansion coefficients
β_d	Material parameter for stress-dependent permeability
ε	Strain
ε_c	Maximum compressive strain
ε_{cr}	Residual compressive strain
ε_{tr}	Residual tensile strain
ε_v	Volumetric strain
ϕ	Porosity
ϕ_f	Friction angle
μ	Fluid viscosity
θ	Parameter for time discretization

μ	Fluid viscosity
ρ_m	Total mass density
ν	Poisson ratio
ν_u	Undrained poisson ratio
σ	Total stress
σ'	Effective stress
σ_1	Maximum principal stress
σ_3	Minimum principal stress
τ	Stress which has the relationship with strain in linear elasticity
ω_0	Swelling coefficient
ξ	Fluid content
ξ_d	Increasing factor for permeability increase after failure
$\Re$	Reflection coefficient

REFERENCES

Abu Al-Rub, R. K., Kim, S.M., 2010. Computational application of a coupled plasticity-damage constitutive model for simulating plain concrete fracture. Eng. Fracture Mech. 77, 1577-1603.

Adushkin, V., Rodionov, V.N., Turuntaev, S., 2000. Seismicity in the oil field. Oilfield Review 1, 2–17.

Babuska, I., 1971. Error bounds for finite element methods. Num. Math. 16, 322–333.

Babuska, I., 1973. The finite element method with Lagrange multipliers. Num. Math. 20, 179–192.

Bai, M., Elsworth, D., 1994. Modeling of subsidence and stress-dependent hydraulic conductivity for intact and fractured porous media. Rock Mech. Rock Eng. 27, 209–234.

Bai, M., Meng, F., Elsworth, D., Roegiers, J.C., 1999. Analysis of stress-dependent permeability in nonorthogonal flow and deformation fields. Rock Mech. Rock Eng. 32(3), 195–219.

Baisch, S., Voros, R., Rothert, E., Stang, H., Jung, R., Schellschmidt, R., 2009. A numerical model for fluid injection-induced seismicity at solutz-sous-forets. Int. J. Rock Mech. Min. Sci. 47(3), 405–413.

Bart, M., Shao, J.F., Lydzba, D., 2000. Poroelastic behavior of saturated brittle rock with anisotropic damage. Int. J. Num. and Anal. Meth. Geomech. 24, 1139–1154.

Biot, M.A., 1941. General theory of three-dimensional consolidation. J. Appl. Phys. 12, 155–164.

Brezzi, F., 1974. On the existence, uniqueness and approximations of saddle point problems arising from Lagrange multipliers. RAIRO Anal.Numer 8 (2), 129–51.

Bruel, D., 2002. Impact of induced thermal stress during circulation tests in an engineered fractured geothermal reservoir. Oil & Gas Sci. Tech. 57, 459–470.

Bruno, M.S., Bovberg, C.A., Nakagaw, F.M., 1991. Anisotropic stress influence on the permeability of weakly-cemented sandstones. In: Proceedings, 32nd U.S. Symposium on Rock Mechanics, Norman, OK, USA, 375–384.

Cacas, M.C., Ledoux, E., de Marsily G., 1990. Modeling fracture flow with a stochastic discrete fracture network: calibration and validation 2. The transport model. Water Resour. Res. 26, 491–500.

Carter, J.P., Booker, J.R., 1982. Elastic consolidation around a deep circular tunnel. Int. J. Solids Struct. 18, 1059–1074.

Chenevert, M.E., 1970. Shale control with balanced-activity oil-continuous muds. J. Petrol. Technol. 22 (10), 1309–1316.

Cheng, H., Dusseault, M.B., 1993. Deformation and diffusion behaviour in a solid experiencing damage: a continuous damage model and its numerical implementation. Int. J. Rock Mech. Min. Sci. Geomech. Abstr. 30, 1323–1331.

Chin, L.Y., Raghavan, R., Thomas, L.K., 2000. Fully coupled geomechanics and fluid-flow analysis of wells with stress-dependent permeability. Soc. Petrol. Eng. 5 (1), 32–45.

Chow, C.L., Wang, J. 1987. An anisotropic theory of continuum damage mechanics for ductile fracture. Eng. Fracture. Mech. 27, 547–558.

Cook R.D., Malkus D.S., Plesha, M.E., Witt, R.J., 2001. Concepts and application of finite element analysis, fourth ed. John Wiley, New York.

Coste, F., Bounenni, A., Chanchole, S., Su, K., 2001. A method for measuring hydraulic and hydromechanical properties during damage in materials with low permeability. Thermohydromechanical Behaviour of Deep Argillaceous Rock, in: Hoteit, N., Su, K., Tijani, M., Shao, J.-F. (Ed.), Swets & Zeitlinger Publisher, The Netherlands, pp. 109–116.

Coulomb, C.A., 1773. Application of the rules of maxima and minima to some problems of statics related to architecture. Aca. Roy. Sci. Mem. Math. Phys. 7, 343–382.

Cryer, C.W., 1963. A comparison of the three-dimensional compaction theories of Biot and Terzaghi. Q. J. Mech. Appl. Math. 16, 401–412.

Detournay, E., Cheng, A.H.D., 1988. Poroelastic response of a borehole in a non-hydrostatic stress field. Int. J. Rock Mech. Min. Sci. Geomech. Abstr. 25, 171–182.

Detournay, E., Cheng, A.H.D., 1993. Fundamentals of poroelasticity, Comprehensive Rock Engineering, in: Hudson, J. (Ed.), Pergamon Press, Oxford, UK, pp. 113–171.

De Paola, N., Faulkner, D. R., Collettini C., 2009. Brittle versus ductile deformation as the main control on the transport properties of low-porosity anhydrite rocks, J. Geophys. Res. 114 (B6), B06211.

Economides, M.J., Hill A.D., Ehlig-Economides, C., 1993. Petroleum production systems, Prentice Hall, Inc., Upper Saddle River, NJ, USA.

Elsworth, D., 1989. Thermal permeability enhancement of blocky rocks: one dimensional flows. Int. J. Rock Mech. Min. Sci. Geomech. Abst. 26, 329–339.

Ezzedine S.M., 2010. Impact of geological characterization uncertainties on subsurface flow using stochastic discrete fracture network models. In: Proceedings of the Thirty-fifth Workshop on Geothermal Reservoir Engineering. Stanford University, Stanford, CA, USA. pp. 1–7.

Fang Z., Harrison, J.P., 2002. Development of a local degradation approach to the modelling of brittle fracture in heterogeneous rocks. Int. J. Rock Mech. Min. Sci. 39, 443–457.

Fehler, M., Jupe, A., Asanuma, H., 2001. More than cloud: new techniques for characterizing reservoir structuring using induced seismicity. The Leading Edge 20(3), 324–328.

Finlayson, B.A., 1972. The method of weighted residuals and variational principles. Academic Press, New York, USA.

Gharahbagh, A.E., Fakhimi, A., 2010. Pore distribution and statistical size effect: a discrete element analysis. 44th US Rock Mechanics Symposium, Salt Lake City, Utah. 10–322.

Ghassemi, A., Diek, A., 2003. Linear chemo-poroelasticity for swelling shales: theory and application. J. Pet. Sci. Eng. 38, 199–212.

Ghassemi, A., Tao, Q., Diek, A., 2009. Influence of coupled chemo-poro-thermoelastic processes on pore pressure and stress distributions around a wellbore in swelling shale. J. Pet. Sci. Eng. 67, 57–64.

Grimvall, G., 1986. Thermophysical properties of Materials, North-Holland, Amsterdam, The Netherlands.

Gurson, A.L., 1977. Continuum theory of ductile rupture by void nucleation and growth. Part I: yield criteria and flow rules for porous ductile media. J. Eng. Mater. Tech. 99, 2–15.

Hale, A.H., Mody, F.K., Salisbury, D.P., 1992. Experimental investigation of the influence of chemical potential on wellbore stability. IADC/SPE–23885, pp. 18–21.

Hamiel, Y., Lyakhovshy, V., Agnon, A., 2005. Poroelastic damage rheology: dilation, compaction, and failure of rocks. Geochem. Geophy. Geosys. 6, 1–9.

Heidug, W.K., Wong S.W., 1996. Hydration swelling of water-absorbing rocks: a constitutive model. Int. J. Num. Anal. Methods in Geomech. 20, 403–430.

Hewett, T.A., 1986. Fractal distributions of reservoir heterogeneity and their influence on fluid transport. Paper presented at the SPE Annual Technical Conference and Exhibition, New Orleans, Louisiana. SPE–15386.

Ingebritsen, S.E., Manning, C.E., 2010. Permeability of the continental crust: dyanamic variations inferred from seismicity and metamorphism. Geofluids 10, 193–205.

Jaeger, J.C., Cook, N.G.W., Zimmerman, R.W., 2007. Fundamentals of rock mechanics, fourth ed. Blackwell Publishing, Malden, Massachusetts, USA.

Kachanov, L.M., 1958. On the creep fracture time, Izv Akad, Nauk USSR Otd. Tech. 8, 26–31.

Kachanov, L.M., 1986. Introduction to continuum damage mechanics. Martinus Nijhoff Publishers, The Netherlands.

Khan, M., Teufel, L.W., 2000. The effect of geological and geomechanical parameters on reservoir stress path and its importance in studying permeability anisotropy. SPE Reservoir Evaluation & Engineering (10), 66184

Krajcinovic, D.,1983. Constitutive equations for damage materials, J. App. Mech. 50, 355–360.

Krajcinovic, D., 1996. Damage mechanics, Elsevier, Amsterdam.

Krajcinovic, D., Foneska, G.U., 1981. The continuum damage theory of brittle materials. J. App. Mech. 48, 809–824.

Kurashige, M., 1989. A thermoelastic theory of fluid-filled porou materials. Int. J. Solids Struct. 25(9), 1039–1052.

Kiyama, T., Kita, H., Ishijima, Y., Yanagidani, T., Akoi, K., Sato, T., 1996. Permeability in anisotropic granite under hydrostatic compression and tri-axial compression including post-failure region. In: Proceedings of the second North American Rock Mechanics Symposium. Montreal, Quebec, Canada, pp. 383–391.

Knutson, C.F., 1976. Modeling of noncontinuous fort union and mesaverde sandstone reservoirs, Piceance Basin, Northwestern Colorado. SPE Journal, 16(4), 5024.

Labrid, J.C., 1975. Thermodynamic and kinetic aspects of argillaceous sandstone acidizing. Soc. Petrol. Eng. J. 117–128.

Lambert, M.E., 1981. A statistical study of reservoir heterogeneity. M.S. Thesis. The University of Texas, Austin, USA.

Lemaitre, J., 1984. How to use damage mechanics. Nuclear engineering and Design. 80, 233–245.

Lemaitre, J., 1985. A continuous damage mechanics model for ductile fracture. J. Eng. Mater. And Tech. 107, 83–89.

Lemaitre, J., Chaboche, J.L., 1990. Mechanics of solid materials, Cambridge University Press, London.

Lewis R.W., Schrefler, B.A., 1988. The finite element method in the static and dynamic deformation and consolidation of porous media, second ed. John Wiley, New York.

Li, X., Cui, L., and Roegiers, J.C., 1998. Thermoporoelastic modeling of wellbore stability in non-hydrostatic stress field. Int. J. Rock Mech. Min. Sci. 35, 4–5.

Liang Z.Z., 2005. Three-dimensional numerical modelling of rock failure process. PhD Thesis. Center for Rock Instability & Seismicity Research, Dallian University of Technology, Dallian, China.

Liu Y., 2006. Using the snesim program for multiple-point statistical simulation. Computers Geosiences. 32, 1544–1563.

Lund, K., Fogler, H.S., 1976. Acidization V. the prediction of the movement of acid and permeability fronts in sandstone. Chem. Eng. Sci. 31(5), 381–392.

Mahnken, R., 2002. Theoretical, numerical and identification aspect of a new model class for ductile damage. Int. J. Plasticity 18, 801–831.

Mazars, J., 1986. A description of micro- and macroscale damage of concrete structures. Eng. Fracture. Mech. 25, 729–737.

Mazars J., Pijaudier-Cabot, G., 1996, From damage to fracture mechanics and conversely: a combined approach. Int. J. Solids and Struct. 33, 3327–3342.

Min, K.S., Ghassemi, A., 2011. A study of numerical simulations of mixed-mode fracture propagation in rock. In: Proceedings, 36th Workshop on Geothermal Reservoir Engineering. Stanford University, Stanford, CA, USA SGP-TR-191.

McTigue, D.F., 1986. Thermoelastic response of fluid-saturated porous rock. J. Geophys. Res. 91(B9), 9533–9542.

Mody, F.K., Hale, A.H., 1993. Borehole-Stability model to couple the mechanics and chemistry of drilling-fluid/shale interactions. J. Petr. Tech. 45, 1093–1101.

Muller A.L., Vargas Jr, E.D.A., Vaz, L.E., Goncalves, C.J., 2008. Borehole stability analysis considering spatial variability and poroelastoplasticity. Int. J. Rock Mech. Min. 46, 90–96.

Murakami, 1988. Mechanical modeling of material damage. J. App. Mech. 55, 280–286.

Pine, R.J., Batchelor A.S., 1984. Downward migration of shearing in jointed rock during hydraulic injections. Int. J. Rock Mech. Min. Sci. 21(5), 249–263.

Palciauskas, W., Domenico, PA., 1982. Characterization of drained and undrained response of thermally loaded repository rocks. Water Res. Res. 18, 281–290.

Rhett, D.W., Teufel, L.W., 1992. Stress dependence of matrix permeability of North Sea sandstone reservoir rock. In: Proceedings, 33rd U.S. Symposium on Rock Mechanics. Santa Fe, New Mexico, 345–355.

Rice, J.R., Cleary, M.P., 1976. Some basic stress-diffusion solutions for fluid-saturated elastic porous media with compressible constituents. Rev. Geophys. Space Phys. 14, 227–241.

Rothert, E., Shapiro, S.A., 2003. Microseismic monitoring of borehole fluid injection: data modeling and inversion for hydraulic properties of rocks. Geophysics 68(2), 685–689.

Ruistuen, H., Teufel, L.W., Rhett, D.W., 1996. Influence of reservoir stress path on deformation and permeability of weakly cemented sandstone reservoirs. SPE–36535.

Safari, M.R., Ghassemi, A., 2011. A 3D analysis of enhanced geothermal reservoir: shear slip and micro-seismicity. 45th US Rock Mehcanics/Geomechanics Symposium. 11–480.

Selvadurai, A.P.S., 2004. Stationary damage modeling of poroelastic contact. Int. J. Solids Struct. 41, 2043–2064.

Shao, J.F. and Marchina, P., 2002. A damage mechanics approach for the modelling of sand production in heavy oil reservoirs. Paper presented at the SPE/ISRM Rock Mechanics Conference. SPE–78167.

Shapiro, S., Huenges, E., Borm, G., 1997. Estimating the crust permeability from fluid-injection-induced seismic emission at the KTB site. Geophys. J. Int. 131, F15–F18.

Shapiro, S., Audigane, P., Royer, J., 1999. Large-scale in situ permeability tensor of rocks from induced microseismicity. Geophys. J. Int. 137, 207–213.

Shapiro, S. A., Rothert, E., Rath, V., Rindschwentner, J., 2002. Characterization of fluid transport properties of reservoirs using induced microseismicity. Geophysics. 67, 212–220.

Sherwood, J.D., Bailey, L., 1994. Swelling of shale around a cylindrical well-bore. Proc. R. Soc. A 444, 161–184.

Shipping, L., Yushou, L., Yi, L., Zhenye, W., Gang, Z., 1994. Permeability-strain equations corresponding to the complete stress-strain path of Yinzhuang Sandstone. Int. J. Rock Mech. Min. Sci. Geomech. Abstr. 41, 2043–2064.

Sidoroff, F., 1981. Description of anisotropic damage application to elasticity. IUTAM Coloqium on Physical Nonlineariteis in Structural Analysis. Springer-Verlag, Berlin.

Simakin, A., Ghassemi, A., 2005. Modelling deformation of partially melted rock using a poroviscoelastic rheology with dynamic power law viscosity. Tectonophysics 397, 195–209.

Smith I. M., Griffiths D. V., 2004. Programming the finite element method, fourth ed. John Wiley, New York.

Smith, P.J. and Morgan, D.T.K., 1986. Modelling faulted and fluvial reservoirs. Paper presented at the European Petroleum Conference, London, UK. SPE–15853-MS.

Strang G., Fix, G.J., 1973. An analysis of the finite element method. Wellesley Cambridge Press, Massachusetts.

Talwani, P., Acree, S., 1985. Pore pressure diffusion and the mechanism of reservoir-induced seismicity. Pure Appl. Geophys. 122, 947–965.

Tang, C.A., Tham, L.G., Lee, P.K.K., Yang, T.H., Li, L.C., 2002. Coupled analysis of flow, stress and damage (FSD) in rock failure. Int. J. Rock Mech. Min. 39, 477–489.

Tao, Q., 2000. Wellbore stability in water-sensitive shales. M.S. Thesis. University of North Dakota. Grand Forks, ND, USA.

Terzaghi, K., 1923. Die Berechnung des durchlassigkeitsziffer des tones aus dem verlauf der hydrodynamischen spannungserscheinungen, Sitz. Akad. Wiss. Wien, Abt. IIa. 132, 125– 38.

Terzaghi, K., 1936. The shearing resistance of saturated soils and the angle between planes of shear. Proc. Int. Conf. Soil Mech. Found. Eng. Vol. 1, Harvard University Press. Cambridge, MA, USA.

Thomas, L.K., Chin, L.Y., Pierson, R.G., Sylte, J.E., 2003. Coupled geomechanics and reservoir simulation. SPE–87339-PA.

Timoshenko, S.P., Goodier J.N., 1982. Theory of elasticity, international ed. McGraw-Hill, Singapore.

Tvergaard, V., 1982. Material failure by void coalescence in localized shear bands. Int. J. Solids Struct. 18, 659–672.

Voyiadjis, G.Z., Kattan, P.I., 1999. Advances in damage mechanics: metals and metals matrix composites. Elsevier Science, Oxford, UK.

Wang Y., Papamichos E., 1994. Conductive heat flow and thermally induced fluid flow around a wellbore in a poroelastic medium. Water Resour. Res. 30(12), 3375-3384.

Wang, J.A., Park H.D., 2002. Fluid permeability of sedimentary rock in a complete stress-strain process. Eng. Geol. 63, 291–300.

Weibull W., 1951. A statistical distribution function of wide applicability. J. Appl. Mech. 18, 293–297.

Yang, T.H., Tham, L.G., Tang, C.A., Liang, Z.Z., Tsui, Y., 2004. Influence of heterogeneity of mechanical properties on hydraulic fracturing in permeable rocks. Rock Mech. Rock Eng. 37, 251–275.

Yu, M., Chen, G., Chenevert, M.E., Sharma M.M., 2001. Chemical and thermal effects on wellbore stability of shale formations, Paper presented at the SPE Annual Technical Conference and Exhibition, New Orleans, Louisiana. SPE–71366.

Yuan, S.C., Harrison, J.P., 2006. A review of the state of the art in modeling progressive mechanical breakdown and associated fluid flow in intact heterogeneous rock, Int. J. Rock Mech. Min. 43, 1001–1022.

Voss, R.F., 1985. Random fractals: characterization and measurement, Plenum Press, New York.

Voyiadjis, G.Z., Kattan, P.I., 1999. Advances in damage mechanics: metals and metals matrix composites, Elsvier Science, Oxford.

Zhao, X.L., Ma, Q., Roegiers J.C., 1993. The measurement of compressibility of fractured rock. SCA–9318.

Zhou, X., Ghassemi, A., 2009. Finite element analysis of coupled chemo-poro-themo-mechanical effects around a wellbore in swelling shale. Int. J. Rock Mech. Min. 46, 769–778.

Zienkiewicz, O.C., Taylor, R., 1991. The finite element method. Mcgraw-Hill, New York.

Zoback, M.D., Byerlee, J.D. 1975. The effect of micro-crack dilatancy on the permeability of westerly granite. J. Geophys. Res. 80, 752–755.

APPENDIX A

DERIVATION OF FINITE ELEMENT DISCRETIZATION FOR FULLY COUPLED CHEMO-THER-POROELASTICITY

1. Field equations for displacement, pore pressure, solute mass concentration, and temperature

$$\left(K+\frac{G}{3}\right)\nabla(\nabla\cdot\mathbf{u})+G\nabla^2\mathbf{u}+m\left(\alpha'\nabla p-\chi\nabla C^S+\gamma_1\nabla T\right)=0 \quad \text{..... (A.1)}$$

$$\alpha(\nabla\cdot\dot{\mathbf{u}})+\beta'\dot{p}+\chi'\dot{C}^S+\gamma_2\dot{T}-\frac{k}{\mu}\nabla^2 p+\frac{k}{\mu}L_D\nabla^2 C^2=0 \quad \text{..... (A.2)}$$

$$\phi\dot{C}^S-D^S\nabla^2 C^S-C^S D^T\nabla^2 T=0 \quad \text{..... (A.3)}$$

$$\dot{T}-c^T\nabla^2 T=0 \quad \text{..... (A.4)}$$

2. Weight residual method

The governing equation can be discretized from the following examples. A typical example for solving the differential equation is

$$L(u)=f \quad \text{..... (A.5)}$$

where L is the differential equation as a function of u, and f is the known function of the independent variables.

The solution of u has weak formulations:

$$u(x)\approx U_N(x)=\sum_{j=1}^{N}c_j\phi_j(x)+\phi_0(x) \quad \text{..... (A.6)}$$

If we substitute $U_N(x)$ in the left hand side of Eq. A.5, the residuals can be obtained by $L(U_N) - f$, which is called the residual of the approximation.

$$R \equiv U_N(x) - f = L\left(\sum_{j=1}^{N} c_j \phi_j(x) + \phi_0(x) \right) - f \neq 0 \quad \text{..... (A.7)}$$

The parameter c_j is solved by setting residual *R* to vanish by integration in the weighted-residual method:

$$\int_{\Omega} \psi_i(x) R(x, C_j)\, d\Omega \qquad (i = 1,2,3,...N) \quad \text{..... (A.8)}$$

where $\psi_i(x)$ are the weight functions and the most widely used weighted-residual method can be summarized as

Galerkin's method: $\psi_i = \phi_i$

Petrov-Galerkin method: $\psi_i \neq \phi_i$

Least squares method: $\psi_i = \frac{\partial R}{\partial c_i}$

3. Application of Galerkin's method for the variables

The continuous variables u, p, C^S, and T are approximated by the nodal values through the shape functions as

$$\tilde{u} = \sum_{i=1}^{q} N_i u_i \qquad \tilde{p} = \sum_{i=1}^{q} N_i p_i \qquad \tilde{T} = \sum_{i=1}^{q} N_i T_i \qquad \tilde{C}^S = \sum_{i=1}^{q} N_i C_i^S$$

We can substitute the nodal variables to the field equations by applying Galerkin's residual method.

For solids,

$$\left(K + \frac{G}{3}\right) \int_\Omega [N_u]^T \frac{\partial^2}{\partial x^2}[N_u]\{\mathbf{u}\}\, d\Omega + G \int_\Omega [N_u]^T \frac{\partial^2}{\partial x^2}[N_u]\{\mathbf{u}\}\, d\Omega +$$
$$\left(K + \frac{G}{3}\right) \int_\Omega [N_u]^T \frac{\partial^2}{\partial x \partial y}[N_u]\{\mathbf{u}\}\, d\Omega + \alpha' \int_\Omega [N_p]^T \frac{\partial}{\partial x}[N_p]\{\mathbf{p}\}\, d\Omega -$$
$$\chi \int_\Omega [N_{C^S}]^T \frac{\partial}{\partial x}[N_{C^S}]\{\mathbf{C^S}\}\, d\Omega + \gamma_1 \int_\Omega [N_T]^T \frac{\partial}{\partial x}[N_T]\{\mathbf{T}\}\, d\Omega = 0$$

For fluids,

$$\alpha \int_\Omega [N_u]^T \frac{\partial}{\partial x}[N_u]\{\dot{\mathbf{u}}\}\, d\Omega + \beta' \int_\Omega [N_p]^T [N_p]\{\dot{\mathbf{p}}\}\, d\Omega +$$
$$\chi' \int_\Omega [N_{C^S}]^T [N_{C^S}]\{\dot{\mathbf{C}}^{\mathbf{S}}\}\, d\Omega + \gamma_2 \int_\Omega [N_T]^T [N_T]\{\dot{\mathbf{T}}\} -$$
$$\frac{k}{\mu} \int_\Omega [N_p]^T \frac{\partial^2}{\partial x^2}[N_p]\{\mathbf{p}\}\, d\Omega + \frac{k}{\mu} L_D \int_\Omega [N_{C^S}]^T \frac{\partial^2}{\partial x^2}[N_{C^S}]\{\mathbf{p}\}\, d\Omega = 0$$

For solute mass concentrations,

$$\phi \int_{\Omega} \left[N_{C^S}\right]^T \left[N_{C^S}\right] \left\{\dot{\mathbf{C}}^{\mathbf{S}}\right\} d\Omega - D^S \int_{\Omega} \left[N_{C^S}\right]^T \frac{\partial^2}{\partial x^2} \left[N_{C^S}\right] \left\{\mathbf{C}^{\mathbf{S}}\right\} d\Omega$$
$$- \int_{\Omega} \left[N_T\right]^T \left\{\mathbf{C}^{\mathbf{S}}\right\} \frac{\partial^2}{\partial x^2} \left[N_T\right] \{\mathbf{T}\}\, d\Omega = 0$$

For temperature,

$$\int_{\Omega} \left[N_T\right]^T \left[N_T\right] \{\dot{\mathbf{T}}\}\, d\Omega - c^T \int_{\Omega} \left[N_T\right]^T \frac{\partial^2}{\partial x^2} \left[N_T\right] \{\mathbf{T}\}\, d\Omega = 0$$

Integration by parts for the above three equations leads to

$$\mathbf{K_m}\, \tilde{\mathbf{u}} + \mathbf{A}\, \tilde{\mathbf{p}} - \mathbf{W} \tilde{\mathbf{C}} + \mathbf{V}\, \tilde{\mathbf{T}} = \mathbf{0}$$

$$\mathbf{A^T}\, \dot{\tilde{\mathbf{u}}} + \mathbf{S}\, \dot{\tilde{\mathbf{p}}} + \hat{\mathbf{M}} \dot{\tilde{\mathbf{C}}} + \mathbf{N}\, \dot{\tilde{\mathbf{T}}} + \mathbf{H_H} \tilde{\mathbf{p}} + \mathbf{D_H} \tilde{\mathbf{C}}^{\mathbf{S}} = \mathbf{0}$$

$$\mathbf{M} \dot{\tilde{\mathbf{C}}}^{\mathbf{S}} + \mathbf{D_D} \tilde{\mathbf{C}}^{\mathbf{S}} + \mathbf{Q_D}\, \tilde{\mathbf{T}} = \mathbf{f^u}$$

$$\mathbf{R} \dot{\tilde{\mathbf{T}}} + \mathbf{U}\, \tilde{\mathbf{T}} = 0$$

where :

$$\mathbf{K_m} = \int_{\Omega} \mathbf{B^T D_u B}\, d\Omega$$

$$\mathbf{A} = \int_{\Omega} \mathbf{B^T \alpha\, m\, N_p}\, d\Omega$$

$$\mathbf{W} = \int_{\Omega} \mathbf{B^T}\, \chi\, \mathbf{m\, N_{C^S}}\, d\Omega$$

$$\mathbf{V} = \int_{\Omega} \mathbf{B}^{\mathbf{T}} \, \gamma_1 \, \mathbf{m} \, \mathbf{N}_{\mathbf{T}} \, d\Omega$$

$$\mathbf{S} = \int_{\Omega} \mathbf{N}_{\mathbf{p}}^{\mathbf{T}} \beta' \mathbf{N}_{\mathbf{p}} \, d\Omega$$

$$\hat{\mathbf{M}} = \int_{\Omega} \mathbf{N}_{\mathbf{p}}^{\mathbf{T}} \chi' \mathbf{N}_{\mathbf{C}^{\mathrm{s}}} \, d\Omega$$

$$\mathbf{N} = \int_{\Omega} \mathbf{N}_{\mathbf{T}}^{\mathbf{T}} \gamma_2 \, \mathbf{N}_{\mathbf{T}} \, d\Omega$$

$$\mathbf{M} = \int_{\Omega} \mathbf{N}_{\mathbf{C}^{\mathrm{s}}}^{\mathbf{T}} \phi \mathbf{N}_{\mathbf{C}^{\mathrm{s}}} \, d\Omega$$

$$\mathbf{R} = \int_{\Omega} \mathbf{N}_{\mathbf{T}}^{\mathbf{T}} \mathbf{N}_{\mathbf{T}} \, d\Omega$$

$$\mathbf{U} = \int_{\Omega} \left\{ (\nabla \mathbf{N}_{\mathbf{T}})^T \left(c^T \right) (\nabla \mathbf{N}_{\mathbf{T}}) + (\mathbf{N}_{\mathbf{T}})^T \mathbf{v}_{\mathbf{f}} \, (\nabla \mathbf{N}_{\mathbf{T}}) \right\} d\Omega$$

$$\mathbf{H}_{\mathbf{H}} = \int_{\Omega} \left(\nabla \mathbf{N}_{\mathbf{p}} \right)^T (\mathbf{k} / \eta) \left(\nabla \mathbf{N}_{\mathbf{p}} \right) d\Omega$$

$$\mathbf{D}_{\mathbf{H}} = \int_{\Omega} \left(\nabla \mathbf{N}_{\mathbf{p}} \right)^T L_D \left(\nabla \mathbf{N}_{\mathbf{p}} \right) d\Omega$$

$$\mathbf{D}_{\mathbf{D}} = \int_{\Omega} \left(\nabla \mathbf{N}_{\mathbf{C}^{\mathrm{s}}} \right)^T D^S \left(\nabla \mathbf{N}_{\mathbf{C}^{\mathrm{s}}} \right) d\Omega$$

$$\mathbf{Q}_{\mathbf{D}} = \int_{\Omega} (\nabla \mathbf{N}_{\mathbf{T}})^T C^S D^S \, (\nabla \mathbf{N}_{\mathbf{T}}) \, d\Omega$$

VITA

Name: Sang Hoon Lee

Address: Harold Vance Department of Petroleum Engineering, 3116 TAMU, College Station, TX 77843-3116

Email Address: sanghoon.lee75@gmail.com

Education:

University of Seoul
Seoul, Republic of Korea
B.S., Chemical Engineering
February 2002

Seoul National University
Seoul, Republic of Korea
M.S., Chemical Engineering
February 2004

Texas A&M University
College Station, Texas
Ph.D., Petroleum Engineering
December 2011

Affiliations: American Rock Mechanics Association
Society of Petroleum Engineers